Dissecting the mechanisms of translational regulation by neuronal ribosomes

Albert Tensing Blandy

200937143

Submitted in accordance with the requirements for the degree of

Masters by research

The University of Leeds

School of Molecular and Cellular Biology

July 2022

Supervisors: Dr Julie Aspden, Dr Juan Fontana and Dr Amanda Bretman

The candidate confirms that the work submitted is their own and that appropriate credit has been given where reference has been made to the work of others.

Abstract

Regulation of translation is vital in all living systems, underpinning the coordination of organismal development, cellular processes, and responses to external stimuli and stresses. Multiple studies have identified that ribosomes exist in heterogenous populations arising from differences in rRNA and ribosomal protein (RP) composition. In some instances, this heterogeneity enables translational regulation of specific groups of mRNAs.

Recent quantitative tandem mass tag mass spectrometry (TMT-MS) of ribosomes from *D. melanogaster* tissues revealed that RpS11 was found to be significantly enriched in head 80S monosomes and polysomes, in comparison to other tissue ribosomes. Therefore, I sought to investigate this ribosomal heterogeneity and its impact on translation. Selective knockdown of RpS11 was performed in fly neurons, to determine the importance of RpS11 in neuronal translation. Preliminary analysis suggests that RpS11 is required for global translation in the brain, but further analysis is required to confirm this. To dissect the structural implications of RpS11 enrichment in *D. melanogaster* head 80S monosomes, single particle cryo-EM of purified head 80S monosomes was carried out. However, no additional RpS11 densities could be identified to explain higher levels of RpS11 compared to other 80S ribosomes and no structural consequences of the reported RpS11 enrichment were identified.

Interestingly, whilst analysing the cryo-EM structure of head 80S ribosomes, I discovered that ~98% of these monosomes contain tRNAs, indicating that they are engaged in active translation. This is surprising because 80S monosomes are thought to be largely inactive. Further analysis of 80S structures from other tissues indicated that the levels of monosomes actively translating varies tremendously. 91% of embryo monosomes were also found to be engaged in active translation, in contrast to the testis and ovary where no monosomes were found to be actively translating. This implies that monosomal translation is potentially induced in the head (and therefore the brain) and embryo, suggesting a vital role in the translation of specific mRNAs in these tissues. Further analysis of the tRNA densities enabled the identification of 5 stages of translation elongation. Together this work indicates that monosomal translation is favoured in certain tissues and developmental stages to regulate the translation of specific mRNAs.

Acknowledgements

I am incredibly grateful to my supervisors Dr. Julie Aspden, Dr. Juan Fontana and Dr. Amanda Bretman, for their ceaseless encouragement, kindness and patience. I am very lucky to have had them as my supervisors and none of this work would have been possible without their support, feedback or technical expertise. I also owe a great deal of gratitude to the amazing Aspden and Fontana lab groups, in particular, Dr. Karl Norris and Tayah Hopes for their help with performing and understanding many of the experiments and analyses in this report.

A very big thanks to Michaela Agapiou, Tayah Hopes, and Julie Aspden for generating the *D. melanogaster* testis and ovary tissue ribosome datasets, which were image processed by Juan Fontana. Thanks also to Amy Turner for generating the *D. melanogaster* embryo and head tissue ribosome datasets and image processing the embryo datasets.

Finally, I want to thank the Astbury Biostructure Laboratory EM support staff for aiding and facilitating all the cryo-EM analysis performed and analysed in this report.

Table of Contents

List of tables

List of figures

List of Supplemental Figures

List of abbreviations

Abbreviation	Description
3'-UTR	3'- Untranslated Region
43S PIC	43S Preinitiation Complex
5'-UTR	5'-Untranslated Region
A/A	Aminoacyl (tRNA site)
A/P	Aminoacyl/Peptidyl (hybrid tRNA site)
aa-tRNA	Aminoacylated tRNA
ABCE1	ATP Binding Cassette Subfamily E Member 1
ALS	Amyotrophic Lateral Sclerosis
ATP	Adenosine Triphosphate
CaMV	Cauliflower Mosaic Virus
CHX	Cycloheximide
Cryo-EM	Cryogenic Electron Microscopy
CTF	Contrast Transfer Function
CyO	Curly O
DTT	Dithiothreitol
E/E	Exit (tRNA site)
eEF	Eukaryotic Elongation Factor
eIF	Eukaryotic Initiation Factor
elav	Embryonic Lethal Abnormal Vision
eRF	Eukaryotic Release Factor
FMRP	Fragile X Mental Retardation Protein
FSC	Fourier Shell Correlation
GDP	Guanosine Diphosphate
GraFix	Gradient Fixation
GTP	Guanosine Triphosphate
Hox	Homeobox
IFRD	Interferon Related Developmental Regulator
IRES	Internal Ribosome Entry Site
KSHV	Kaposi's Sarcoma-associated Herpesvirus
LC-MS-MS	Liquid Chromatography Tandem Mass Spectrometry
LN_2	Liquid Nitrogen

LoG	Laplacian of Gaussian
LSD	d-Lysergic acid diethylamide bitartrate
m^7G cap	7-Methylguanosine Cap
mESC	Mouse Embryonic Stem Cell
Met-tRNAi	Methionine Initiator tRNA
mORF	Main Open Reading Frame
mRNA	Messenger RNA
MS	Mass Spectrometry
MWCO	Molecular Weight Cut-Off
NMD	Nonsense Mediated Decay
ORF	Open Reading Frame
P/E	Peptidyl/Exit (tRNA site)
P/P	Peptidyl (tRNA site)
PABP	Poly(A) Binding Protein
PBS	Phosphate Buffer Solution
qPCR	Quantitative Polymerase Chain Reaction
RAN	Repeat Associated Non-AUG
RNA	Ribonucleic Acid
RNAi	RNA Interference
RP	Ribosomal Protein
rRNA	Ribosomal RNA
S2	Schneider 2
smFRET	Single Molecule Fluorescence Resonance Energy Transfer
TAV	Transactivator
TMT-MS	Tandem Mass Tag Mass Spectrometry
tRNA	Transfer RNA
UAS	Upstream Activator Sequence
UCSF	University of California San Francisco
UFM	Ubiquitin Fold Modifier
uORF	Upstream Open Reading Frame
VDRC	Vienna Drosophila Resource Centre
XL-MS	Cross Linking Mass Spectrometry

1 Introduction

1.1 The eukaryotic ribosome

The ribosome is a ribonucleoprotein particle that performs the process of translation. These macromolecular machines translate the genetic information encoded by mRNAs to create the proteome of all cells (Woolford and Baserga, 2013). Generally, eukaryotic ribosome consists of the 60S subunit containing the 28S, 5.8S and 5S rRNAs and 46 ribosomal proteins (RPs), and the 40S subunit consists of the 18S rRNA and 33 RPs (Thomson et al., 2013).

The function of the 60S subunit is to catalyse peptide bond formation, facilitated by the 28S rRNA which forms the peptidyl transferase centre (Baxter-Roshek et al., 2007). Whereas the 40S subunit binds mRNA and is responsible for translation fidelity, ensuring correct base pairing between mRNA codons and anticodons of the aminoacylated tRNAs (aa-tRNAs) (Doudna and Rath, 2002). Association of the 60S and 40S subunits forms the 80S ribosome, forming the mRNA channel and the 3 classical sites of tRNA binding: A/A (aminoacyl), P/P (peptidyl) and E/E (exit) (Figure 1) (Schuller and Green, 2018).

1.2 tRNA positioning and conformations during eukaryotic translation

tRNAs act as substrates of protein synthesis that when charged with amino acids (aa-tRNAs) links the mRNA codon and amino acids, by binding to the mRNA codon in the tRNA sites of the ribosome via its anti-codon loop by base pairing interactions (Raina and Ibba, 2014). Therefore, tRNAs decode the mRNA sequence into protein by delivering amino acids, as specified by the mRNA codons of the open reading frame (ORF), that bind to the growing nascent peptide chain by peptide bond formation (Berg and Brandl, 2021). To achieve this the tRNAs must progress through the tRNA binding sites in the mRNA channel of the ribosome facilitated by movement of the small and large subunits during translation as well as the action of translation factors (Berg and Brandl, 2021). The tRNA sites and conformations that tRNAs occupy in the ribosome is dependent on the phase of eukaryotic translation. In addition to the classical tRNA positions (A/A, P/P and E/E), the intermediate A/P and E/P tRNA positions are formed in the process of translation as the tRNAs move through the tRNA sites from the A/A to the E/E site (Figure 2) (Zhou et al., 2014). These hybrid tRNA positions were discovered by chemical modification of tRNAs, which revealed that after peptide bond formation the acceptor ends of the A/A and P/P tRNAs move into the P/P and E/E sites, due to the spontaneous rotation of the 60S subunit (Moazed and Noller, 1989).

The complex process of mRNA translation is highly regulated and occurs in 3 distinct stages: initiation, elongation and termination, followed by recycling of the 40S and 60S subunits (Figure 3). Each stage is facilitated by dedicated translational factors that recruit the 80S to the start codon (i.e. eukaryotic initiation factors, eIFs), promote peptide synthesis (i.e. eukaryotic elongation factors, eEFs) and recycling or reinitiating ribosomes once a stop codon has been reached (i.e. eukaryotic release factors, eRFs) (Figure 3) (Aitken and Lorsch, 2012; Dever et al., 2018; Frolova et al., 1996).

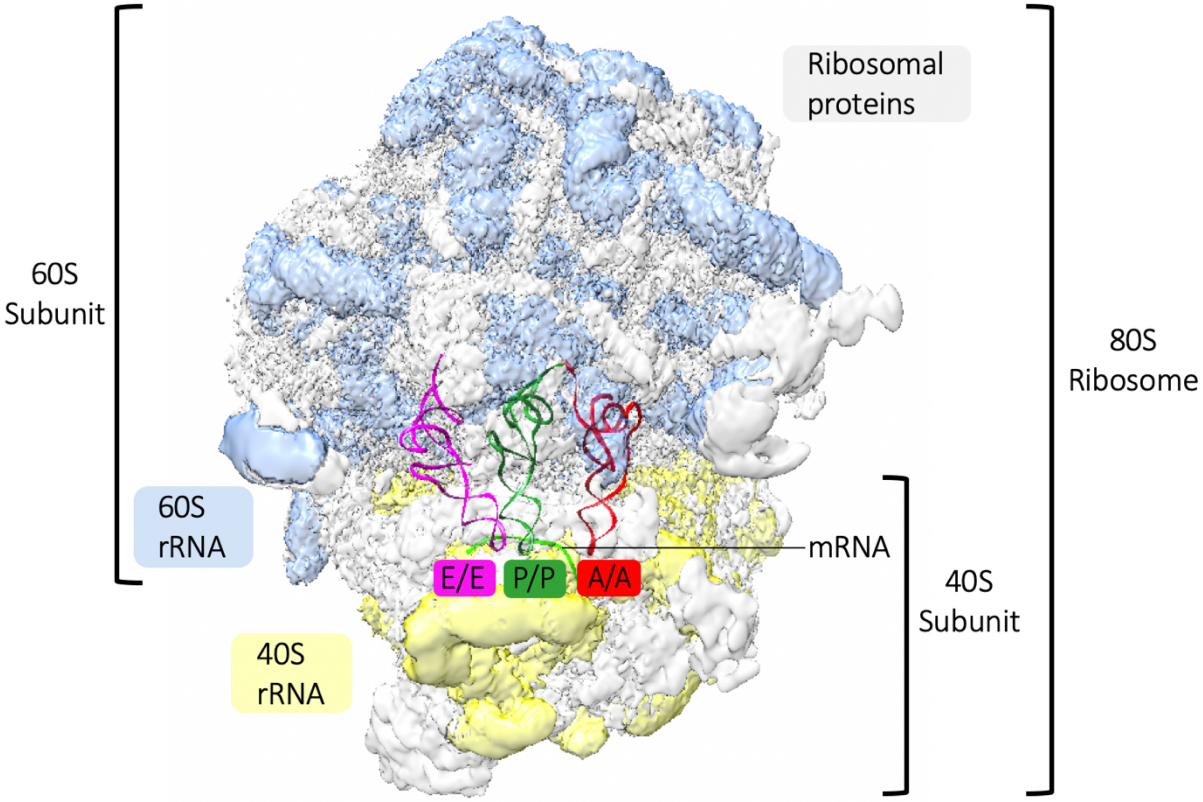

Figure 1. Structure of the 80S eukaryotic ribosome, formed by the association of 60S and 40S subunits. Each subunit consists of multiple and subunit-specific RPs (light grey) and, 60S (light blue) rRNAs and the 40S rRNA (yellow). Association of the 2 subunits forms the A/A (red), P/P (green) and E/E (pink) classical tRNA binding sites, required for peptide chain formation.

Figure adapted from Schuller and Green, 2018.

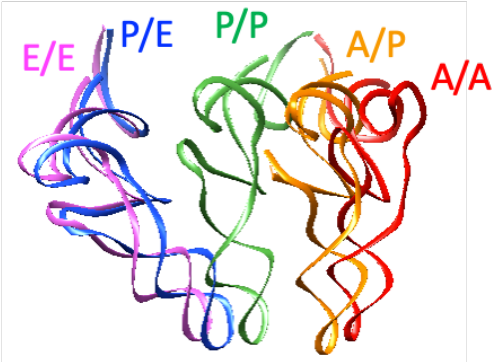

Figure 2. Comparison of the classical eukaryotic tRNA positions (A/A, P/P and E/E) with the hybrid state tRNA positions (A/P and P/E). tRNAs were selected from a range of eukaryotic atomic models, as translation is conserved across eukaryotic species (Dever et al., 2018). Classical tRNAs: A/A (red) from the *Saccharomyces cerevisiae* 60S ribosomal subunit, PDB code: 5GAK (Schmidt et al., 2015), P/P (green) from *D. melanogaster* testis 80S polysome, PDB code: 6XU7 (Hopes et al., 2021) and E/E (pink) from *D. melanogaster* embryonic extract 80S monosome, PDB code: 4V6W (Anger et al., 2013). Hybrid state tRNAs: A/P (orange) and P/E (blue) from rabbit reticulocyte lysate 80S ribosome on globin mRNA in rotated state, PDB code: 6HCJ (Juszkiewicz et al., 2018).
Figure made with UCSF Chimera.

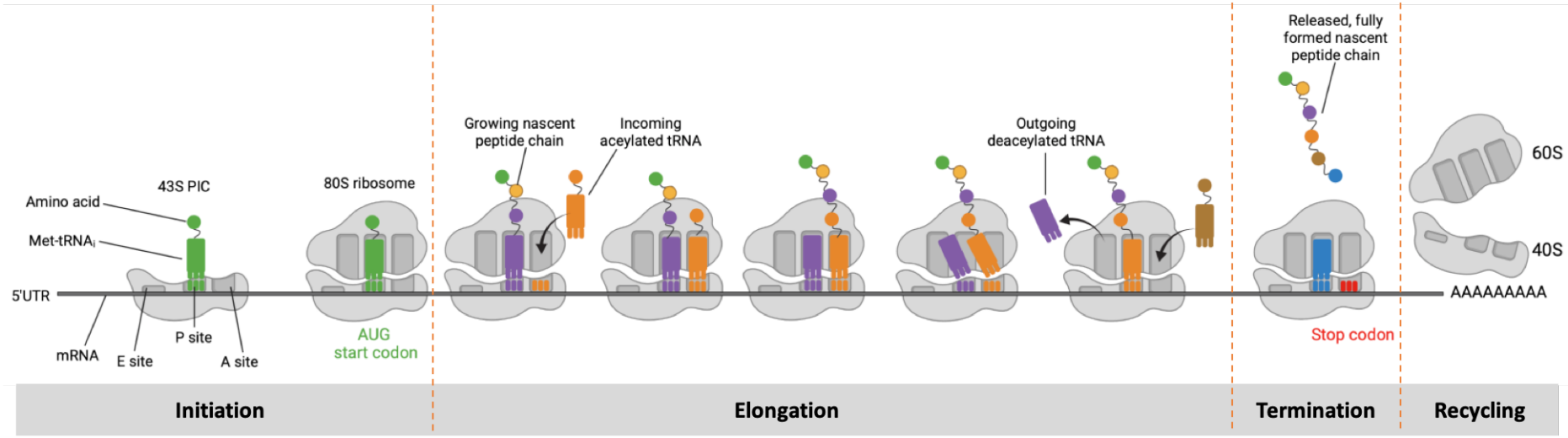

Figure 3. The stages of eukaryotic translation. Initiation is coordinated by eIFs and Met-tRNAi binding to the 40S forming the 43S preinitiation complex (43S PIC) that scans the mRNA and binds the AUG start codon. This induces the binding of the 60S subunit forming the 80S ribosome. Next, elongation allows synthesis of the peptide chain regulated by eEFs and aa-tRNAs. The elongation phase is repeated for each codon in the ORF following the AUG start codon until a stop codon is recognised. After stop codon recognition, the termination phase occurs, regulated by action of the eRFs the peptide chain is released. The 40S and 60S disengage from the mRNA and are recycled for further round of translation.

Figure made with Biorender.

1.2.1 Initiation

The first phase of translation is initiation, comprising of multiple stages before the 80S ribosome formation and Met-tRNAi base pairing to the AUG start codon.

Firstly, the 43S pre-initiation complex (43S PIC) is formed by binding of the ternary complex (eIF2-GTP bound to the methionine initiator tRNA (Met-tRNAi)) to the 40S subunit plus eIFs 1, 1A, 3 and 5 (Aitken and Lorsch, 2012). eIFs 1 and 1A bind at the A/A and P/P tRNA sites of the 40S subunit, opening a cleft between the 40S head and body, allowing for single stranded mRNA binding (Merrick and Pavitt, 2018). Concurrently, eIF4F (a complex of eIF4E, eIF4G and eIF4A) binds to the 5' 7-methylguanosine cap (m^7G cap) and poly(A) binding protein (PABP) at the 3' poly(A) tail, activating the mRNA. The RNA helicase eIF4A unwinds the mRNA secondary structure to allow for the 43S PIC to bind (Jackson et al., 2010). The 43S PIC scans the mRNA from the m^7G cap, in a 3' direction requiring ATP. When the 43S PIC reaches the AUG start codon base pairing interactions form with the Met-tRNAi anticodon. This triggers the hydrolysis of the GTP bound to eIF2 arresting scanning by closing the open scanning conformation of the 43S PIC, causing the release of eIF1 (Aitken and Lorsch, 2012). eIF2-GDP and eIF5 dissociate from the 43S PIC, allowing binding of the 60S subunit bound to eIF5B-GTP. Binding of the 60S to the 40S subunit is followed by eIF5B GTP hydrolysis, eIF5B-GDP and eIF1A dissociate, forming the 80S ribosome (Jackson et al., 2010). The precise timing of the dissociation of the remaining initiation factors (eIF4F, eIF4B and eIF3) has not yet been elucidated, however, they have been determined to be released before the ribosome progresses to the elongation stage (Merrick and Pavitt, 2018).

1.2.2 Elongation

For each subsequent mRNA codon in the ORF after the AUG start codon and preceding the stop codon, the ribosome cycles through the elongation stages (Figures 3 and 4).

A/A site tRNA selection is the first stage of elongation, commenced by the delivery of an aa-tRNA in complex with eEF1A and GTP to the A/A site. Base-pairing between the anticodon of the aa-tRNA and the codon in the A/A site hydrolyses the GTP, releasing the eEF1A-GDP complex and induces A/A site tRNA occupation (Figure 4) (Rodnina et al., 2005).

The second stage of elongation is peptide bond formation, occurring rapidly after A/A tRNA selection. Peptide bond formation is catalysed by the peptidyl transferase centre, which favourably positions the A/A and P/P site tRNAs (Jia et al., 2021). The peptide bond is formed by nucleophilic attack of the α-amino group of the A/A site tRNA on the carbonyl carbon of the P/P site tRNA (Budkevich et al.,

2011). This transfers the P/P site tRNA peptides to the A/A site amino acid, lengthening the peptide chain by 1 amino acid and deacylates the P/P site tRNA, forming the pre-translocation state (Figure 4) (Hiller et al., 2011).

The third and final stage of elongation is translocation, achieved by progressing from the pre-translocation state to the post-translocation state, via the hybrid state. Translocation transfers the A/A site tRNA with the nascent peptide chain bound and the deacylated P/P site tRNA to the P/P site and E/E site, respectively; as well as simultaneously translocating the mRNA transcript by 1 codon (Figure 4) (Frank et al., 2007). In the pre-translocation stage, the newly formed deacyl P/P site unlocks the ribosome allowing the 40S and 60S subunits to spontaneously and reversibly rotate, with respect to one another (Munro et al., 2010). The binding of eEF2-GTP locks the 80S ribosome in the hybrid state preventing reversal of the subunit rotation to the pre-translocation state (Djumagulov et al., 2021). This rotation induces the acceptor ends of the A/A and P/P tRNAs to move into the P/P and E/E sites of the 60S whilst the anticodon stem-loops remain occupied in the 40S A/A and P/P sites. This forms the hybrid state of the translocation with the intermediate state A/P and P/E tRNAs (Figure 4) (Frank et al., 2007). Notably, the translational inhibitor cycloheximide (CHX), has been shown by single-molecule FRET microscopy (smFRET) to prevent translocation by occupying the E/E site of elongating ribosomes. This halts translocation by preventing A/A and P/P site tRNAs from entering the hybrid state through inhibiting eEF2 binding (Budkevich et al., 2011). Therefore, in the presence of CHX the tRNAs cannot progress through the mRNA channel as translocation has been inhibited. The post-translocation state is formed by the hydrolysis of the GTP bound by eEF2 to GDP, which induces a conformational change in eEF2 causing the 40S head domain to rotate relative to the large subunit, severing the base paring of the tRNA and mRNA and resulting in the dissociation of eEF2-GDP. Together these actions shift the anticodon stem loops of the intermediate tRNAs, so the tRNAs now occupy E/E and P/P sites and translocate the mRNA by 1 codon so that the next codon of the ORF is now situated in the A/A site (Figure 4) (Taylor et al., 2007; Behrmann et al., 2015).

smFRET experiments have also revealed that the E/E site deacylated tRNA is ejected by allosteric interactions upon aa-tRNA A/A site binding during early stages of protein translation. However, in later cycles the E/E site tRNA spontaneously dissociated (Chen et al., 2011). Despite this finding being determined *in vitro* and in prokaryotic ribosomes, these mechanisms are likely well conserved in eukaryotes as with many of the reactions in translation as well as the peptide sequences and structures of the translation factors (Ganoza et al., 2002).

1.2.3 Termination

Recognition of the stop codon in the A/A site by eRF1 leads to the binding of the eRF1-eRF3-GTP complex. eRF3 GTP hydrolysis induces release of the nascent peptide chain from the P/P site tRNA. This results in the 80S ribosome with the deacylated tRNA in the P/P site, bound to the mRNA codon preceding the stop codon (Figure 4) (Frolova et al., 1996). Finally, ABCE1 (ATP Binding Cassette Subfamily E Member 1) induces dissociation of the post-termination 80S ribosome into the 60S, and mRNA- and deacylated P/P site tRNA-bound 40S subunits. These subunits are then recycled for subsequent rounds of translation (Pisarev et al., 2010).

1.3 Monosomal versus polysomal translation

Two populations of 80S ribosomes exist in cells: monosomes and polysomes. Polysomes are groups of 2 or more 80S ribosomes that are bound to a single mRNA transcript, whereas monosomes are lone 80S ribosomes occupying either a mRNA transcript or existing as 80S ribosomes formed in the absence of mRNA termed 'vacant couples' (Noll et al., 1973). These vacant couples are in contrast to the translating 80S ribosomes that conventionally form at the AUG start codon (Aitken and Lorsch, 2012). eEF2 has been determined to occupy vacant couples, stably binding the 80S ribosomes. In contrast, eEF2 was found to be mostly absent from polysomes, consistent with the kinetics of translocation where it only briefly associates with the ribosome during translocation (Liu and Qian, 2016).

Monosomes have previously been thought to be translationally inactive, and only polysomes to be translationally active. This assumption has been reinforced by early studies concluding all peptide synthesis is performed by polysomes, as determined by radioactive amino acid incorporation (Warner and Knopf, 2002; Noll, 2008). In fact, monosomes have been considered so translationally inactive compared to polysomes that translation rates have been defined by the polysome to monosome ratio detected by polysomal translation (Chassé et al., 2017; Lecampion et al., 2016; Yoshikawa et al., 2018). The polysome to monosome ratio in untreated HeLa cell lines has been determined to be ~2.5 (Yoshikawa et al., 2018). The translational inactivity of monosomes has been evidenced by polysome profiling establishing that when stress conditions arise and global translation is repressed, the number of polysomal fractions dramatically decreases and the monosomal fraction increases (Liu et al., 2013). Furthermore, monosomes bound to mRNAs have been presumed to be newly assembled 80S ribosomes at the start codon in the initiation phase that had not moved far enough along the transcript to give ample room to allow for the binding of an additional 80S ribosomes at the 5' end, thus representing an early stage of polysome formation (Heyer and Moore, 2016; Kelen et al., 2009).

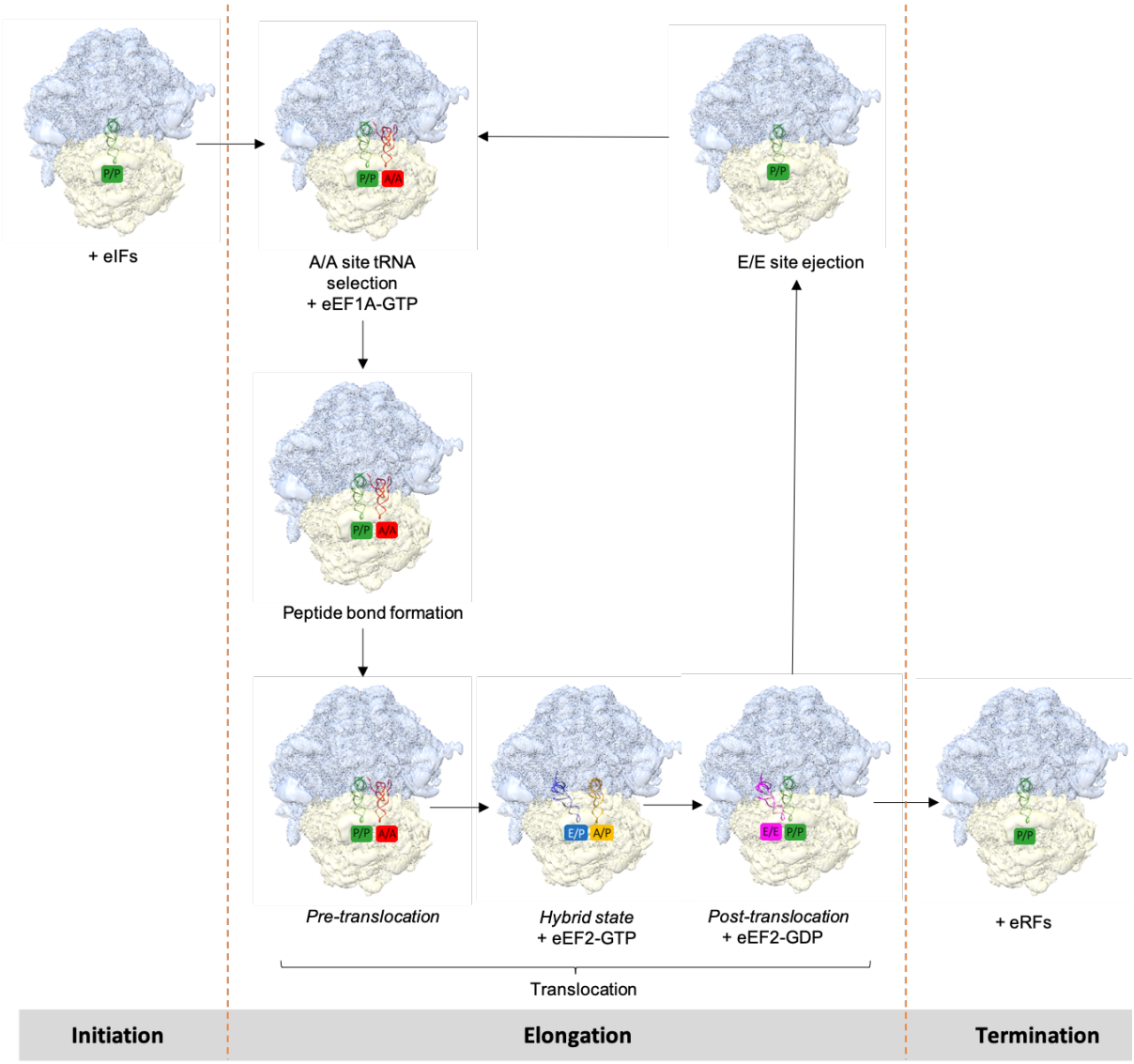

Figure 4. Schematic illustration of tRNA site occupation during the initiation, elongation and termination steps of translation. A/A (red), P/P (green), E/E (pink), A/P (orange) and P/E (blue). Notably, the A/A site tRNA selection, peptide bond formation and pre-translocation states form the same tRNA conformations. However, in the A/A site tRNA selection state, the A/A site tRNA is bound by eEF1A-GTP, whereas the peptide bond formation and pre-translocation states are not associated with EFs but the A/A and P/P sites differ in acetylation. Similarly, the initiation, E/E site ejection and termination form the same tRNA conformation (P/P) but can be differentiated by the presence or absence of eIFs and eRFs.

Figure made with Chimera.

However, there is now evidence that at least some monosomes are in fact actively translating. For example, the translational status of monosomes was investigated in *S. cerevisiae* by comparative analysis of ribosome foot-printing of the monosomes, polysomes and the entire ribosomal population. This ground-breaking series of experiments established that monosomes are not only actively translating but critical for the translation of highly regulated mRNAs (Heyer and Moore, 2016). Monosomal translation was associated with: 1) short open reading frames (ORFs) and nonsense-mediated decay (NMD) mRNA targets (mRNA transcripts with premature stop codons (Nickless et al., 2017); 2) upstream open reading frame (uORF) containing mRNAs (which are present in 5'-UTRs and can regulate translation of the main ORF (mORF) (Barbosa et al., 2013)); and 3) mRNA transcripts of low abundance proteins (Figure 5). Moreover, it was found that the majority of monosomes were engaged in elongation and not initiation, suggesting that these were not 80S ribosomes preceding polysome formation (Heyer and Moore, 2016).

Furthermore, microdissection of adult rodent synapses followed by ribosomal foot-printing, determined that neuronal mRNA transcripts of axonal and dendritic proteins exhibit a preference for monosomal translation (Biever et al., 2020). Notably, these transcripts were established to be high abundance proteins, unusual for monosomal translation, which usually favour translation of lower abundance proteins (Figure 5) (Heyer and Moore, 2016). Therefore, monosomal translation is thought to be employed in this instance for local translation in the axons and dendrites, which due to their size limitations cannot accommodate large polysomes complexes (Biever et al., 2020). This is not the first instance of monosomal translation observed in the brain. An earlier study showed that d-Lysergic acid diethylamide bitartrate (LSD)-induced hyperthermia cellular stress responses caused disaggregation of rabbit brain tissue polysomes and localisation of these mRNAs to monosomes (Cosgrove et al., 1982). Cell free translation assays of monosomes incubated with [^{35}S] methionine, isolated after *in vivo* administration of LSD, determined that a far wider range and quantity of proteins were generated in comparison to untreated control monosomes (Cosgrove et al., 1982). This implies that monosomes generated by stress responses are actively translating and continue to translate when polysomal translation has been inhibited.

1.4 Translational regulation

Unlike transcriptional gene control, translational regulation mechanisms enable the cell to modulate gene expression rapidly and can affect translation of groups of mRNAs that pertain to a particular pathway/function or globally (Hershey et al., 2012). As most cellular processes are catalysed by proteins, translational regulation is vital in facilitating the maintenance of homeostasis and control of cellular proliferation, growth and development (Hershey et al., 2012). Translational control holds key

importance in disease and development enabling highly dynamic responses to the external cellular signals dictating progression of both these processes (Kong and Lasko, 2012). Accordingly, altered translation has been implicated in a diverse range of diseases and developmental disorders, such as blood disorders, cancer and neurological conditions (Ludwig et al., 2014). In fact, human brain tissue has been determined by multidimensional protein identification technology to be the most translationally regulated in comparison to other tissues (Cagney et al., 2005).

Translational regulatory mechanisms are based on two principles: 1) signal-dependent covalent modification of the general translation factors, which mainly impact global translation and 2) *trans*-acting RNA binding factors (RNA-binding factors and miRNAs) that bind to *cis*-regulatory sequences located in the 5' and 3' untranslated region (UTR) of mRNAs, altering translational fates of specific mRNAs (Gebauer et al., 2012). Most translational regulation mechanisms determined thus far have been found to largely occur at the initiation stage (Sonenberg and Hinnebusch, 2009). This is perhaps reflective of the increased number of translational factors in initiation compared to the other stages of translation.

Ribosomes have been traditionally considered invariable in their composition, simply performing the process of protein synthesis without exerting any regulation. However, recent evidence has emerged leading to the notion that ribosomes themselves directly participate in translational regulation (Norris et al., 2021). These 'specialised ribosomes' possess heterogeneity in their composition, thought to enable them to exhibit preference in translating certain subsets of mRNAs (Dalla Venezia et al., 2019). Of note, not all heterogeneity results in specialisation.

1.5 Ribosome heterogeneity

Heterogenous populations of ribosomes have been found to be generated through 6 routes: RP stoichiometry, RP modification, RP paralogs, ribosome associated factors/proteins, rRNA modification and rRNA variation (Figure 6) (Xue and Barna, 2012). Heterogenous ribosomes have been identified in distinct tissues and cell types in a variety of organisms, including yeast, plants, fish, insects, mice and humans (Norris et al., 2021) (Table 1).

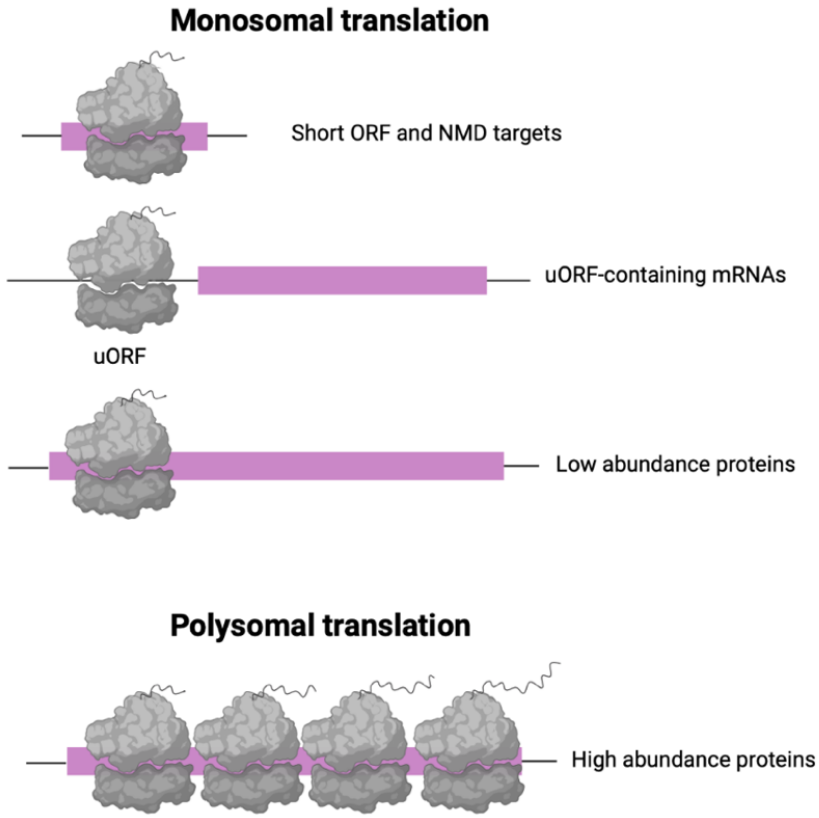

Figure 5. Monosomal and polysomal translation is reflective of mRNA transcripts that they are translating. Monosomal translation has been established to be mostly associated with mRNAs corresponding to short ORFs and NMD targets, uORF containing mRNAs and low abundance proteins. In contrast, polysomal translation is mostly associated with mRNAs corresponding to highly abundant proteins.

Figure adapted from Heyer and Moore, 2016.

RPs provide a major source of ribosomal heterogeneity. As well as varying the stoichiometry of certain RPs, many RPs undergo vast ranges of post-translational modifications (Simsek and Barna, 2017). In addition, some RPs have paralogs, which are two different genes of a specific RP with high similarity but with potentially differing functions, produced by gene duplication events (Gerst, 2018). The number of paralogous RPs is species-specific and can vary enormously. For example, 59 of the 79 RPs have paralogs in *Saccharomyces cerevisiae* (Segev and Gerst, 2018), whereas 19 RP paralog pairs exist in humans (Guimaraes and Zavolan, 2016) and 13 paralogs are present in *D. melanogaster* (Hopes et al., 2021). As well as these core and paralog RPs, ribosome associated factors/proteins can bind to the ribosome RPs or rRNA, further impacting heterogeneity. A huge range of these associated factors exist with many different functions that influence translation (Genuth and Barna, 2018).

rRNA provides another layer of heterogeneity. For example, rRNA variation has been well demonstrated in zebrafish, where it was recently determined that there are maternal-type and somatic-type ribosomes containing distinct rRNAs (Locati et al., 2017). The maternal-type rRNA sequences were found to be highly expressed at oogenesis and gradually were replaced by the somatic-type during embryogenesis. Moreover, *in silico* analysis suggested that the maternal type 18S rRNA preferentially associates with maternally expressed genes (Locati et al., 2017). rRNA modifications include a vast array of post-transcriptional modifications including pseudouridylation, methylation and acetylation (Gerst, 2018). Notably, these covalent additions of chemical moieties to rRNA are not always permanent. These changes have been suggested to be dynamically regulated, supported by the existence of RNA demethylases (Grosjean, 2015). These transient modifications have been determined to regulate rRNA folding or to ensure binding of structural RPs in ribosome biogenesis (D'Souza et al., 2018).

1.6 Ribosomal specialisation via heterogeneity

Specialised ribosomes are defined as heterogeneous ribosomes that have altered translational capacity towards a specific group of mRNAs while retaining the core function of decoding mRNA into amino acids (Ferretti and Karbstein, 2019). The concept of specialised ribosomes soon followed the discovery of the ribosome and has remained a subject of intense debate that has fallen in and out of favour over the last 60 years (Haag and Dinman, 2019).

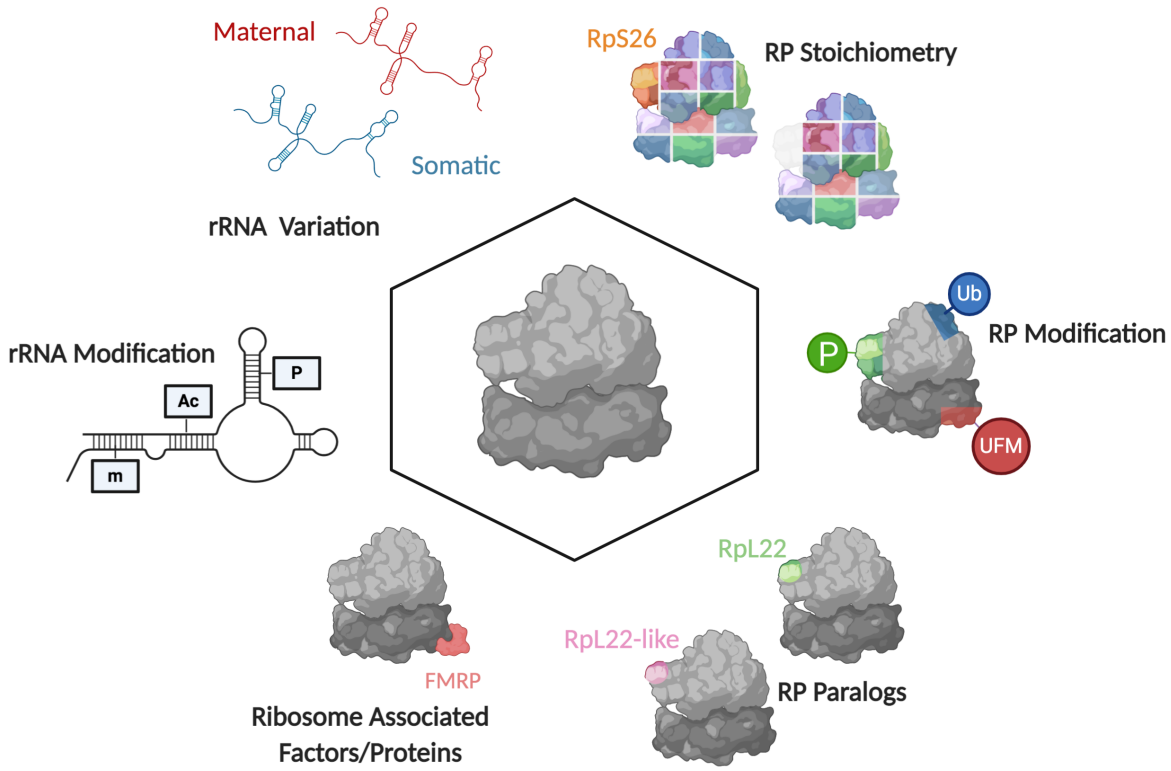

Figure 6. The six defined mechanisms of introducing ribosomal heterogeneity. Ribosomal heterogeneity can arise through six mechanisms by varying the components of the ribosome or that associate with the ribosome: 1) RP stoichiometry, differences in the number of specific RPs included or excluded from the ribosome. 2) RP modification, the post-translational modifications of particular RPs. 3) RP paralogs, highly similar RPs that are incorporated into the ribosome, in favour of another paralog. 4) Ribosomal association of various ribosome associated factors or proteins. 5) Post-transcriptional rRNA modifications. 6) Variation of the sequence of rRNA.

Figure adapted from Norris et al., 2021.

Table 1. Examples of the 6 mechanisms of introducing ribosomal heterogeneity in a variety of eukaryotic organisms

Type of heterogeneity	Example of characterized ribosome heterogeneity	Eukaryotic organism example	Reference
Ribosome Associated Factors	Absence of the RNA binding protein FMRP regulates protein synthesis of target mRNAs leading to abnormal synapse development in the brain and impaired learning and memory.	*Homo sapiens* (Humans)	(Wang et al., 2004)
RP Modification	Ubiquitin fold modifier post-translational modification (UFMylation) identified in mouse embryonic stem cells (mESCs).	*Mus musuclus* (Mouse)	(Simsek et al., 2017)
rRNA Variation	Oocyte specific rRNAs sequences for all 4 rRNAs are expressed and switched to somatic rRNA variants during embryogenesis.	*Danio rerio* (Zebrafish)	(Locati et al., 2017)
Paralogue Enrichment	RpL22-like in testes is highly enriched in polysomes compared to respective paralogue RpL22.	*Drosophila melanogaster* (Fly)	(Mageeney and Ware, 2019)
rRNA Modification	Arabidopsis RPs undergo a variety of covalent modifications including acetylation, methylation and phosphorylation.	*Arabidopsis thaliana* (Arabidopsis)	(Carroll et al., 2008; Turkina et al., 2011)
RP Stoichiometry	In response to high salt and pH conditions yeast cells are depleted of mRNA exit tunnel RP, RpS26.	*Saccharomyces cerevisiae* (Yeast)	(Ferretti et al., 2017)

In 1958 Francis Crick proposed a 'one gene, one ribosome, one protein' hypothesis, suggesting that each cell contains a ribosome for every gene that is specifically tailored for translation of one mRNA into protein (Crick, 1958). This notion was discredited following a series of comprehensive experiments infecting *Escherichia coli* with T4 bacteriophages (Brenner et al., 1961). Bacteriophage mRNA introduced to the cell was determined to associate with bacterial ribosomes and successfully translate bacteriophage proteins. However, no new ribosomes were generated, leading to the conclusion that ribosomes are non-specialised, translating mRNAs present within the cell with equal specificity (Brenner et al., 1961).

The recent rise of the specialised ribosomes concept came through surmounting evidence from multiple groups reporting differences in ribosomal heterogeneity at key developmental points and in different tissues, in several organisms. For example, the amoeba *Dictyostelium discoideum* was found to differentially phosphorylate and methylate RPs in single-celled vegetative and multicellular aggregation competent states (Ramagopal, 1991). The S19, L13, A1, A2, and A3 RPs were found to be phosphorylated in single celled states whereas S20 and A were predominantly phosphorylated in multicellular states (Ramagopal, 1991). In *Brassica napus*, more highly diverse combinations of paralogs were identified in reproductive tissues ribosomal populations, compared to non-reproductive tissues, suggesting functional divergence (Whittle and Krochko, 2009). More recently, in *D. melanogaster* groups of RP paralogs were found to be enriched in the ovary compared to the testis, demonstrating the presence of ribosome heterogeneity in the gonads (Hopes et al., 2021).

The concept of specialised ribosomes is still contentious within the field. Critics have highlighted a lack of assigned physiological roles of specialised ribosomes as well as little mechanistic detail in how ribosome heterogeneity could allow the ribosome to participate in translational regulation. Moreover, it remains largely undetermined how ribosomal composition changes could be regulated (Ferretti and Karbstein, 2019).

1.7 Potential mechanisms of translational regulation by specialised ribosomes

The influence of heterogeneity on ribosomal function to translate specific mRNAs is currently a topic of active research. However, a small number of studies have determined mechanisms through which specialised ribosomes can exert control over mRNA translation.

1.7.1 IRES-like 5'-UTR elements

The most characterised potential specialised ribosome mechanism of translational regulation is internal ribosome entry site (IRES)-like 5'-UTR elements. In conditions such as viral infection or cellular stress, the predominant pathway of translation initiation, cap-dependent translation, is shut down. Proteins synthesised in these conditions harness cap-independent methods of translation initiation such as IRES initiation, where the 40S or 60S subunits can be directly recruited to mRNA via these IRES-like elements rather than at the 5' end (Hertz et al., 2013). RpL38 has been suggested to be required for the translation of certain homeobox (Hox) mRNA transcript translation by recognising and recruiting the RNA regulons present in the 5'-UTRs of these Hox mRNAs, resembling viral IRESes, to the ribosome for translation (Xue et al., 2015). This was based on the findings that disruption of *Rpl38* expression in mice by an 18 kb deletion/insertion of the RpL38 gene results disrupted translation of 8 of 31 homeobox (Hox) mRNAs but does not impact global translation (Kondrashov et al., 2011). The effect of dysregulated expression of RpL38 impacting Hox mRNA translation is apparent in mice causing a functional output phenotype, *'Tail short*', resulting in a short-kinked tail and skeletal patterning defects (Xue et al., 2015). However, very recent work that has not yet been peer reviewed has determined that identification of these IRES-like elements in some of the Hox genes may be resultant of error in the 5'-UTR annotation, leading to a false positive identification of IRES-like elements (Akirtava et al., 2022). Therefore, RpL38 is required for the translation of the 8 Hox mRNA, although the mechanism by which this occurs is not yet clear. Together these studies allude to the pivotal role that specialised ribosomes (and more specifically RPs) could hold in key developmental processes such as embryogenesis.

Similarly, RpL10A was demonstrated to directly interact with the cellular IRES-like elements in mouse embryonic stem cells (mESCs) (Shi et al., 2017). However, whilst the authors successfully showed that ribosomes enriched in RpL10A translate a different subset of mRNAs compared to RpL10A depleted ribosomes; it should be noted that the control and experimental groups utilised different tags (HA and FLAG tagged, respectively) (Shi et al., 2017). This is particularly pertinent as tagging RPs is well known to impact ribosomal function and give rise to phenotypes (Ferretti and Karbstein, 2019). Furthermore, RpS25 has been demonstrated to be required for translation of cellular and viral IRES-containing mRNA transcripts. Knockdown of RpS25, however did not impact cap-independent or significantly impact global translation rates (Hertz et al., 2013). This is highly suggestive that RpS25 influences translation of IRES-containing mRNA transcripts via specialised ribosome mechanisms.

1.7.2 Upstream open reading frame (uORFs)

Another potential specialised ribosome mechanism of translational regulation is through interaction with uORFs. uORFs are present in almost half of all human mRNA transcripts and exert major impacts on gene expression (Barbosa et al., 2013). Many uORFs negatively regulate expression of the mORF and in some cases can trigger decay of the mRNA (Barbosa et al., 2013).

Specific RPs may be required for the translational control of specific mRNAs through uORFs. For example, RpL24, which is located at the interface of the two ribosomal subunits, has been implicated in influencing translation reinitiation, by aiding 60S and 40S subunit association (Nishimura et al., 2005). In plant cells, the cauliflower mosaic virus (CaMV) transactivator (TAV) directs translation reinitiation of mORFs by physical interaction of eIF3 with the 60S subunit, mediated by RpL24 and eIF3g, identified by testing binding of TAV fragments in yeast two-hybrid assays (Park et al., 2001). Increased transient expression of RpL24 enhanced TAV dependent reinitiation but did not impact the first translation initiation event. This was assessed by measuring the relative expression of 2 reporter constructs, one containing one uORF to measure frequency of translation initiation events, the second containing 2 uORFs to measure the frequency of translational reinitiation (Park et al., 2001). In addition, generation of an *Arabidopsis thaliana* rpl24b$^{-/-}$ mutant showed defects in apical-basal gynoecium patterning, a phenotype also seen in mutants of the polycistronic auxin response genes *ETT* and *MP*. Deletion of the uORFs in *ETT* and *MP* partially suppressed this phenotype. Therefore, expression of *ETT* and *MP* may occur through RpL24-dependent translation reinitiation and uORF translation (Nishimura et al., 2005). More recently, in Kaposi's sarcoma associated herpesvirus (KSHV), ribosome profiling demonstrated that depletion of the BUD23 ribosome biogenesis factor reduced association of ribosomes with uORFs in late lytic genes required for efficient translation of the mORF. This resultantly reduced expression of these genes and progression through the lytic cascade, subsequently decreasing production of infectious virions (Murphy et al., 2022). Together these results suggest mechanisms by which ribosomal heterogeneity, by employment of specific RPs, could influence translational control of uORF containing mRNAs.

1.7.3 Other Potential Specialised Ribosome Mechanisms of Action

Specialised ribosomes have also been suggested to alter translation rates of specific mRNAs, through altering RP stoichiometry. Quantitative mass spectrometry of polysome fractions in mESCs and yeast found certain RPs varied in stoichiometry between the more translationally active heavier polysome fractions compared to the light fractions (Slavov et al., 2015). This is suggestive that the certain RPs enriched in the heavier polysome fractions (e.g., RpS21, RpS29 and RpS14) may be required for higher

rates of translation. In addition to differences in RP stoichiometry impacting rates of translation, it has also been established to impact the specific pools of mRNAs translated. For example, in *S. cerevisiae* responses to stess induced RpS26 depletion of ribosomes. Ribosomes with RpS26 were found to preferentially translate highly expressed mRNAs with Kozak sequences (specific nucleic acid motifs around and including the start codon required for efficient translation), whereas the RpS26 depleted ribosomes translate stress repsonse transcripts (Ferretti et al., 2017).

Although not yet determined, it has also been postulated that specialised ribosomes could also impact translation fidelity, and therefore start and stop codon selection of mRNA transcripts; based on the notion of heterogenous ribosomes impacting structural integrity and therefore impacting translation of the mRNA (Ferretti and Karbstein, 2019).

1.8 Tandem mass tag mass spectrometry analysis of ribosome composition

Tandem mass tag mass spectrometry (TMT-MS) utilises isobaric amine reactive stable isotope labelling to enable quantification of differences in protein abundance (Zhang and Elias, 2017). Following fragmentation by trypsin digestion, proteomic samples are separately tagged with TMTs possessing sample specific reporter ions. Thus, TMT-MS allows for multiplexing of multiple samples consisting of complex mixtures of peptides (Zhang and Elias, 2017). Liquid chromatography tandem mass spectrometry (LC-MS-MS) is then used to measure the mass of peptide fragments by determining the mass to charge ratio, typically quantified by measuring the time-of-flight of ions (Zhang and Elias, 2017). Proteomic software identifies the fragments and annotates them with unique peptide IDs. This allows for the relative abundance of individual peptides to be compared between samples in the same mass spectrometry runs (Zecha et al., 2019).

Recent TMT-MS analysis of *D. melanogaster* tissue ribosomes by our group has established that certain RP paralogs are incorporated into ribosomes in a tissue-specific manner, identifying 6 testis-enriched paralogs and 4 ovary-enriched paralogs (with enrichment defined as proteins between tissue ribosome fractions with >1.5-fold change and a *P*-value of <0.05) (Hopes et al., 2021). In addition, this work revealed that RpS11 is significantly enriched in head tissue ribosomes (monosomal and polysomal fractions) in comparison to other tissues (Figure 7A). RpS11 was the only RP significantly enriched in head tissue 80S monosomes in comparison with the testis and ovary tissue 80S monosomes (Figure 7B and C).

1.9 RpS11 and RpS25

RpS11 is located at the region of the 40S subunit furthest from the mRNA channel (Figure 8). The specific role of RpS11 in protein translation is currently undetermined. RpS11 is highly expressed across 6 brain cells in both human and mouse (astrocyte, endothelial, microglial, neuron, oligodendrocyte and oligodendrocyte precursor cell) according to RNA-Seq data (McKenzie et al., 2018). In addition, higher expression of RpS11 has been associated with poorer prognosis in glioblastoma patients and phosphorylation of RpS11 is associated with Parkinson's disease (Yong et al., 2015; Martin et al., 2011). The head tissue specific enrichment of RpS11 in both monosomes and polysomes, as detected by TMT-MS analysis (Hopes et al., 2021), together with its pathological role in neurodegeneration, indicates that RpS11 may be a conserved site of ribosome specialisation in the brain.

RpS25 is located in the head domain of the 40S in the E site and has been identified to directly contact the decoding centre during translation. RpS25 is essential in several forms of unconventional (non-AUG) translation including IRES initiation, repeat associated non-AUG (RAN) translation and ribosomal shunting (Hertz et al., 2013; Yamada et al., 2019). RpS25 knockdown reduces RAN translation (but not general translation) of CAG (Huntington's) and GGGGCC (amyotrophic lateral sclerosis (ALS)) repeats in human and yeast cell lines (Yamada et al., 2019). Knockdown of RpS25 increased lifespan in *D. melanogaster* ALS models and ALS patient induced motor neurons (Yamada et al., 2019). There is strong evidence that RpS25 contributes to specialised mechanisms given its essential role in these forms of translation as well as being determined to be present at sub stoichiometric levels in mESCs (Shi et al., 2017). In contrast to RpS11, TMT-MS analysis found that RpS25 was not significantly enriched in any tissue ribosome fraction; and was detected at comparatively lower levels in head ribosomal fractions than the testis, ovary and embryo (Figure 7A). Therefore, I sought to characterise ribosome heterogeneity in the brain through RpS11 stoichiometry, using RpS25 as a control.

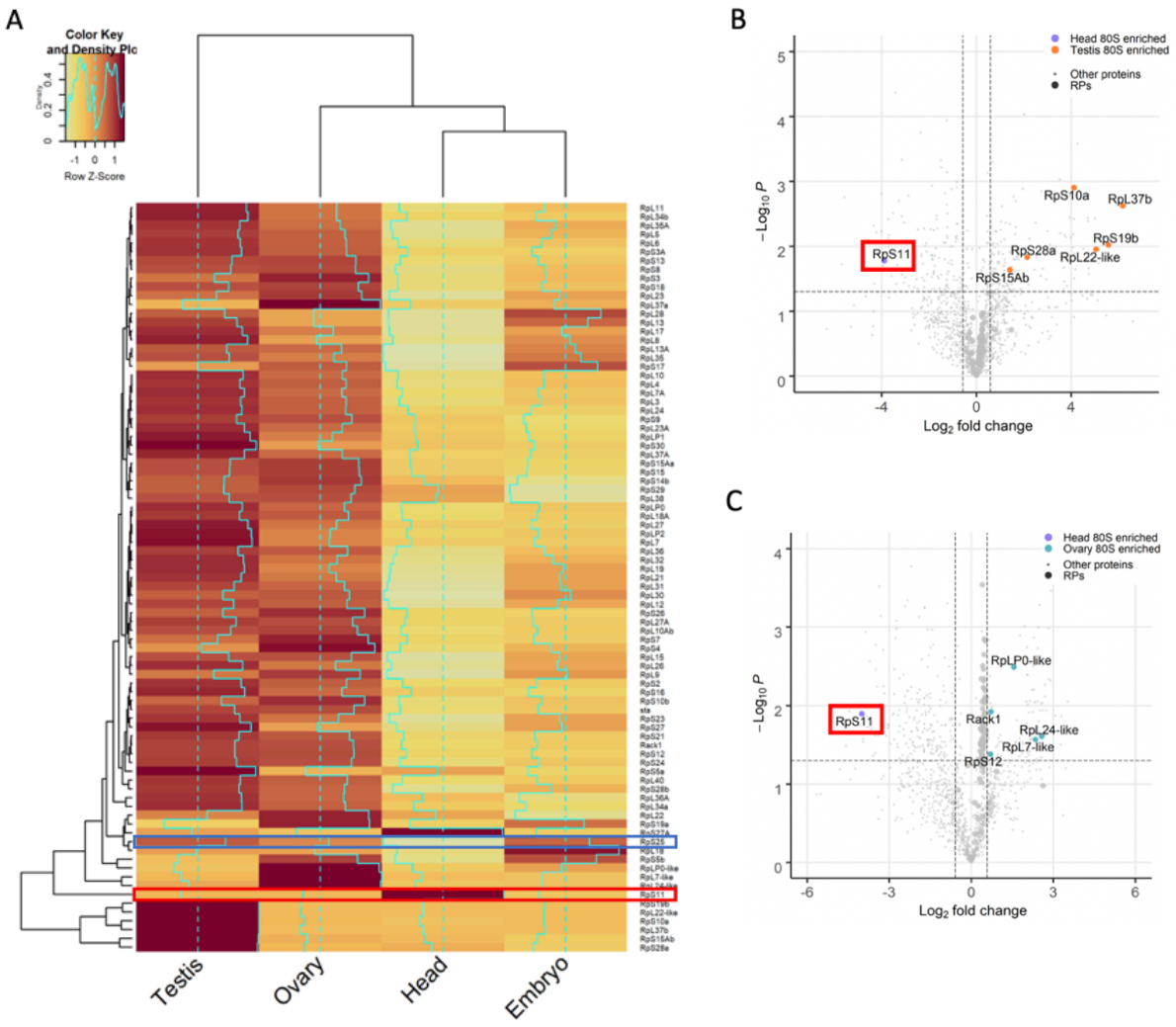

Figure 7. RpS11 is significantly enriched in head ribosomes compared to other tissues. (A) Hierarchical clustering of log_2 normalised RP abundance scaled to a control pool from which Z-scores were calculated and plotted in monosomes from D. melanogaster head, testis, ovary and embryo tissues, detected by TMT-MS, and clustered according to row (RPs). As shown by the key, darker red heatmap squares represent Z-score values closer to 1, whereas yellow squares represent Z-score values closer to -1. Z-values closer to 1 represent RPs more highly expressed in these ribosomal tissue fractions. RpS11 protein expression (outlined in red) shows significant enrichment in the head tissue compared to other fly tissues, whereas RpS25 (outlined in blue) appears to be the lowest expressed 40S RP in the head compared to the other tissues. (B) Volcano plot plotting log_2 fold change of proteins against $-log_{10}P$ values of different D. melanogaster tissue 80S monosomes, detected by TMT-MS. In head tissue monosomes versus testis tissue monosomes, RpS11 (outlined in red) is the only RP significantly ($P < 0.05$) enriched in heads compared to testis. (C) Head tissue monosomes versus ovary tissue monosomes, RpS11 (outlined in red) is the only RP significantly ($P < 0.05$) enriched in heads compared to ovary.

Figure adapted from Hopes et al., 2021.

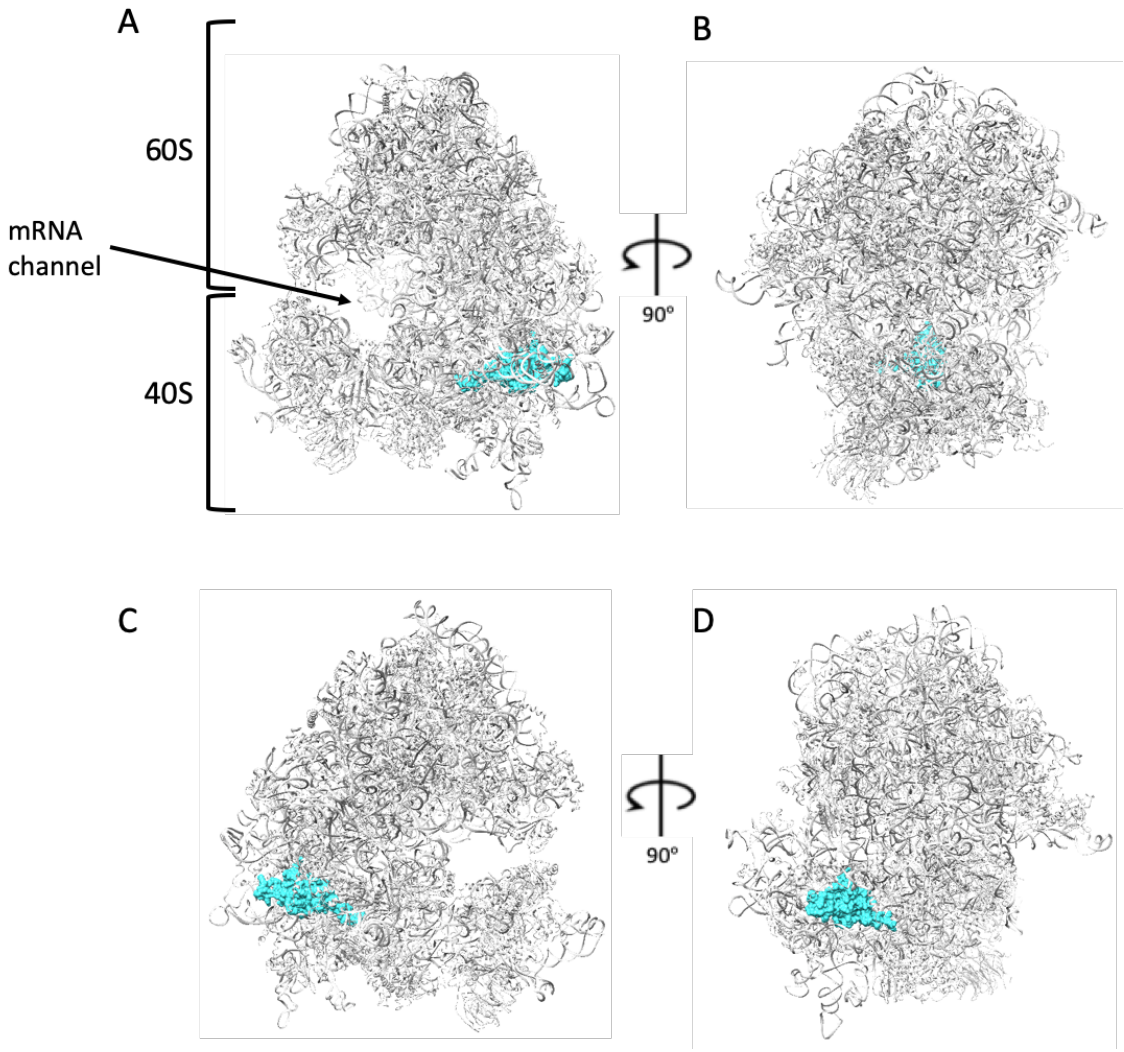

Figure 8. Location of RpS11, mapped onto the *D. melanogaster* ovary 80S monosome atomic model. RpS11, coloured turquoise. Each view represents a 90° rotation about the vertical axis of the 80S ribosome. (A) left side view of 80S head ribosome (B) front view (C) right side view (D) back view. Figure made with UCSF Chimera.

1.10 *D. melanogaster* as a model for the study of the structure and function of ribosome heterogeneity

D. melanogaster is an ideal model to study ribosome specialisation in for several reasons. For example, 60% of *D. melanogaster* protein coding genes have human orthologs, including 75% of genes responsible for human disease (Ugur et al., 2016). In addition, *D. melanogaster* have a high generational turnover and a well characterised genome and anatomy making them incredibly useful model organisms (Jeibmann and Paulus, 2009). Many genetic tools are available to manipulate *D. melanogaster* gene expression, notably the UAS/GAL4 system (Section 2.2), which enables the temporal and spatial expression of genes to be easily manipulated (Jeibmann and Paulus, 2009). The UAS/GAL4 requires the mating of two fly lines, the first expressing the target gene under the control of an upstream activator sequence (UAS) and the second, a GAL4 driver line, a yeast transcription factor driven by a promoter (Duffy, 2002). In the F_1 progeny of the resultant cross, the GAL4 driver controls temporal and spatial of expression of UAS genes (Duffy, 2002). Notably, the disruption of 64 out of 79 cytoplasmic RP genes in *D. melanogaster* can result in the '*Minute*' phenotype, which is characterised as the presence of abnormally short, thin thoracic bristles (Marygold et al., 2007). Several RP mutations associated with the *Minute* phenotype are also accompanied by prolonged development, low fertility and viability, and altered body size. The *Minute* phenotype occurs due to diminished translational capacity during the demanding processes of embryogenesis and in the highly proliferating cells of the bristle organs (Marygold et al., 2007). In addition, TMT-MS data from the Aspden group has established that as well as certain RPs being enriched in the gonads, RpS11 is significantly enriched in *D. melanogaster* head ribosomes compared to other tissues. Furthermore, the published atomic models of *D. melanogaster* ovary 80S monosome, testis 80S monosome and 80 polysome and embryo 80S monosome allow for comparative structural analysis (Hopes et al., 2021; Anger et al., 2013). Therefore, it was concluded that it was extremely appropriate to study ribosomal heterogeneity, structure and function in *D. melanogaster.*

1.11 Aims and Objectives

The aims of this research are to:

1. Assess the potential role of RpS11 in normal brain development in *D. melanogaster*.

2. Dissect the structural effect of RpS11 enrichment in head tissue ribosomes.

3. Determine the translational profile of monosomes across different *D. melanogaster* tissues.

I plan to investigate these aims by completing the following objectives:

a) Verify the enrichment of RpS11 in the head by analysis of RpS11 TMT-MS peptide fragment detection.
b) Knockdown expression of RpS11 in the neurons of *D. melanogaster*, to further understand its role in brain development and neuronal translation.
c) Perform structural analysis by cryo-EM of head-derived *D. melanogaster* ribosomes to investigate RpS11 enrichment in head monosomes.
d) Assess and quantify the translational status of head tissue 80S monosomes in comparison to other *D. melanogaster* tissue ribosomes.

2 Materials and Methods

2.1 TMT-MS peptide fragment analysis

The significant detection of RpS11 in head ribosomes (Hopes et al., 2021), was validated by analysis of RpS11 peptide fragment detection across the *D. melanogaster* tissue ribosomes, in comparison to RpS25. Normalised abundances of each RpS11 and RpS25 peptide fragment were extracted from the 3 TMT-MS data replicates using master protein accession codes (Hopes et al., 2021). The detection of each RpS11 and RpS25 peptide detected by TMT-MS in the *D. melanogaster* tissue ribosomes was analysed using the 'heatmap.2' function from the 'gplots' package on R (Warnes et al., 2016). The heatmap.2 function calculated the Z scores of $\log_{10}$ normalised abundances of each peptide fragment across the *D. melanogaster* tissue ribosomes, which was presented as a heatmap. The heatmap.2 function also performed hierarchical clustering of the Z-scores, clustering them by peptide fragment (row).

The distribution of the RpS11 and RpS25 peptides detected by TMT-MS were mapped to the full-length peptide sequence downloaded from Uniprot manually.

2.2 UAS-GAL4 system

The UAS/GAL4 system was utilised to drive expression of RP-RNAi in GAL4 expressing cells. The *elav*-GAL4 driver was used as elav is expressed in the *D. melanogaster* neurons and most embryonic glial cells (Berger et al., 2007). In these *elav*-GAL4 expressing cells, the GAL4 protein binds to the UAS driving transcription of RP-RNAi, knocking down expression of the RP in those cells (Figure 9).

2.3 Fly growth conditions

D. melanogaster lines used for the UAS-GAL4 crosses (Table 2) were raised in vials on standard sugar, agar, yeast medium (50 g/L sugar, 100 g/L yeast, 10 g/L agar, 0.3% (v/v) propionic acid, 1.97 mM Nipagin M (Bass et al., 2007)), in a humidified constant temperature room at 25 °C with a 12-hour light/dark cycles.

2.4 Crosses

To perform the RP-RNAi mediated knockdown in elav-expressing cells UAS/GAL4 crosses were generated by collecting virgin male and female flies. 10 flies of each sex were placed together into fresh vials, the sugar-agar-yeast medium was scored, and grains of active baker's yeast were added to

promote egg laying (day 1). On days 3 and 6 the flies were flipped into fresh vials and the cross flies were removed from the vial and disposed on day 9. 12 days after mixing parental generation flies (day 15), the F_1 generation adults eclosed from pupae. Progeny were anesthetised with CO_2, selected and segregated by cross specific phenotypes as predicted by punnet squares of each cross (Figures 9-11).

2.5 *D. melanogaster* progeny count

Progeny from each cross were counted to track the progeny genotypes and determine whether expected ratios of each genotype were produced (Figures 10-12).

2.6 Punnet squares

Punnet squares were generated for each *elav*-GAL4 × UAS-RP-RNAi cross, in both directions (i.e., UAS-RP-RNAi male × *elav*-GAL4 female and UAS-RP-RNAi female × *elav*-GAL4 male) to calculate expected ratios of offspring and resultant markers of balancers of each genotype generated (Figures 10-12).

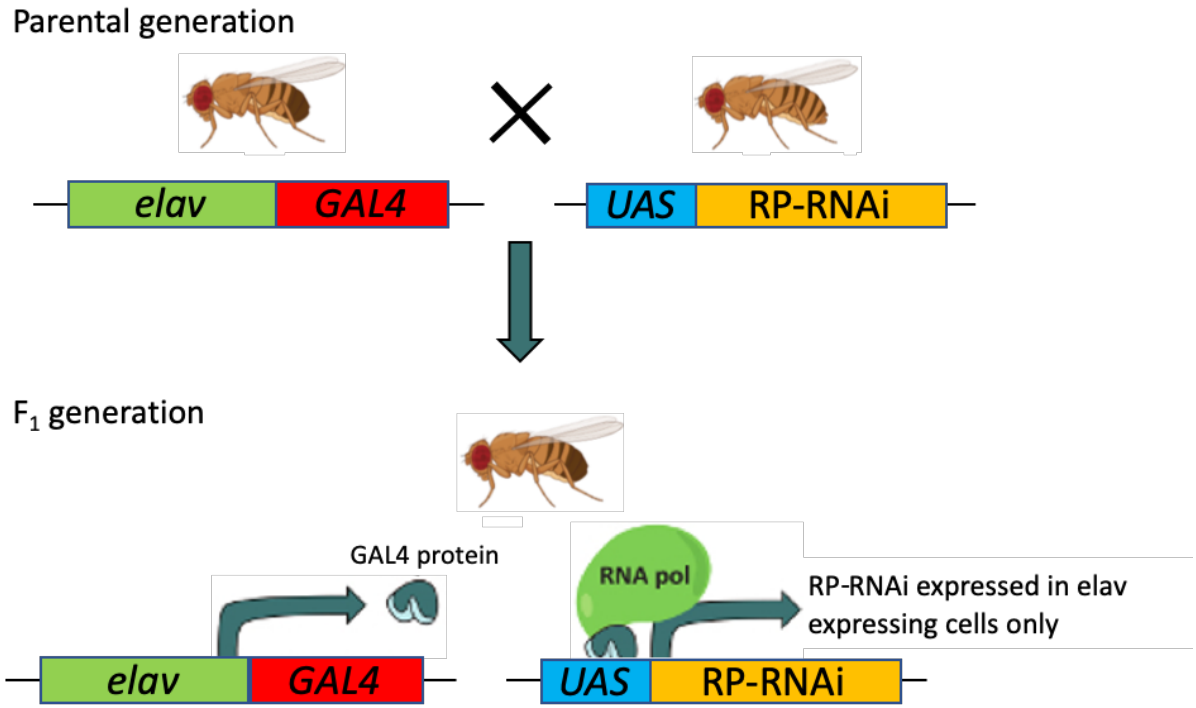

Figure 9. UAS/GAL4 is used drive expression of RP-RNAi elav-expressing cells. In the parental generation *elav*-GAL4 driver lines mate with UAS-RP-RNAi lines. In the F_1 generation this induces expression of GAL4 in elav-expressing cells. The GAL4 protein binds to the UAS of the UAS-RP-RNAi gene, inducing expression of the RP-RNAi in elav-expressing cells, knocking down expression of the RP in neurons and the nervous system.

Figure adapted from Kelly et al. 2017.

Table 2. List of fly lines used, the genotype and source of the line.

Fly line name	Genotype	Source
elav-GAL4	$\frac{elav-GAL4}{CyO}$; $\frac{+}{+}$	Bretman laboratory, University of Leeds
UAS-RpS11-RNAi #23475	$\frac{+}{+}$; $\frac{UAS-RpS11-RNAi}{UAS-RpS11-RNAi}$	Vienna Drosophila Resource Centre (VDRC)
UAS-RpS11-RNAi #23477	$\frac{+}{+}$; $\frac{UAS-RpS11-RNAi}{TM3,Sb}$	VDRC
UAS-RpS25-RNAi #101342	$\frac{UAS-RpS25-RNAi}{UAS-RpS25-RNAi}$; $\frac{+}{+}$	VDRC

2.6.1 *UAS-RpS11-RNAi (#23475) × elav-GAL4*

	elav-GAL4;UAS-RpS11-RNAi expressing progeny

A

$$♂\ \frac{elav-GAL4}{CyO}\ ;\ \frac{+}{+} \times ♀\ \frac{+}{+}\ ;\frac{UAS-RpS11-RNAi}{UAS-RpS11-RNAi}$$

	$elav-GAL4\ ;\ +$	$CyO\ ;+$
$+\ ;UAS-RpS11-RNAi$	$\frac{elav-GAL4}{+}\ ;\ \frac{+}{UAS-RpS11-RNAi}$	$\frac{CyO}{+}\ ;\ \frac{+}{UAS-RpS11-RNAi}$
$+\ ;UAS-RpS11-RNAi$	$\frac{elav-GAL4}{+}\ ;\ \frac{+}{UAS-RpS11-RNAi}$	$\frac{CyO}{+}\ ;\ \frac{+}{UAS-RpS11-RNAi}$

Expectation of progeny from cross:
50% straight wings – *elav*-GAL4;UAS-RpS11-RNAi expressing
50% curly wings (CyO)

B

$$♂\ \frac{+}{+}\ ;\ \frac{UAS-RpS11-RNAi}{UAS-RpS11-RNAi} \times\ ♀\ \frac{elav-GAL4}{CyO}\ ;\ \frac{+}{+}$$

	$+\ ;UAS-RpS11-RNAi$	$+\ ;UAS-RpS11-RNAi$
$elav-GAL4\ ;\ +$	$\frac{+}{elav-GAL4}\ ;\ \frac{UAS-RpS11-RNAi}{+}$	$\frac{+}{elav-GAL4}\ ;\ \frac{UAS-RpS11-RNAi}{+}$
$CyO\ ;\ +$	$\frac{+}{CyO}\ ;\ \frac{UAS-RpS11-RNAi}{+}$	$\frac{+}{CyO}\ ;\ \frac{UAS-RpS11-RNAi}{+}$

Expectation of progeny from cross:
50% straight wings – *elav*-GAL4;UAS-RpS11-RNAi expressing
50% curly wings (CyO)

Figure 10. UAS-RpS11-RNAi #23475 × *elav*-GAL4 genetic cross punnet squares in both directions and expectation of percentage of progeny phenotypes. (A) Male *elav*-GAL4 and female UAS-RpS11-RNAi. (B) Male UAS-RpS11-RNAi and female *elav*-GAL4. Both punnet squares determined that straight winged progeny represented individuals with elav driven RpS11 knockdown. Yellow coloured boxes of the punnet square indicate the genotype of the *elav*-GAL4;UAS-RpS11-RNAi expressing progeny.

2.6.2 *UAS-RpS11-RNAi (#23477) × elav-GAL4*

	elav-GAL4;UAS-RpS11-RNAi expressing progeny

A

$$\male \frac{elav-GAL4}{CyO};\frac{+}{+} \times \female \frac{+}{+};\frac{UAS-RpS11-RNAi}{TM3,Sb}$$

	$elav-GAL4\,;\,+$	$CyO\,;+$
$+\,;\,UAS-RpS11-RNAi$	$\frac{elav-GAL4}{+};\frac{+}{UAS-RpS11-RNAi}$	$\frac{CyO}{+};\frac{+}{UAS-RpS11-RNAi}$
$+\,;\,TM3,Sb$	$\frac{elav-GAL4}{+};\frac{+}{\mathrm{TM3,Sb}}$	$\frac{CyO}{+};\frac{+}{TM3,Sb}$

Expectation of progeny from cross:
25% straight wings, no stubble – *elav*-GAL4;UAS-RpS11-RNAi expressing
25% curly wings (CyO), no stubble
25% stubble (TM3, Sb), straight wings
25% curly wings (CyO) and stubble (TM3, Sb)

B

$$\male \frac{+}{+};\frac{UAS-RpS11-RNAi}{TM3,Sb} \times \female \frac{elav-GAL4}{CyO};\frac{+}{+}$$

	$+\,;\,UAS-RpS11-RNAi$	$+\,;\,TM3,Sb$
$elav-GAL4\,;\,+$	$\frac{+}{elav-GAL4};\frac{UAS-RpS11-RNAi}{+}$	$\frac{+}{elav-GAL4};\frac{\mathrm{TM3,Sb}}{+}$
$CyO\,;\,+$	$\frac{+}{CyO};\frac{UAS-RpS11-RNAi}{+}$	$\frac{+}{CyO};\frac{TM3,Sb}{+}$

Expectation of progeny from cross:
25% straight wings, no stubble – *elav*-GAL4;UAS-RpS11-RNAi expressing
25% curly wings (CyO), no stubble
25% stubble (TM3, Sb), straight wings
25% curly wings (CyO) and stubble (TM3, Sb)

Figure 11. UAS-RpS11-RNAi #23477 × *elav*-GAL4 genetic cross punnet squares in both directions and expectation of percentage of progeny phenotypes. (A) Male *elav*-GAL4 and female UAS-RpS11-RNAi. (B) Male UAS-RpS11-RNAi and female *elav*-GAL4. Both punnet squares determined that straight winged, no stubble progeny represented individuals with elav driven RpS11 knockdown. Yellow coloured boxes of the punnet square indicates the genotype of the *elav*-GAL4;UAS-RpS11-RNAi expressing progeny.

2.6.3 *UAS-RpS25-RNAi (#101342) × elav-GAL4*

	elav-GAL4;UAS-RpS11-RNAi expressing progeny

A

$$\male \frac{elav-GAL4}{CyO};\frac{+}{+} \times \female \frac{UAS-RpS25-RNAi}{UAS-RpS25-RNAi};\frac{+}{+}$$

	$elav-GAL4$	$CyO\ ;\ +$
$UAS-RpS25-RNAi\ ;\ +$	$\frac{elav-GAL4}{UAS-RpS25-RNAi};\frac{+}{+}$	$\frac{CyO}{UAS-RpS25-RNAi};\frac{+}{+}$
$UAS-RpS25-RNAi\ ;\ +$	$\frac{elav-GAL4}{UAS-RpS25-RNAi};\frac{+}{+}$	$\frac{CyO}{UAS-RpS25-RNAi};\frac{+}{+}$

Expectation of progeny from cross:
50% straight wings – *elav*-GAL4;UAS-RpS25-RNAi expressing
50% curly wings (CyO)

B

$$\male \frac{UAS-RpS25-RNAi}{UAS-RpS25-RNAi};\frac{+}{+} \times \female \frac{elav-GAL4}{CyO};\frac{+}{+}$$

	$UAS-RpS25-RNAi\ ;\ +$	$UAS-RpS25-RNAi\ ;\ +$
$elav-GAL4\ ;\ +$	$\frac{UAS-RpS25-RNAi}{elav-GAL4};\frac{+}{+}$	$\frac{UAS-RpS25-RNAi}{elav-GAL4};\frac{+}{+}$
$CyO\ ;\ +$	$\frac{UAS-RpS25-RNAi}{CyO};\frac{+}{+}$	$\frac{UAS-RpS25-RNAi}{CyO};\frac{+}{+}$

Expectation of progeny from cross:
50% straight wings – *elav*-GAL4;UAS-RpS25-RNAi expressing
50% curly wings (CyO)

Figure 12. UAS-RpS25-RNAi #101342 × *elav*-GAL4 genetic cross punnet squares in both directions and expectation of percentage of progeny phenotypes. (A) Male *elav*-GAL4 and female UAS-RpS25-RNAi. (B) Male UAS-RpS25-RNAi and female *elav*-GAL4. Both punnet squares determined that straight winged progeny represented individuals with elav driven RpS25 knockdown Yellow coloured boxes of the punnet square indicates the genotype of the *elav*-GAL4;UAS-RpS11-RNAi expressing progeny.

2.7 *D. melanogaster* tissue ribosome purification and application to cryo-EM grids

All cryo-EM analysis was performed on ribosomes from the head, embryo, testis and ovary tissues of WT *D. melanogaster*. The ribosomes for all of the cryo-EM analysis described in this report were previously derived from harvested WT *D. melanogaster* tissues. Ribosomes were then purified from these tissues and applied to cryo-EM grids. The head and embryo purified ribosome cryo-EM grids were generated by PhD student Amy Turner. The testis and ovary purified ribosomes cryo-EM grids were generated by Tayah Hopes, Michaela Agapiou, Julie Aspden and Juan Fontana using the following protocols, as describe in Hopes et al. (2021).

2.7.1 Tissue harvest (prepared by Aspden and Fontana lab groups)

5 mL of whole flies were snap frozen in liquid nitrogen (LN_2) were subjected to mechanical shock to detach heads. Heads were isolated by passing through a 1 mm mesh filter with LN_2 and transferred to 1.5 mL Eppendorf tubes (Amy Turner). 1.5 g of embryos were collected at 0-2 hours from laying plates (300 mL grape juice concentrate (Young's Brew), 25g agar, 550 mL dH_2O, 10% nipagin). Laying plates were scored and applied with yeast paste consisting of active dried yeast (DCL), plates were placed in cages after pre-clearing for 2 hours. Embryos were washed with dH_2O, dried and flash frozen in LN_2 (Amy Turner). ~500 pairs of testes were harvested from 1- to 4-day-old males in 1× PBS with 2 mM DTT and 1 U/µl RNAsin Plus and flash frozen in LN_2 (Hopes et al., 2021). ~300 pairs of ovaries were dissected from 3-6 day old females in 1× PBS (Lonza) with 1 mM DTT (Sigma) and 1 U/µl RNAsin Plus (Promega) and flash frozen in LN_2 (Hopes et al., 2021).

2.7.2 Ribosome purification (prepared by Aspden and Fontana lab groups)

All stages of ribosome purification were performed on wet ice or at 4°C wherever possible. Heads were transferred to an 8 mL glass Dounce with 3.2 mL lysis buffer A (10 mM Tris-HCl pH 7.5, 150 mM NaCl, 10 mM $MgCl_2$ (Fluka), 2 mM DTT, 1% IGEPAL CA-630 (Sigma), 1% Triton X-100, 200 µg/ml cycloheximide, 2 U/µL Turbo DNAse (Thermo Fisher), 40 U/µL RNAsin Plus, 1× EDTA-free Protease Inhibitor cocktail (Roche), 0.5% DOC) (Amy Turner). Embryos were ground with a pre-chilled loose pestle and mortar in LN_2 and incubated with 5 mL lysis buffer A (Amy Turner). Ovaries and testes were ground using RNase-free 1.5 mL pestles (SLS) in 500 µL lysis buffer B (50 mM Tris-HCl pH 8 (Sigma), 150 mM NaCl, 10 mM $MgCl_2$, 1% IGEPAL CA-630, 1 mM DTT, 100 µg/mL cycloheximide, 2 U/µL Turbo DNase, 0.2 U/µL RNasin Plus, 1× EDTA-free protease inhibitor cocktail) (Hopes et al., 2021). All samples were incubated for 30 minutes with occasional agitation. To obtain the cytoplasmic lysate both head and embryo preparations were centrifuged to remove cell debris at 3,000 × g for 10 min, then twice

at 14,000 × g for 5 minutes (Amy Turner). Ovaries and testes samples were centrifuged at 17,000 × g for 5 min (Hopes et al., 2021).

Cytoplasmic lysates were loaded onto a 18-60% (w/v) sucrose gradient (50 mM Tris pH 8.0, 150 mM NaCl, 10 mM $MgCl_2$, 100 mg/ml cycloheximide, 1 mM DTT, 1× EDTA-free Protease Inhibitor cocktail (Roche)) and ultra-centrifuged in an SW40Ti rotor (Beckman) for 3.5 hours at 170,920 × g at 4°C. Fractions were collected using a Gradient Station (Biocomp) equipped with a fraction collector (Gilson) and Econo UV monitor (BioRad). 80S monosome and polysome fractions were combined. These fractions were concentrated using a 30 kDa column (Amicon Ultra-4 or Ultra-15) at 4°C and buffer exchanged (50 mM Tris–HCl pH 8, 150 mM NaCl, 10 mM $MgCl_2$) until final sucrose ≥0.1%. Samples were quantified using Qubit Protein Assay Kit (Invitrogen) (Amy Turner; (Hopes et al., 2021).

2.7.3 Application to cryo-EM grids (prepared by Aspden and Fontana lab groups)

Purified ribosomes were diluted as required with dilution buffer (50 mM Tris pH 8.0, 150 mM NaCl, 10 mM $MgCl_2$). Copper grids covered with a lacey carbon and an ultrathin layer of carbon (Agar Scientific) were glow discharged for 30 seconds (easiGlow, Ted Pella) and 3 μL of purified ribosomes in 4°C and 95% humidity chamber conditions. Grids were vitrified by plunge-freeing in liquid ethane cooled by liquid nitrogen, using the EM GP plunge freezer (Leica) (Amy Turner; Hopes et al., 2021).

2.8 Head 80S monosome Cryo-EM Analysis

Cryo-EM data collection and image processing were carried out on purified head 80S monosomes to generate 3D structures of these ribosomes, to visualise and perform structural analysis of WT head 80S *D. melanogaster* monosomes to investigate the reported RpS11 enrichment (Hopes et al., 2021). Head 80S monosomes were previously purified and applied to grids as described in section 2.7.

2.8.1 Cryo-EM data collection

Cryo-EM data collection was carried out using FEI Titan Krios (Thermo Fisher) transmission electron microscope with an accelerating voltage of 300 keV. Data was recorded on a Falcon III direct electron detector in integrating mode at a pixel size of 1.065 Å. For the head-derived 80S monosomes a total of 14,827 micrographs were collected with a total electron dose of 60 e/Å^2 partitioned into a dose of 1.37 e/Å^2 per fraction (60 fractions).

2.8.2 Cryo-EM image processing

Cryo-EM image processing was carried out on-the-fly using RELION (v3.1.1) (Thompson et al., 2019; Zivanov et al., 2018). Motion correction and CTF estimation was performed using MOTIONCORR and gCTF, respectively (Zhang 2016; Li et al., 2013). Particles were either autopicked using the RELION Laplacian of Gaussian (LoG) or crYOLO. RELION LoG resulted in 2,711,718 autopicked particles, when using a minimum and maximum diameter for LoG Filter (Å) of 200 and 250. Employing the same micrographs as above, 735,663 particles were picked using crYOLO with the low pass filtered general model. 2 rounds of reference free 2D classification were used to align and classify autopicked particles into 200 classes. 2D classifications were used to iteratively remove 'junk' particles selected from autopicking. After both rounds of 2D classification, the LoG dataset resulted in 1,350,959 particles selected for 3D classification, while crYOLO resulted in 610,605 particles. The previously produced *D. melanogaster* testis 80S ribosome average was used as a reference average for 3D classification (Hopes et al., 2021). For RELION LoG picked particles the three out of five best resolved 3D classes (839,487 particles) were selected for 3D refinement resulting in a 3.1 Å resolution average. This average was post-processed to give a final resolution of 3.0 Å (Section 4.2). For the crYOLO picked particles the four out of five best resolved 3D classes (542,670 particles) were selected for 3D refinement resulting in a 3.2 Å resolution average. This average was post-processed to give a final resolution of 3.0 Å (Section 4.3).

2.9 *D. melanogaster* tissue ribosome cryo-EM datasets

The proportion of 80S monosomes and polysomes engaged in active translation in the *D. melanogaster* head, embryo, testis and ovary tissues was determined by tRNA occupation assessment by focused classification. These datasets were used to contextualise and characterise the level of 80S monosome translation I observed in the head tissue 80S monosomes.

The embryo 80S monosome dataset (11,446 particles) and embryo tissue derived foot-printed 80S polysome dataset (34,603 particles) were previously generated by PhD student, Amy Turner. These datasets were derived from embryo ribosomes collected and purified as described in section 2.7.1 and 2.7.2. The foot-printed 80S polysomes were isolated from pooled polysomal fractions of the embryo extract ribosome purification sucrose gradient and treated with RNAse1 (4 U/AUC) at 4°C overnight. SuperRNAsin was added for 5 minutes at 4°C, preventing over digestion of mRNA. A second ribosome purification step was carried out on this sample as stated in section 2.7.2, isolating the 80S fractions. Fractions were pooled and diluted to <0.1% sucrose and concentrated using Amicon Ultra-4 centrifugal filter units (MWCO 30 kDa) to >200 nM. Cryo-EM data collection and image processing

were carried out on these purified embryo 80S monosomes and embryo 80S foot-printed monosomes applied to copper grids as the method described for head 80S monosomes in sections 2.9.1 and 2.9.2 using RELION autopicking.

The testis 80S monosome dataset (46,878 particles), testis 80S polysome dataset (10,392 particles) and ovary 80S monosome datasets (185,913 particles) were generated from testis and ovary samples isolated as described in section 2.7 and image processed as the method described for head 80S monosomes in sections 2.8.1 and 2.8.2 using RELION autopicking (Hopes et al., 2021).

2.10 Focussed classification

To determine the tRNA occupancy of the head, embryo, testis and ovary *D. melanogaster* tissue ribosome cryo-EM datasets (Table 3), the focused classification was used. The focused classification uses an additional 3D classification step with a mask focussed on an area of variance. The subsequent classification aids resolving and analysing heterogenous cryo-EM datasets by classifying them into homogenous classes (Penczek et al., 2006). 3D refinement was carried out using unbinned particles. Then particles were binned 5 times to expedite image processing (resulting in 5.325 Å pixel size), given that we are looking at features easily distinguished at the maximum resolution achieved (10.65 Å).

2.10.1 Creating the mRNA channel mask

To create the mRNA channel mask used in the focused classification, the following steps were carried out: Firstly, in UCSF Chimera, a 60 Å radius volume erasing sphere was placed at the mRNA channel of the head 80S monosome EM average (Figure 13A, B). All volume outside of the 60 Å radius sphere was erased, with the remaining volume used as the input 3D average to generate a mask with initial binarization threshold of 0.001 (Figure 13C, D). This threshold was deemed appropriate for mask creation, as after expanding the mask, the densities formed a near solid sphere that would include all potential tRNA densities (Figure 13C). Individual masks were generated for each of the other *D. melanogaster* ribosomes using the method outlined for the head 80S monosome in figure 13.

Table 3. Summary of all *D. melanogaster* tissue ribosome cryo-EM datasets analysed by focussed classification to determine and quantify tRNA occupation.

Dataset	Number of particles	Resolution (Å)	Persons responsible for tissue harvest and ribosome purification	Person(s) responsible for cryo-EM grid preparation	Person responsible for generating refined cryo-EM average	Person responsible for classification of translation stages
Head 80S monosome	610,605	3.0	Amy Turner and Tayah Hopes	Juan Fontana	Albert Blandy	Albert Blandy
Embryo 80S monosome	11,446	5.4	Amy Turner and Tayah Hopes	Amy Turner and Juan Fontana	Amy Turner	Albert Blandy
Embryo 80 foot-printed polysome	34,603	4.7	Amy Turner and Tayah Hopes	Amy Turner and Juan Fontana	Amy Turner	Albert Blandy
Testis 80S monosome	46,878	3.5	Michaela Agapiou, Julie Aspden and Tayah Hopes	Juan Fontana	Juan Fontana	Albert Blandy
Testis 80S polysome	10,392	4.9	Michaela Agapiou, Julie Aspden and Tayah Hopes	Juan Fontana	Juan Fontana	Albert Blandy
Ovary 80S monosome	185,913	3.0	Michaela Agapiou, Julie Aspden and Tayah Hopes	Juan Fontana	Juan Fontana	Albert Blandy

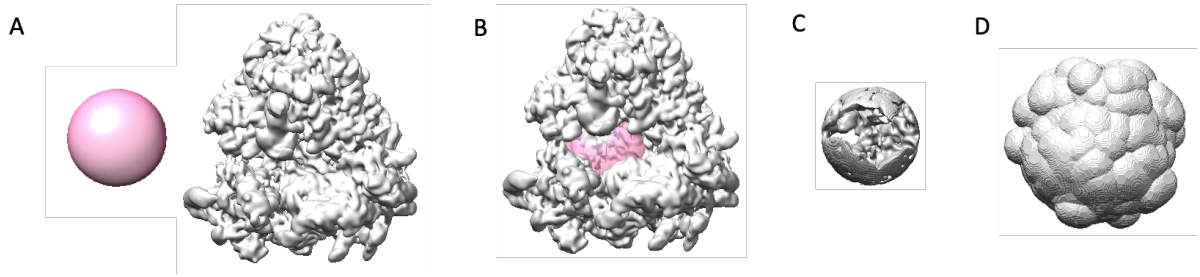

Figure 13. Method used to generate the head 80S monosome mRNA channel mask for the masked focused classification to assess the translational subpopulations. (A) In UCSF Chimera a 60 Å radius volume erasing sphere was generated (pink). (B) This sphere was placed within the mRNA channel of head 80S monosome EM average. (C) The EM densities outside the mask were erased. (D) The resultant volume was extended in RELION, resulting in a mask of ~105 Å radius.

2.10.2 Performing the focussed classification

To perform the focused classification, a 10-class 3D classification jobs were performed for each ribosome sample using the mask around the mRNA channel (Figure 13D). To ensure a more accurate alignment than would have been possible when using a focused mask on a partially occupied region, no alignment was performed in the focused classification job. Therefore, the alignments from the final 3D refinement were employed for all particles. This additionally resulted in faster processing. A further unmasked 3D classification without alignment was carried out on each resultant significant focused class, resolving the full 80S monosome structure whilst maintaining the structural detail from the masked focused classification. This allowed imaging the full 80S monosome reconstruction, aiding orientating and assessing the mRNA channel in the context of the whole 80S monosome structure.

2.11 Atomic modelling

To assess the presence of additional RpS11 densities in the head 80S global average, *D. melanogaster* ovary 80S monosome, testis 80S polysome atomic model structures (Hopes et al., 2021) and embryo extract 80S monosome (Anger et al., 2013) were rigid-body fitted into the average of the head 80S monosome, using the UCSF Chimera 'fit in map' tool (Pettersen et al., 2004).

2.11.1 RpS11 atomic model fitting

To determine if the cryo-EM averages contained densities covering the full RpS11, the testis 80S monosome, testis 80S polysome and ovary 80S monosome atomic models were split and the RpS11 chain was rigid-body fitted into the *D. melanogaster* tissue ribosome averages using UCSF Chimera (Pettersen et al., 2004).

2.11.2 tRNA and IFRD1 atomic model fitting

To confirm the presence of tRNAs in the *D. melanogaster* tissue ribosomes, eukaryotic tRNA atomic models were chosen from variety of organisms, as only the P/P and E/E tRNAs are currently available from *D. melanogaster* ribosome atomic models (Table 4). The IFRD1 atomic model selected from the *D. melanogaster* testis 80S monosome atomic model (Hopes et al., 2021). To ensure the correct orientation of the different tRNAs employed, first the whole atomic model was fitted into the different cryo-EM averages; then each model was split and all the specified tRNAs and IFRD1 atomic were fixed in place to each average to allow for tRNA/IFRD1 occupancy detection assessment. The remaining structure of the global 80S atomic models were deleted.

Table 4. The ribosomal atomic models used for each of the tRNAs fitted to the significant focus classification classes.

tRNA	Atomic model	PDB accession code	Reference
A/A	Yeast (*S. cerevisiae*) 60S ribosomal subunit	5GAK	(Schmidt et al., 2016)
A/P	Rabbit reticulocyte lysate 80S ribosome on globin mRNA in rotated state	6HCJ	(Juszkiewicz et al., 2018)
P/P	*D. melanogaster* testis 80S polysome	6XU7	(Hopes et al., 2021)
P/E	Rabbit reticulocyte lysate 80S ribosome on globin mRNA in rotated state	6HCJ	(Juszkiewicz et al., 2018)
E/E	*D. melanogaster* embryonic extract 80S monosome	4V6W	(Anger et al., 2013)

2.11.3 tRNA and IFRD1 occupancy visualisation

To visualise tRNA occupancy in the mRNA channels of all *D. melanogaster* tissue ribosome significant focused classifications, colour zoned averages were created with UCSF Chimera (Pettersen et al., 2004). The testis 80S polysome atomic model was fitted into each average. The model was subsequently split into the 40S and 60S subunits, which were again rigid body fitted. Visual inspection of the mRNA channel assessed tRNA and IFRD1 occupation or absence. The occupation or absence of relevant tRNA or IFRD1 was visually assessed, and the appropriate tRNA/IFRD1 model was fitted and coloured. All atomic models (60S, 40S, tRNAs and IFRD1), were coloured appropriately, and the colour zone function from UCSF Chimera was employed to colour using a 30 Å radius. The resultant coloured average was split by colour into separate averages and the 40S and 60S subunits were set to 70% transparency to clearly display the tRNAs/IFRD1 from the front 80S view.

In the resolution limited tRNA absent and occupied focused classification classes, only the 40S and 60S subunits were colour zoned and displayed at 0% transparency. These classes were viewed at the left side view to demonstrate tRNA absence or occupancy.

3 Characterising RpS11 enrichment and function in the *Drosophila* brain

3.1 Introduction

The first aim of this project was to assess the potential role of RpS11 in normal brain development in *D. melanogaster*. It had previously been shown that there was significant enrichment of RpS11 in head 80S monosomes and polysomes, compared to other tissues (Hopes et al., 2021). Therefore, I postulated that this enrichment was impacting the stoichiometry of RpS11, i.e. contributing to ribosomal heterogeneity. In glioblastoma patients, higher expression of RpS11 has been associated with poorer prognoses (Yong et al., 2015). Moreover, RNA sequencing analysis across 6 human and mouse brain cells (astrocyte, endothelial, microglial, neuron, oligodendrocyte and oligodendrocyte precursor cell) determined RpS11 was one of the most highly detected mRNAs across all cell types (McKenzie et al., 2018). Together, this is suggestive that RpS11 may facilitate a specialised ribosome mechanism in brain cells, conserved between humans and *D. melanogaster,* impacting translational regulation of head tissue (and more specifically brain) mRNAs. Therefore, I hypothesized that this ribosome heterogeneity, through RpS11 enrichment, could be impacting the proteome of the head tissue through translational regulation. As a first step to test this hypothesis, I sought to perform a detailed investigation of enrichment of RpS11 in head tissue ribosomes detected by TMT-MS. This was to ensure that the RpS11 enrichment was the result of full length RpS11 peptide detection and not the detection of certain RpS11 fragments or a truncated version of RpS11. In addition, I sought to determine whether head tissue could be driving exaggerated RpS11 detection by comparison of the TMT-MS detection of RpS25 peptide fragments as a representative 40S RP not enriched in head tissue, according to the TMT-MS results (Figure 7). Furthermore, to understand the importance of RpS11 enrichment in the *D. melanogaster* head tissue 80S as well as establishing if RpS11 is required for brain development or function, I performed RpS11 RNAi-mediated knockdown in the brain. RpS25-RNAi mediated knockdown was also carried out to compare and contextualise the effect of RpS11 knockdown. Therefore, crosses were performed to knockdown expression of these RPs in the *D. melanogaster* neurons and embryonic glial cells. Any negative changes of knockdown progeny generated compared to the expected ratio could indicate the disruption of translational mechanisms of transcripts vital to brain development and function.

3.2 TMT-MS peptide fragment detection

Global analysis of RP abundances in various *D. melanogaster* tissue and cell culture ribosomes was established by TMT-MS to determine if there was evidence of tissue specific RP stoichiometry contributing to ribosome heterogeneity. TMT-MS analysis found RpS11 to be the only RP significantly enriched in head tissue ribosomes in comparison to the other tissue and cell culture ribosomes analysed (Figure 7 and Hopes et al., (2021)). To verify the significant enrichment of RpS11 detection in head tissue ribosomes, the abundance of the RpS11 peptide fragments detected in each TMT-MS replicate were analysed by hierarchical clustering. I sought to determine if all RpS11-derived peptides were being detected at similar levels in all replicates, or if potentially certain replicates or RpS11 peptide fragments were causing the high level of detection. RpS25 TMT-MS peptide fragment detection was also analysed and used as a comparison to RpS11. RpS25, like RpS11, is a 40S RP and has been shown to have varying levels of RP stoichiometry (Shi et al., 2017). Therefore, I considered RpS25 to be a suitable candidate RP to benchmark peptide detection across the tissue ribosomes. This comparison was aimed to establish if any specific factors were potentially driving an artefactual over detection.

Hierarchical clustering of RpS11 peptide abundances (log_{10} scaled) from TMT-MS replicate 3 showed that all RpS11 peptide fragments were consistently detected highest in the head 80S monosomes and head polysomes. In addition, relative levels between different peptides are similar across different samples of *D. melanogaster* tissue and ribosomes purified from Schneider 2 (S2) cultured cells, derived from late *Drosophila* embryos (Figure 14). Similar results were observed in replicates 1 and 2 (Supplementary figures 1 and 3). This indicated that all RpS11 peptide fragments were detected similarly across replicates. 5 different RpS11 fragment peptides were detected by TMT-MS with coverage mostly towards the N-terminus of the protein sequence (Figure 15). However, there were more trypsin cut sites in the C-terminus, likely suggesting that the production of RpS11 peptides may not be amenable to LC-MS. Therefore, detection of a truncated version of the RpS11 protein cannot be ruled out. Due to TMT-MS replicates being performed separately as the availability of samples and resources was limited, not all 5 peptide fragments were always detected in different replicate runs. For example, only 4 were detected in TMT3, most likely due to experimental variability (Figure 14).

There was a high level of consistency between the RpS25 TMT-MS 2 and 3 replicates (although this was not seen in TMT1), which indicated there was some tissue specific differences in expression of RpS25 (Figure 16, supplementary figures 2 and 4). Replicates 2 and 3 both showed RpS25 was detected at slightly higher levels in the testis and embryo polysomes, therefore suggesting that head tissue

contributing to a higher detection of RPs was very unlikely. In comparison to RpS11, RpS25 detection was less consistent within the different *D. melanogaster* tissue and cell culture ribosome fractions, with certain fragments showing greater differences in the levels of detection across tissues. However, the differences in consistency between RpS11 and RpS25 peptide detection within ribosomes could be attributed to the variation in peptide coverage. In contrast to RpS11, 14 RpS25 peptide fragments were detected across the whole protein sequence (Figure 17).

Together the results of the RpS11 and RpS25 hierarchical clustering analysis suggests that the significant enrichment of RpS11 was most likely a true reflection of higher RpS11 levels in head 80S ribosomes.

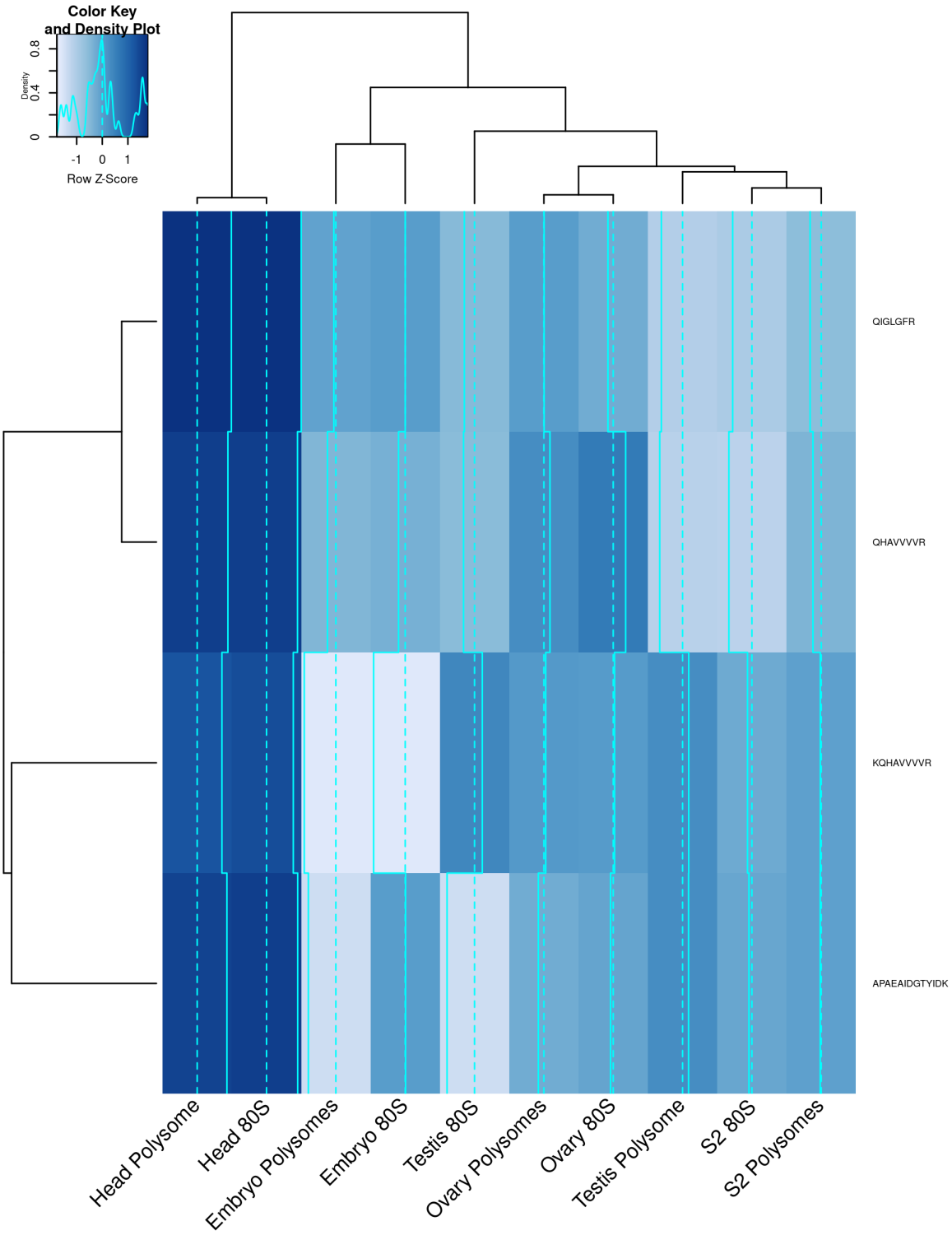

Figure 14. TMT-MS replicate 3 hierarchical clustering of log_{10} scaled normalised abundances of RpS11 peptide fragments in *D. melanogaster* tissue and cell culture ribosomes. Normalised abundances were scaled to a control pool (the average detection of all RP peptide fragments in all ribosome fractions) from which Z-scores were calculated and plotted, rows are clustered according to RpS11 peptide fragments. Peptide fragment normalised abundances were extracted from the TMT-MS data using RpS11 protein (Uniprot accession code A1Z8U9).

***D. melanogaster* RpS11 peptide sequence**

MADQQTE**R**SF**RK**QHAVVVV**RR**K**S**PNL**K**K**R**P**R**FY**R**QIGLGF**R**APAEAIDGTYID**K**K CPWTGDV**R**I**R**G**R**ILTG VV**RK**A**K**MQ**R**TIVI**RR**DYLHFV**RK**YS**R**FE**KR**H**R**NMSVHCSPVF**R**DVEHGDIVTIGEC**R**PLS**K**TV**R**FNVL**K**VS**K** GQGA**KK**SF**KK**

RpS11 peptide fragments detected by TMT-MS

KQHAVVVV**R**

KSPNL**K**

QIGLGF**R**

APAEAIDGTYID**K**

APAEAIDGTYID**K**K

Figure 15. Distribution of the RpS11 peptide fragments detected in TMT-MS analysis across the *D. melanogaster* RpS11 peptide sequence (Uniprot accession ID A1Z8U9). Each colour highlighted sections represents, the peptide fragments generated by trypsin cleavage and detected by TMT-MS. Multiple combination of highlighted colours listed as the peptide fragments detected by TMT-MS represents a different peptide fragment generated by trypsin cleavage plus additional residues. Lysine (K) and arginine (R) residues are underlined and in bold to show the potential sites of trypsin cleavage.

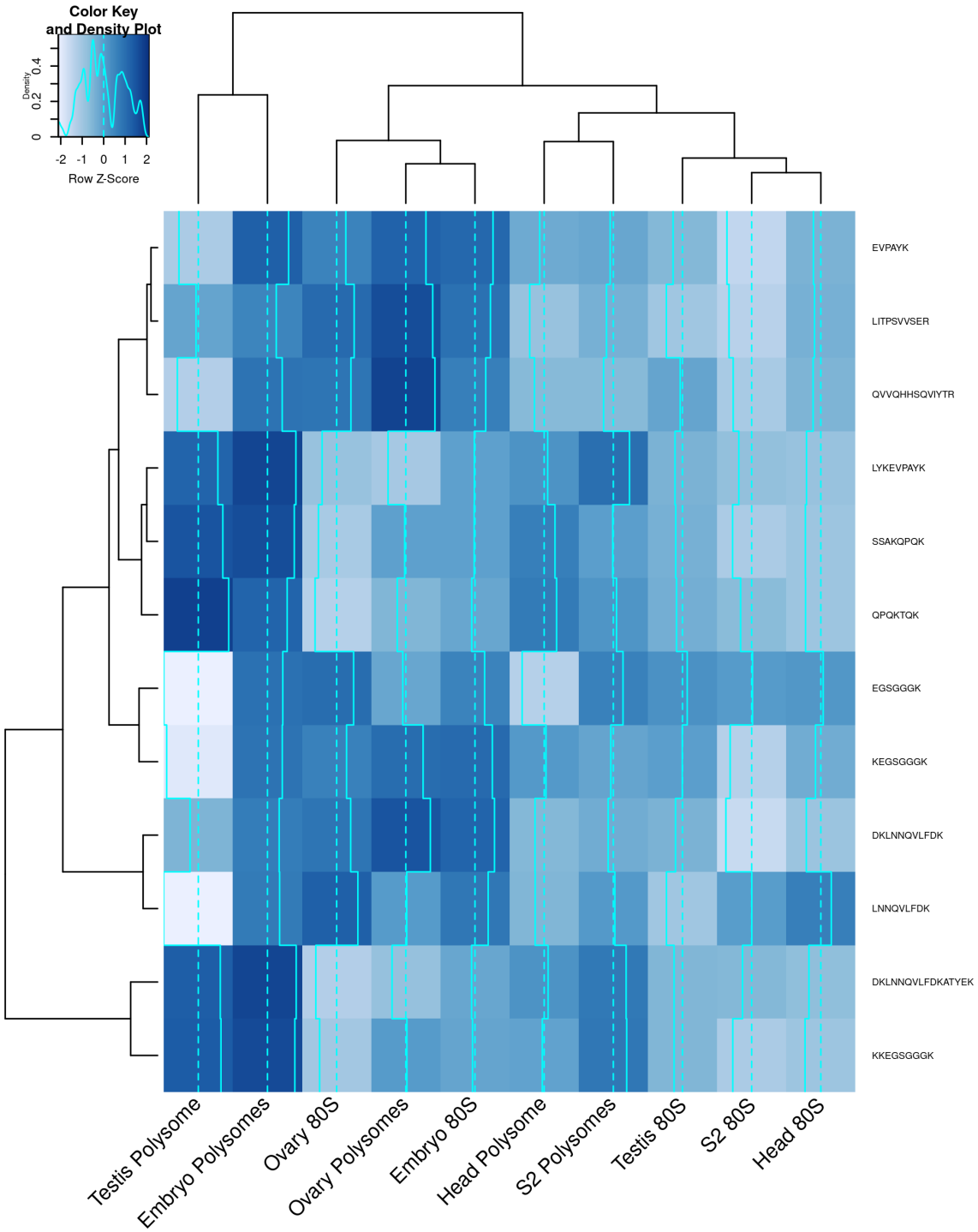

Figure 16. TMT-MS replicate 3 hierarchical clustering of log_{10} scaled normalised abundances of RpS25 peptide fragments in *D. melanogaster* tissue and cell culture ribosomes. Normalised abundances were scaled to a control pool (the average detection of all RP peptide fragments in all ribosome fractions) from which Z-scores were calculated and plotted, rows are clustered according to RpS25 peptide fragments. Peptide fragment normalised abundances were extracted from the TMT-MS data using RpS25 protein (Uniprot accession code P48588).

***D. melanogaster* RpS25 peptide sequence**

MPPKKDAKSSAKQPQKTQKKKEGSGGGKAKKKKWSKGKVRDKLNNQVLFDKATYEKLYKEVPAYKLITPS
VVSERLKIRGSLAKRALIELREKGLIKQVVQHHSQVIYTRATKGDEA

RpS25 peptide fragments detected by TMT-MS

SSAKQPQK
SSAKQPQKTQK
KKEGSGGGK
KEGSGGGK
EGSGGGK
DKLNNQVLFDK
LNNQVLFDK
LYKEVPAYK
LYKEVPAYKLITPSVVSER
EVPAYK
EVPAYKLITPSVVSER
LITPSVVSER
ALIELR
QVVQHHSQVIYTR

Figure 17. Distribution of the RpS25 peptide fragments detected in TMT-MS analysis across the *D. melanogaster* RpS25 peptide sequence (Uniprot accession ID P48588). Each colour highlighted sections represents, the peptide fragments generated by trypsin cleavage and detected by TMT-MS. Multiple combination of highlighted colours listed as the peptide fragments detected by TMT-MS represents a different peptide fragment generated by trypsin cleavage plus additional residues. Lysine (K) and arginine (R) residues are underlined and in bold to show the potential sites of trypsin cleavage.

3.3 RNAi knockdown of RpS11 in *D. melanogaster* nervous system

To establish if RpS11 is essential for brain development or function, I performed RNAi of RpS11 *in vivo*. I crossed UAS-RpS11-RNAi and UAS-RpS25-RNAi *D. melanogaster* lines with *elav*-GAL4, which is a pan neuronal and embryonic glial cell driver line (Berger et al., 2007). RpS25 knockdown was performed as a control. To dissect the importance of RpS11 in the head, the effect of knockdown on numbers of resultant progeny generated for each genotype compared to the ratio expected as calculated by the punnet squares was analysed.

Knockdown of RpS11 was performed with two different UAS-RpS11-RNAi lines, #23475 and #23477, to ensure any effects observed were specific to RpS11 knockdown. Each line differs in the random insertion site of the UAS-RpS11-RNAi construct in chromosome 3 (Dietzl et al., 2007). Both RpS11-RNAi crosses were performed reciprocally, (i.e., performed in both directions: male *elav*-GAL4 flies were crossed with female RpS11-RNAi flies, and female *elav*-GAL4 flies were crossed with male RpS11-RNAi flies). I hypothesised that any decrease in the expected ratio of knockdown progeny compared to no-knockdown progeny would suggest i) RNAi knockdown had been successful and ii) decreased levels of RpS11 affects viability. Thus, indicating that RpS11 is essentially required in embryo brain development. This may be suggestive that RpS11 plays a role in translation of mRNA transcripts required for adult fly brain development. Alternatively, observing the expected progeny could either mean that the knockdown did not work, or that RpS11 knockdown has no effect on viability.

3.3.1 elav driven RpS11-RNAi knockdown with line #23475 has no effect on progeny levels

Crossing UAS-RpS11-RNAi (#23475) × *elav*-GAL4 (Tables 5 and 6, Figures 18 and 19) produced progeny of each genotype closely following the expected ratios (1:1, *elav*-GAL4;UAS-RpS11-RNAi: *CyO*;UAS-RpS11-RNAi (Figure 10)), in both directions of the cross. 3 crosses with 10 virgin females and 10 males were set up for each direction of the cross. Given the enrichment of RpS11 in head tissue monosomal and polysomal fractions, I hypothesised that RpS11 may be playing an essential role in neuronal development and therefore few flies would survive this knockdown. Therefore, despite these crosses producing an abundance of the *elav*-GAL4;UAS-RpS11-RNAi (putative knockdown) flies, the fact that they are produced in an equal ratio to the *CyO*;UAS-RpS11-RNAi (no knockdown) flies could indicate that either RpS11 knockdown has not been achieved or that RpS11 is not important in the nervous system. To distinguish between these two possibilities, validation of the success of the knockdown would be required either by western blot or qPCR.

3.3.2 elav driven RpS11-RNAi knockdown with line #23477 produces no viable RpS11 knockdown progeny

The UAS-RpS11-RNAi (#23477) × *elav*-GAL4 crosses were set up with 3 crosses with 10 virgin females and 10 males were set up for each direction. Crosses in both directions of the cross failed to produce any viable *elav*-GAL4;UAS-RpS11-RNAi progeny (Tables 7 and 8, Figures 20 and 21) and did not follow the expected phenotypic ratio (1:1:1:1, *elav*-GAL4;UAS-RpS11-RNAi: *elav*-GAL4;TM3,Sb: *CyO*;UAS-RpS11-RNAi: *CyO*;TM3,Sb (Figure 11)). This was in agreement with my hypothesis that RpS11 is essential for neuronal development, the generation of no knockdown progeny suggests that both knockdowns have been successful and that RpS11 knockdown leads to a reduction in viability. If knockdown is confirmed, e.g., by western blot or qPCR, it would strongly suggest that RpS11 is globally required for translation of mRNA transcripts in elav-expressing cells, and that its expression is necessary for early embryo development. An alternative explanation could be an unexpected off-target effect of RpS11-RNAi expression.

Table 5. Progeny count of the ♂ $\frac{elav-GAL4}{CyO}$; $\frac{+}{+}$ × ♀ $\frac{+}{+}$; $\frac{UAS-RpS11-RNAi}{UAS-RpS11-RNAi}$ cross, carried out in triplicate. Yellow coloured box indicates the genotype of the *elav*-GAL4;UAS-RpS11-RNAi expressing progeny

Genotype	Sex	Total number of *Drosophila* collected
$\frac{elav-GAL4}{+}$; $\frac{+}{UAS-RpS11-RNAi}$ (straight wings)	♂	129
	♀	134
$\frac{CyO}{+}$; $\frac{+}{UAS-RpS11-RNAi}$ (curly wings)	♂	130
	♀	106

elav-GAL4;UAS-RpS11-RNAi expressing progeny

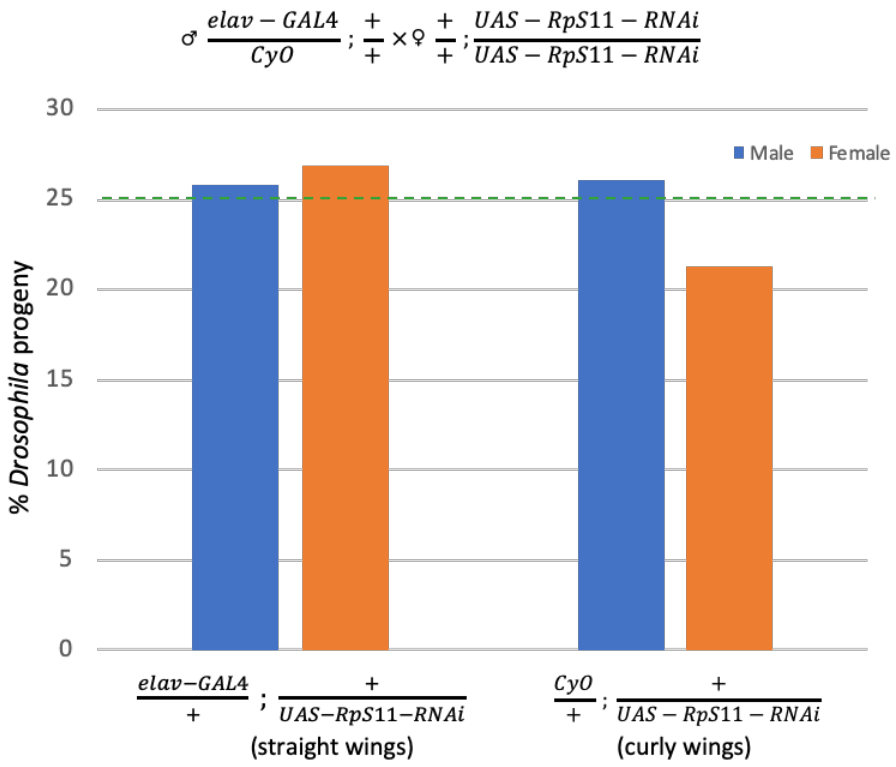

Figure 18. Percentage total resultant progeny of each genotype from the ♂ $\frac{elav-GAL4}{CyO}$; $\frac{+}{+}$ × ♀ $\frac{+}{+}$; $\frac{UAS-RpS11-RNAi}{UAS-RpS11-RNAi}$ cross. Cross was set up in triplicate with 10 adult male $\frac{elav-GAL4}{CyO}$; $\frac{+}{+}$ and 10 adult virgin female $\frac{+}{+}$; $\frac{UAS-RpS11-RNAi}{UAS-RpS11-RNAi}$ flies in each of the 3 vials. Progeny from each genotype were segregated by sex, males (blue) and females (orange). Dashed green line shows the expected percentage of resultant progeny of males and female (25%), as calculated from ratios of each cross progeny expected from punnet square (1:1). As the UAS-RpS11-RNAi element was inserted onto chromosome 3, no differences in the generation of male and female progeny was expected. A difference of >5% would indicate a significant difference of progeny generated than expected.

Table 6. Progeny count of the ♂ $\frac{+}{+}$; $\frac{UAS-RpS11-RNAi}{UAS-RpS11-RNAi}$ × ♀ $\frac{elav-GAL4}{CyO}$; $\frac{+}{+}$ cross, carried out in triplicate.

Yellow coloured box indicates the genotype of the *elav*-GAL4;UAS-RpS11-RNAi expressing progeny.

Genotype	Sex	Total Number of *Drosophila* collected
$\frac{+}{elav-GAL4}$; $\frac{UAS-RpS11-RNAi}{+}$ (straight wings)	♂	132
	♀	131
$\frac{+}{CyO}$; $\frac{UAS-RpS11-RNAi}{+}$ (curly wings)	♂	122
	♀	128

	elav-GAL4;UAS-RpS11-RNAi expressing progeny

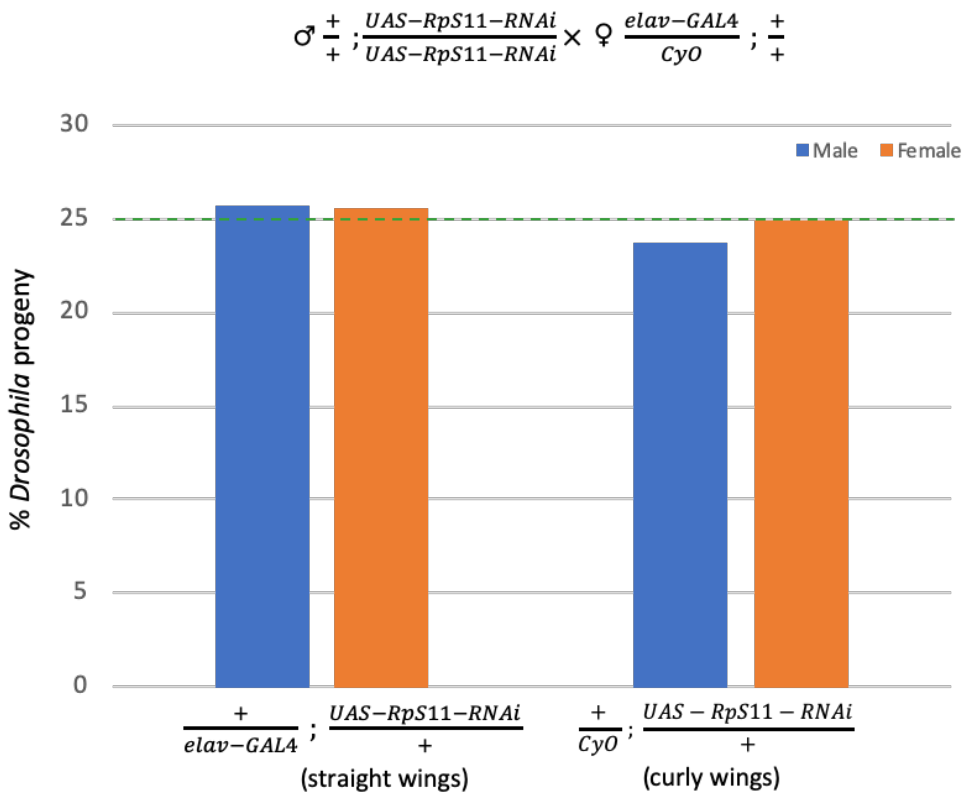

Figure 19. Percentage total resultant progeny of each genotype from the ♂ $\frac{+}{+}$; $\frac{UAS-RpS11-RNAi}{UAS-RpS11-RNAi}$ × ♀ $\frac{elav-GAL4}{CyO}$; $\frac{+}{+}$ cross. Cross was set up in triplicate with 10 adult male $\frac{+}{+}$; $\frac{UAS-RpS11-RNAi}{UAS-RpS11-RNAi}$ and 10 adult virgin female $\frac{elav-GAL4}{CyO}$; $\frac{+}{+}$ flies in each of the 3 vials. Progeny from each genotype were segregated by sex, males (blue) and females (orange). Dashed green line shows the expected percentage of resultant progeny of males and female (25%), as calculated from ratios of each cross progeny expected from punnet square (1:1). As the UAS-RpS11-RNAi element was inserted onto chromosome 3, no differences in the generation of male and female progeny was expected. A difference of >5% would indicate a significant difference of progeny generated than expected.

Table 7. Progeny count of the ♂ $\frac{elav-GAL4}{CyO}$; $\frac{+}{+}$ × ♀ $\frac{+}{+}$; $\frac{UAS-RpS11-RNAi}{TM3,Sb}$ cross, carried out in triplicate. Yellow coloured box indicates the genotype of the elav-GAL4;UAS-RpS11-RNAi expressing progeny.

	elav-GAL4;UAS-RpS11-RNAi expressing progeny

Genotype	Sex	Total Number of *Drosophila* collected
$\frac{elav-GAL4}{+}$; $\frac{+}{UAS-RpS11-RNAi}$ (straight wings, stubble)	♂	0
	♀	0
$\frac{elav-GAL4}{+}$; $\frac{+}{\mathrm{TM3,Sb}}$ (straight wings, stubble)	♂	91
	♀	96
$\frac{CyO}{+}$; $\frac{+}{UAS-RpS11-RNAi}$ (curly wings, no stubble)	♂	79
	♀	113
$\frac{CyO}{+}$; $\frac{+}{TM3,Sb}$ (curly wings and stubble)	♂	51
	♀	35

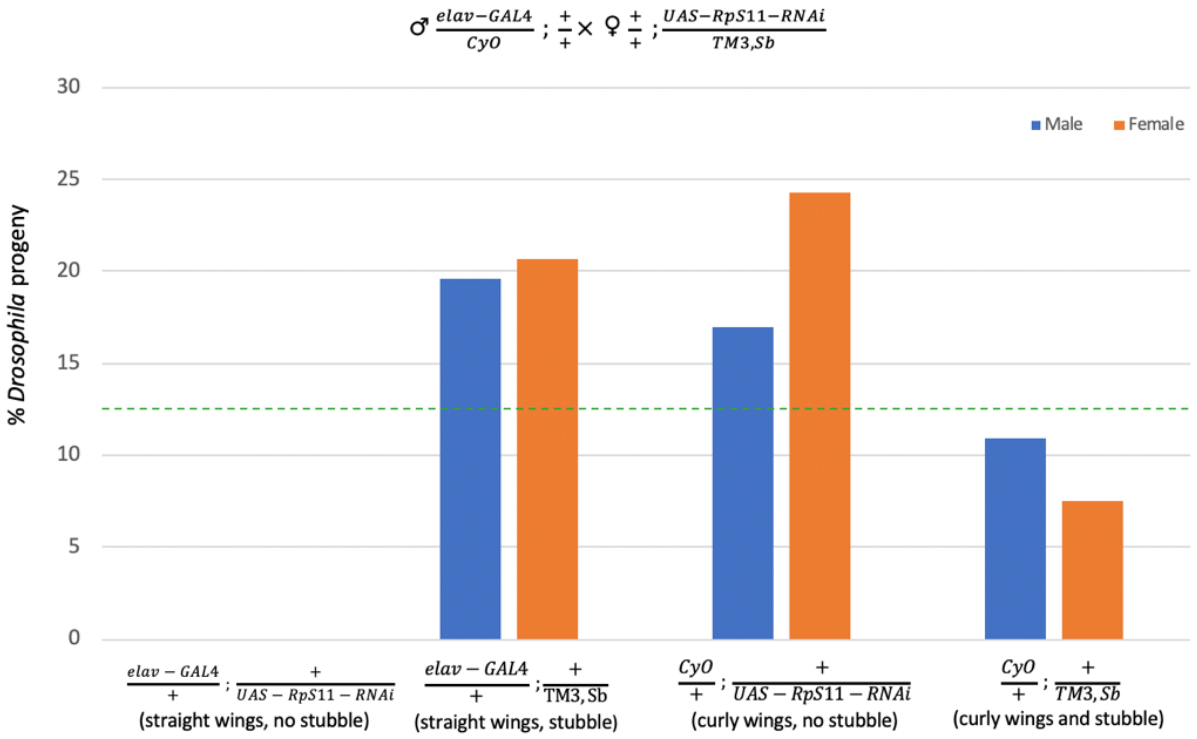

Figure 20. Percentage total resultant progeny of each genotype from the ♂ $\frac{elav-GAL4}{CyO}$; $\frac{+}{+}$ × ♀ $\frac{+}{+}$; $\frac{UAS-RpS11-RNAi}{TM3,Sb}$ cross. Cross was set up in triplicate with 10 adult male $\frac{elav-GAL4}{CyO}$; $\frac{+}{+}$ and 10 adult virgin female $\frac{+}{+}$; $\frac{UAS-RpS11-RNAi}{TM3,Sb}$ flies in each of the 3 vials. Progeny from each genotype were segregated by sex, males (blue) and females (orange). Dashed green line shows the expected percentage of resultant progeny of males and female (12.5%), as calculated from ratios of each cross progeny expected from punnet square (1:1:1:1). As the UAS-RpS11-RNAi element was inserted onto chromosome 3, no differences in the generation of male and female progeny was expected. A difference of >5% would indicate a significant difference of progeny generated than expected.

Table 8. Progeny count of the ♂ $\frac{+}{+}$; $\frac{UAS-RpS11-RNAi}{TM3,Sb}$ × ♀ $\frac{elav-GAL4}{CyO}$; $\frac{+}{+}$ cross, carried out in duplicate. Yellow coloured box indicates the genotype of the *elav*-GAL4;UAS-RpS11-RNAi expressing progeny.

Genotype	Sex	Total number of *Drosophila* collected
$\frac{+}{elav-GAL4}$; $\frac{UAS-RpS11-RNAi}{+}$ (straight wings, stubble)	♂	0
	♀	0
$\frac{+}{elav-GAL4}$; $\frac{\mathrm{TM3,Sb}}{+}$ (straight wings, stubble)	♂	59
	♀	56
$\frac{+}{CyO}$; $\frac{UAS-RpS11-RNAi}{+}$ (curly wings, no stubble)	♂	103
	♀	54
$\frac{+}{CyO}$; $\frac{TM3,Sb}{+}$ (curly wings, stubble)	♂	14
	♀	2

elav-GAL4;UAS-RpS11-RNAi expressing progeny

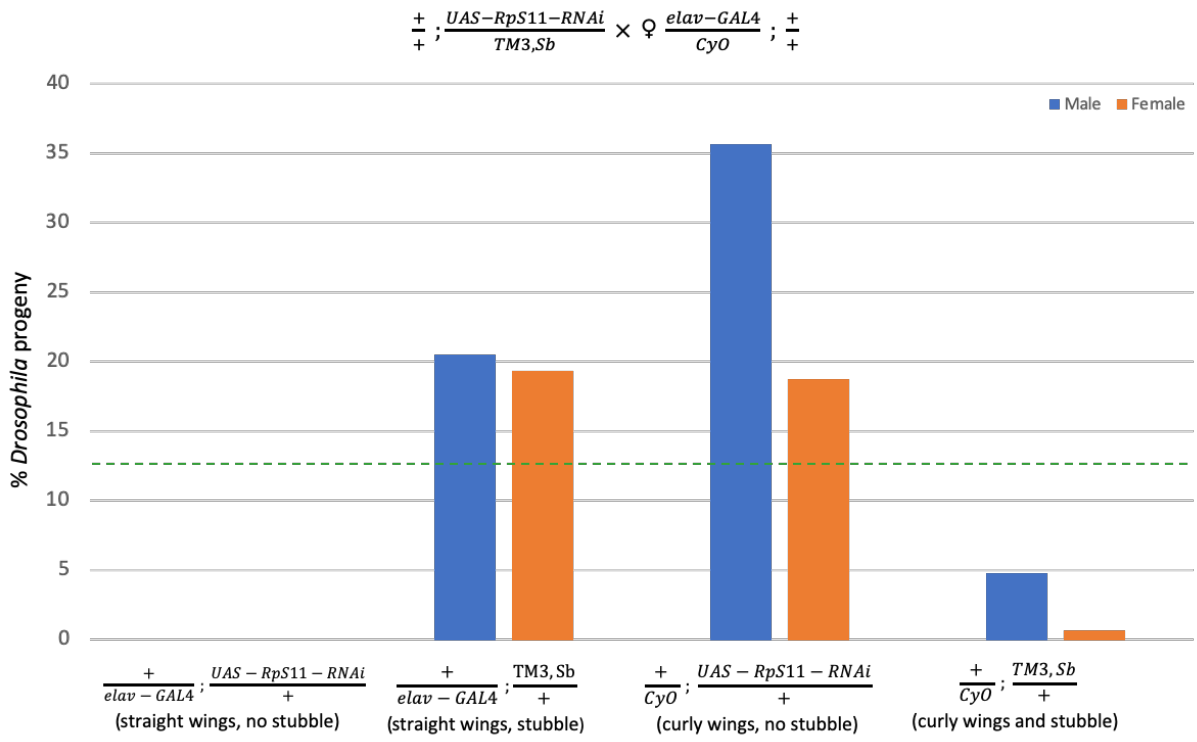

Figure 21. Percentage total resultant progeny of each genotype from the ♂ $\frac{+}{+}$; $\frac{UAS-RpS11-RNAi}{TM3,Sb}$ × ♀ $\frac{elav-GAL4}{CyO}$; $\frac{+}{+}$ cross. Cross was set up in duplicate with 10 adult male $\frac{+}{+}$; $\frac{UAS-RpS11-RNAi}{TM3,Sb}$ and 10 adult virgin female $\frac{elav-GAL4}{CyO}$; $\frac{+}{+}$ flies in each of the 2 vials. Progeny from each genotype were segregated by sex, males (blue) and females (orange). Dashed green line shows the expected percentage of resultant progeny of males and female (12.5%), as calculated from ratios of each cross progeny expected from punnet square (1:1:1:1). As the UAS-RpS11-RNAi element was inserted onto chromosome 3, no differences in the generation of male and female progeny was expected. A difference of >5% would indicate a significant difference of progeny generated than expected.

3.4 RNAi knockdown of RpS25 in *D. melanogaster* nervous system

As with the TMT-MS analysis, RpS25 was used as a control RP. Therefore, elav driven RpS25 knockdown was also performed to contextualise the knockdown results of RpS11. As with the RpS11 knockdowns, any decreases in the ratio of knockdown progeny generated indicates a vital requirement for RpS25 in the development of the brain. This could suggest RpS25 is required for the translation of vitally required mRNA transcripts in embryonic glial and neuronal cells. As with the RpS11 crosses, the RpS25 mediated RNAi crosses were performed reciprocally.

3.4.1 elav driven RpS11-RNAi knockdown with line #101342 reduces the level of knockdown progeny from expected

For the UAS-RpS25-RNAi × *elav*-GAL4 crosses, 3 crosses were set up with 10 UAS-RpS25-RNAi virgin females and 10 elav males, and 2 crosses were set up with 10 UAS-RpS25-RNAi males and 10 *elav*-GAL4 virgin males. Both directions of the UAS-RpS25-RNAi × *elav*-GAL4 crosses (Tables 9 and 10, Figures 22 and 23) produced slightly fewer *elav*-GAL4;UAS-RpS25-RNAi (putative knockdown) flies than *CyO*;UAS-RpS11-RNAi (no knockdown), however this was not greater than 5% decrease for either males or females, so cannot be determined to be significantly different from the expected percentage of progeny generated for this genotype, deduced from the respective punnet squares (1:1, *elav*-GAL4;UAS-RpS25-RNAi: *CyO*;UAS-RpS25-RNAi (Figure 12)). The reciprocal crosses, however did produce a significantly different reduction in putative knockdown flies (Figure 20). This indicates that elav driven RpS25-RNAi likely reduces *D. melanogaster* viability. Although, this would require knockdown confirmation and further investigation to establish this.

Table 9. Progeny count of the ♂ $\frac{elav-GAL4}{CyO}$; $\frac{+}{+}$ × ♀ $\frac{UAS-RpS25-RNAi}{UAS-RpS25-RNAi}$; $\frac{+}{+}$ cross, carried out in triplicate. Yellow coloured box indicates the genotype of the *elav*-GAL4;UAS-RpS11-RNAi expressing progeny.

Genotype	Sex	Total number of *Drosophila* collected
$\frac{elav-GAL4}{UAS-RpS25-RNAi}$; $\frac{+}{+}$ (straight wings)	♂	130
	♀	137
$\frac{CyO}{UAS-RpS25-RNAi}$; $\frac{+}{+}$ (curly wings)	♂	159
	♀	173

elav-GAL4;UAS-RpS25-RNAi expressing progeny

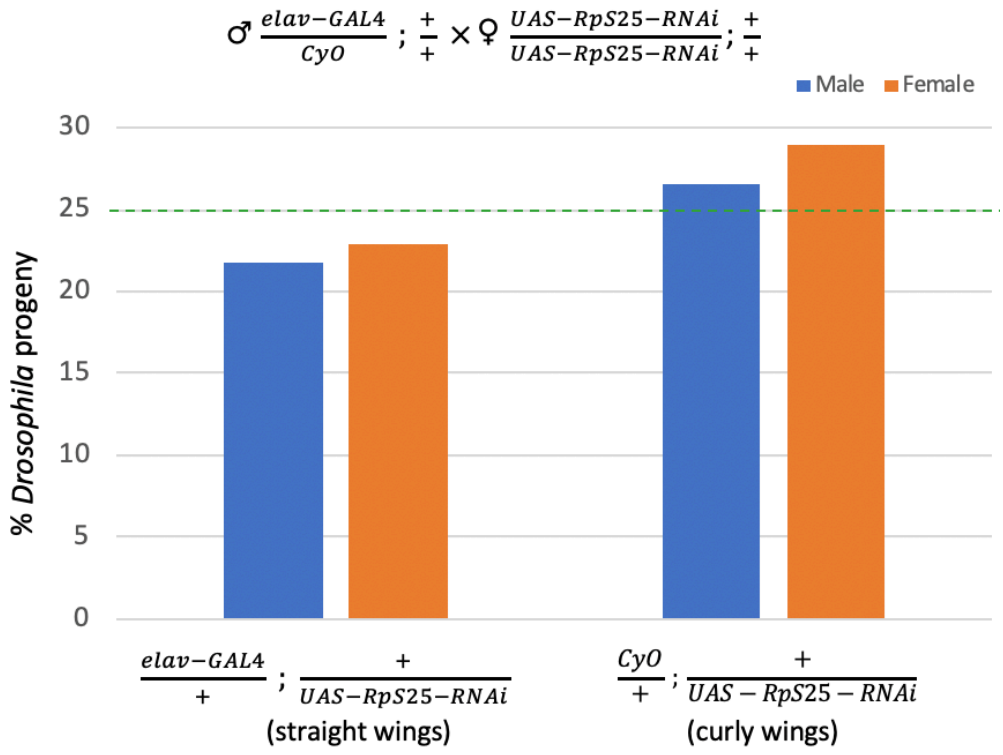

Figure 22. Percentage total resultant progeny of each genotype from the ♂ $\frac{elav-GAL4}{CyO}$; $\frac{+}{+}$ × ♀ $\frac{UAS-RpS25-RNAi}{UAS-RpS25-RNAi}$; $\frac{+}{+}$ cross. Cross was set up in triplicate with 10 adult male $\frac{elav-GAL4}{CyO}$ and 10 adult virgin female $\frac{UAS-RpS25-RNAi}{UAS-RpS25-RNAi}$; $\frac{+}{+}$ flies in each of the 3 vials. Progeny from each genotype were segregated by sex, males (blue) and females (orange). Dashed green line shows the expected percentage of resultant progeny of males and female (25%), as calculated from ratios of each cross progeny expected from punnet square (1:1). As the UAS-RpS25-RNAi element was inserted onto chromosome 2, no differences in the generation of male and female progeny was expected. A difference of >5% would indicate a significant difference of progeny generated than expected.

Table 10. Progeny count of the ♂ $\frac{UAS-RpS25-RNAi}{UAS-RpS25-RNAi}$; $\frac{+}{+}$ × ♀ $\frac{elav-GAL4}{CyO}$; $\frac{+}{+}$ cross, carried out in duplicate. Yellow coloured box indicates the genotype of the *elav*-GAL4;UAS-RpS11-RNAi expressing progeny.

Genotype	Sex	Total Number of *Drosophila* collected
$\frac{UAS-RpS25-RNAi}{elav-GAL4}$; $\frac{+}{+}$ (straight wings)	♂	27
	♀	39
$\frac{UAS-RpS25-RNAi}{CyO}$; $\frac{+}{+}$ (curly wings)	♂	109
	♀	84

	elav-GAL4;UAS-RpS25-RNAi expressing progeny

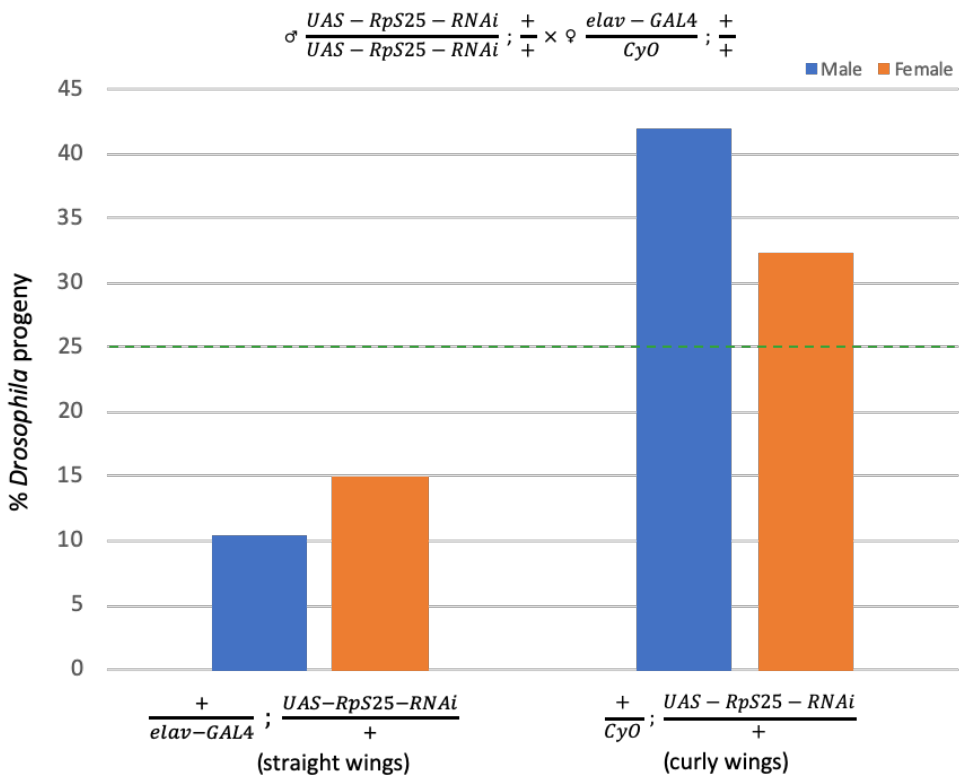

Figure 23. Percentage total resultant progeny of each genotype from the ♂ $\frac{UAS-RpS25-RNAi}{UAS-RpS25-RNAi}$; $\frac{+}{+}$ × ♀ $\frac{elav-GAL4}{CyO}$; $\frac{+}{+}$ cross. Cross was set up in triplicate with 10 adult male $\frac{UAS-RpS25-RNAi}{UAS-RpS25-RNAi}$; $\frac{+}{+}$ and 10 adult virgin female $\frac{elav-GAL4}{CyO}$; $\frac{+}{+}$ flies in each of the 3 vials. Progeny from each genotype were segregated by sex, males (blue) and females (orange). Dashed green line shows the expected percentage of resultant progeny of males and female (25%), as calculated from ratios of each cross progeny expected from punnet square (1:1). As the UAS-RpS25-RNAi element was inserted onto chromosome 2, no differences in the generation of male and female progeny was expected. A difference of >5% would indicate a significant difference of progeny generated than expected.

3.5 Discussion

The first aim of this project was to assess the potential role of RpS11 in normal brain development in *D. melanogaster*. Firstly, I addressed this by performing RpS11 peptide fraction analysis of the TMT-MS data, to confirm increased RpS11 detection in head tissue ribosomes in comparison to other tissues (Hopes et al., 2021). Then the role of RpS11 ribosomal heterogeneity in the *D. melanogaster* nervous system was assessed by performing RNAi knockdown of RpS11.

3.5.1 Confirmation of RpS11 detection by TMT-MS

It was determined that overexpression of RpS11 in head tissue ribosomes is consistent across replicates, and not dependant on an individual peptide, reinforcing the previous conclusions from TMT-MS analysis (Hopes et al 2022). This is not seen in RpS25 peptide fragment analysis, which is expressed more equally across different tissues. However, as the RpS11 peptide fragments were mostly situated at the N-terminal (Figure 15), there is some level of doubt that this is full length RpS11 peptide sequence detection. This is in contrast to RpS25, a smaller peptide, that TMT-MS analysis detected more peptide fragments across the whole length of the peptide (Figure 17). As these peptide fragments were generated by trypsin digestion, this is perhaps reflective of the RpS25 sequence having more trypsin cleavable sites throughout its peptide sequence. Although, this seems unlikely as trypsin digests amino acids between the carboxyl group of arginine (R) and lysine (K) residues and the amino group of the adjacent amino acid (Simpson, 2006). Both R and K residues are well distributed throughout the RpS11 peptide sequence with more R and K residues at the C-terminus (Figure 15). As previously stated, this could suggest that the production of RpS11 peptides is not amenable to LC-MS. It is also possible that this could be resultant of an under representation of RpS11 peptide fragments in the proteomic software used to analyse these TMT-MS data.

The literature supports this now confirmed enrichment of RpS11 in the head/brain. RNA sequencing analysis across 6 human and mouse brain cells (astrocyte, endothelial, microglial, neuron, oligodendrocyte and oligodendrocyte precursor cell) determined RpS11 mRNA was highly detected across these cell types (McKenzie et al., 2018). High expression of RpS11 correlates with poorer prognosis in glioblastoma patients (Yong et al., 2015). However, the high expression found across brain cells and association with glioblastoma may be resultant of an extra ribosomal role of RpS11. Several RPs, (e.g., RpS3, RpS9, RpS19, RpL13a and RpL7) have been established to have extra ribosomal roles impacting processes vital roles which are often disrupted in cancer, including cell cycle regulation, cell proliferation, apoptosis and DNA repair (Chen and Ioannou, 1999; Yamamoto, 2007; Wool, 1996).

3.5.2 RpS11 RNAi knockdown in the brain

The two RpS11-RNAi line crosses produced different results. The #23475 RpS11-RNAi cross resulted in the expected ratio of progeny (Tables 5 and 6, Figures 18 and 19), suggestive of either that knockdown was unsuccessful or RpS11 does not play an essential role in brain development. The #23477 RpS11-RNAi cross produced no knockdown progeny, suggesting knockdown leads to a reduction in viability (Tables 7 and 8, Figures 20 and 21), potentially through disruption of translational mechanisms and suggesting that RpS11 may be essential for neurodevelopment. If knockdown was confirmed, this would suggest that RpS11 is required for global translation, rather than translation of specific subsets of mRNAs that is expected of a specialised translation mechanism. However, knockdown of the RpS11 (#23477 line) is impossible to confirm since no knockdown progeny were generated. It could be possible multiple copies of RpS11 protein (as is hypothesised and unable to be confirmed in the cryo-EM analysis (Section 4)) are present in elav-expressing cells, with the canonical RpS11 facilitating general translation and the additional copies playing a role in a specialised ribosome mechanism. Therefore, successful knockdown (as the *elav*-GAL4 $\times$ UAS-RpS11-RNAi (#23477 line) is suggested to be) would disrupt all translation if all copies were knocked down, without alluding to disruption of a specialised ribosomal translation mechanism. If RpS11 was disrupting general translation, this would suggest RpS11 is essential for the normal function of the ribosome in head tissue.

In contrast to our expectation that RpS11 knockdown would reduce viability in *D. melanogaster*, when knocked down by RNAi in *Caenorhabditis elegans*, 3 studies have shown that this results in a 25-30% increase in life span, although these studies did not assess the impact on translation (Reis-Rodrigues et al., 2012; Hansen et al., 2007; Curran and Ruvkun, 2007). However, these knockdowns were performed on worms that have already reached adult hood, so the impact of this knockdown on brain development cannot be assessed, although increase in lifespan has been determined to be associated with reduced translation in *C. elegans* (Hipkiss, 2007). As both *C. elegans* and *D. melanogaster* are eukaryotes, their translational mechanisms are likely to be conserved.

3.5.3 RpS25 RNAi knockdown in the brain

However, for the RpS25 RNAi knockdown the proportion of knockdown progeny was less than expected, and significantly different in one direction of the cross, indicating that in this direction successful knockdown of RpS25 was achieved and that it reduces *D. melanogaster* viability (Table 9 and 10, Figures 22 and 23). This was an expected result, given the requirement of RpS25 for several forms of non-AUG translation (Hertz et al., 2013). Moreover, RpS25 has been detected at substoichiometric levels in mESCs and knockdown of RpS25 has previously been determined not to

impact cap dependent translation (Shi et al., 2017; Hertz et al., 2013). Therefore, the reduction in the expected number of viable RpS25 progeny indicates that RpS25 could facilitate translation of specific transcripts in the brain required for viability. However, future work should include the confirmation of knockdown by qPCR or western blot for a definitive assessment of knockdown success, where possible.

RpS11 and RpS25 have been identified as RPs that heterozygous deletion of their genes results in the *Minute* phenotypes of shorter thinner thoracic bristles as well as reduced body size, prolonged development and lower viability and fertility (Marygold et al., 2007). Therefore, successful elav driven RP-RNAi knockdown could result in production of the *Minute* phenotypes, although this seems unlikely as knockdown only occurred in the elav-expressing cells and not the whole organism. During progeny collection of elav driven RP-RNAi no noticeable difference in size of the knockdown progeny flies or thoracic bristles was determined by visual inspection compared to no knockdown progeny, however the difference in size was not quantified. A reduction of viability could only be confirmed in the RpS25-RNAi knockdown, although the RpS11-RNAi (#23477) did not produce any viable progeny. However, as previously discussed, it is undetermined if this was a direct effect of knockdown or off target effect. To confirm presence or absence of the *Minute* phenotype, once knockdowns were confirmed in the progeny producing crosses (elav driven RpS11-RNAi #23475 and RpS25-RNAi crosses), each of these crosses should be repeated and the size of the knockdown progeny could be quantified by measuring the mass and length compared to no knockdown progeny. Furthermore, the impact of knockdown on fertility could be assessed by assessing the fertility of male and female knockdown progeny with WT flies by the number of viable progeny generated.

In conclusion, RpS11 detection by TMT-MS has been validated and is resultant of detection of at least the N-terminal region of the protein. The role this form of ribosomal heterogeneity in normal brain development is inconclusive due to the contradictory results of the crosses performed with the different UAS-RpS11-RNAi lines. However, the most reasonable explanation of the RpS11-RNAi knockdown data is that RpS11 is likely essential for all translation in elav-expressing cells. Confirmation of these knockdowns and further analysis is required to determine the role of RpS11 in the translation of brain transcripts.

4 Investigating structural consequences of RpS11 enrichment in head ribosomes by cryo-EM

4.1 Introduction

The second aim of this project was to dissect the structural effect of RpS11 enrichment in head tissue ribosomes. I was intrigued by the structural impact of the now validated significant enrichment of RpS11 in head ribosome detection by TMT-MS. It could be possible that the high detection of RpS11 peptides in the head tissue ribosomes was due to an additional copy of RpS11 residing in a position of the 80S ribosome, in addition to the canonical RpS11 location (Figure 8). Of note, ribosomes with additional copies of RPs, as well as those lacking specific RPs have previously described (Kišonaitė et al., 2022; van de Waterbeemd et al., 2018). It was also postulated that enrichment of RpS11 may result in an altered conformations or structural locations of the canonical RpS11, compared to other *D. melanogaster* ribosomes. To this end, I sought to resolve the structure of adult *D. melanogaster* head 80S monosomes by single particle cryo-EM analysis to deduce the location(s) of RpS11 and dissect structural implications of the RpS11 enrichment. I presumed that any additional copies present in the head 80S monosome 3D average would be clearly detected by overlaying the atomic model of the ovary 80S monosome and testis 80S polysome, in which RpS11 was not enriched.

4.2 Cryo-EM image processing of RELION autopicked particles results in a 3.0 Å final resolution

To determine the structural consequences of RpS11 enrichment in head ribosomes, single particle cryo-EM was performed on purified head 80S monosomes on previously generated grids by Juan Fontana. A Krios microscope operated at 300 kV and equipped with a Falcon III camera was used for this, and a dataset of 14,827 micrographs was obtained. From this dataset, 2,711,718 particles were autopicked by the RELION software based on a LoG filter with a minimum and maximum diameter for LoG Filter (Å) of 200 and 250 (Zivanov et al., 2018). This LoG function searches the micrographs for particles with edges that fit within the 200-250 Å diameter of a circle. 2 rounds of 2D classification were then performed to remove non-ribosome ('junk') particles, resulting in ~1.35M particles. These particles where then 3D classified into 5 classes, resulting in 3 classes containing ribosome particles (~850,000 particles), which were then refined using the *D. melanogaster* testis 80S average (Hopes et al., 2021) filtered to 375 Å to reduce reference bias. This resulted in a 3.0 Å 3D average (Figures 24 and 25).

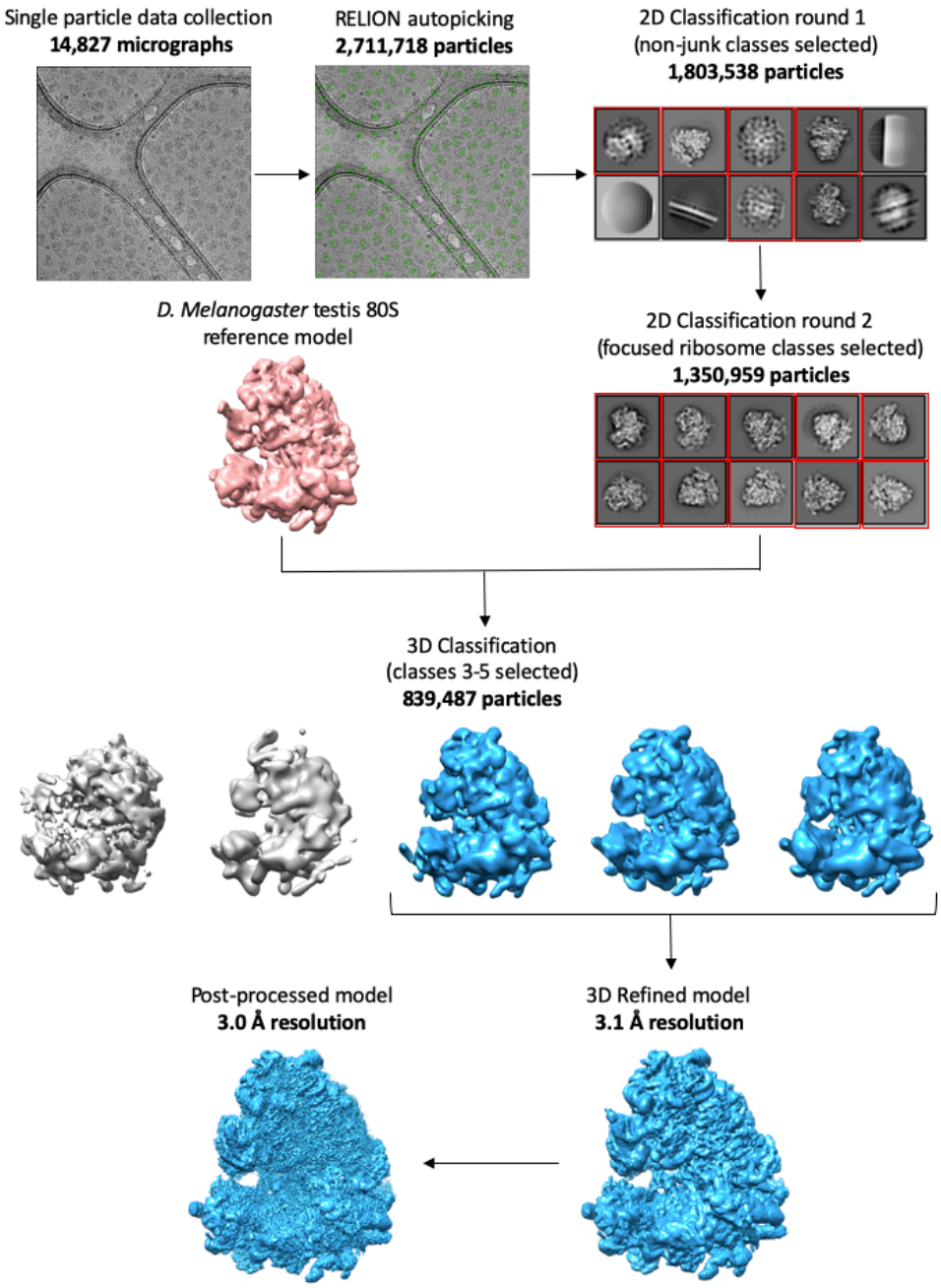

Figure 24. Schematic illustration of image processing of cryo-EM data using RELION v3.1.1 autopicked particles. From 14,872 micrographs, 2,711,718 particles were picked using the RELION autopicking software. 2 rounds of 2D classification were carried out to remove junk particles, resulting in 1,350,959 particles submitted to 3D classification. From the 5 3D classes generated, the 3 best were selected, consisting of 839,487 particles. 3D refinement of these particles resulted in a 3.1 Å initial resolution average. Post-processing resulted in a 3.0 Å final resolution. Representative 2D classes selected and taken forward are highlighted with red boxes, 3D classes selected and taken forward are coloured in blue. Only the full ribosome 3D class averages generated were selected, as determined by visual inspection, to ensure the highest resolution post processed average was produced.
Figure made with UCSF Chimera.

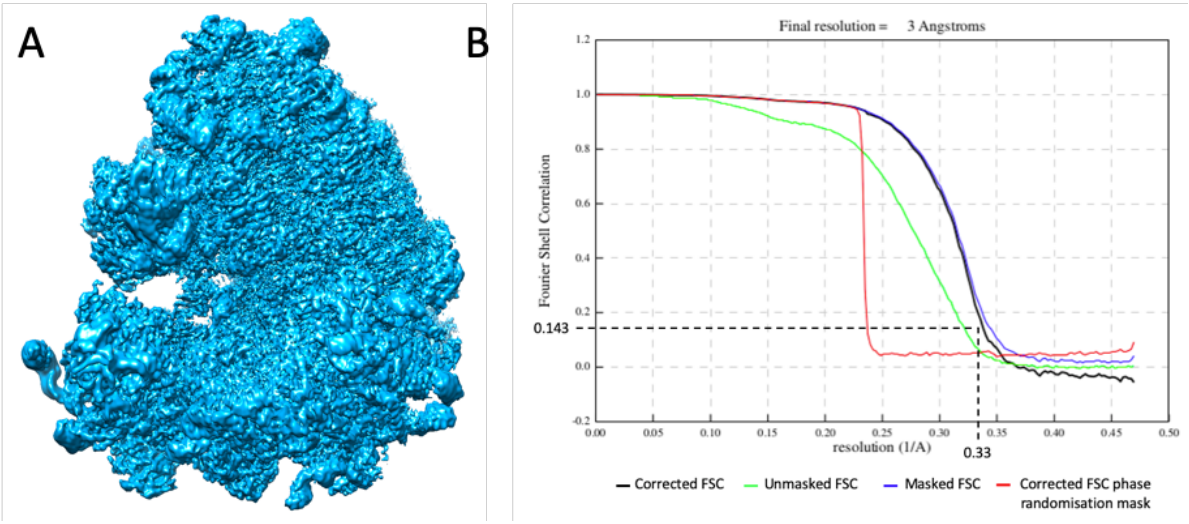

Figure 25. Head 80S post-processing average of the RELION picked particles and Fourier Shell Correlation (FSC) curve plot. (A) The *D. melanogaster* head 80S post-processed 3D average processed from 839,487 particles at a resolution of 3.0 Å. (B) Resolution plot of the average for the whole particle population. The mostly overlapping corrected FSC (black line) and masked FSC (blue line) indicates there is only a small amount of interference of noise in the final post-processed particle population average. The decrease in the corrected FSC phase randomisation mask (red line) from 1 to close to 0 indicates little randomised phase data, indicating the resolution is produced from only 80S particles (not from noise). Presence of the unmasked FSC (green line) is as expected between the corrected FSC phase randomisation mask and masked FSC values, and this compares whole unmasked volumes. The resolution of the average is calculated by taking the reciprocal of the resolution at an FSC value of 0.143, the fixed FSC value threshold at which a resolution value is comparable to X-ray crystallography (Scheres and Chen, 2012). As shown by the black dashed line, at 0.143 FSC the reciprocal resolution is 0.33, thus, 1/0.33 = 3.0 Å resolution.

Figure (A) made with UCSF Chimera.

4.3 Cryo-EM image processing of crYOLO autopicked particles results in a 3.0 Å final resolution

Due to the large number of particles autopicked by RELION, image processing of this dataset, in particular 3D refinement, took a large amount of time to complete (8 weeks). Therefore, crYOLO, a more selective particle picking software, which employs machine learning, was tested to identify if image processing jobs would process faster. I also considered that this could possibly result in a higher final resolution, compared to the RELION picked dataset, due to better selection of ribosome particles and therefore exclusion of 'junk' particles. crYOLO picking software picked on average 50 particles/micrograph, compared to 183 particles/micrograph by RELION autopicking. Particle picking in crYOLO was indeed more selective and accurate, as, unlike RELION, crYOLO did not misidentify carbon edges as particles (Figure 26). This reduced the number of particles selected (735,663 particles, 1,976,055 less than RELION) and processing of 2D classifications as carbon edges and significantly fewer 'junk' particles needed to be removed from subsequent rounds of 2D classification (Figure 27). Using the same workflow as the RELION picked particles (Figure 24), 2 rounds of 2D classification were performed to remove non-ribosome ('junk') particles, resulting in ~610,000 particles. These particles were then 3D classified into 5 classes, resulting in 4 classes containing ribosome particles (~540,000 particles), which were then refined using the *D. melanogaster* testis 80S average (Hopes et al., 2021), filtered to 375 Å to reduce reference bias.

Due to this more selective particle picking, image processing of the crYOLO picked particles was significantly faster than the RELION picked particles. Within 2 weeks of crYOLO particle picking, a post-processed model of 3.0 Å was generated (Figure 27, Figure 28). The resulting model is the same resolution achieved as the RELION autopicked model which took ~3 months to process. However, Fourier shell correlation (FSC) of the phase-randomised averages (red line, Figure 28) took a slightly higher value above zero in comparison to the RELION model (Figure 25). FSC curves might not reach zero for a number of reasons, including overfitting, incorrect orientation determination or issues with masking. In this case, since the FSC curve is close to zero (~0.05), the reason for this is likely masking; therefore, a softer mask may be required for post-processing.

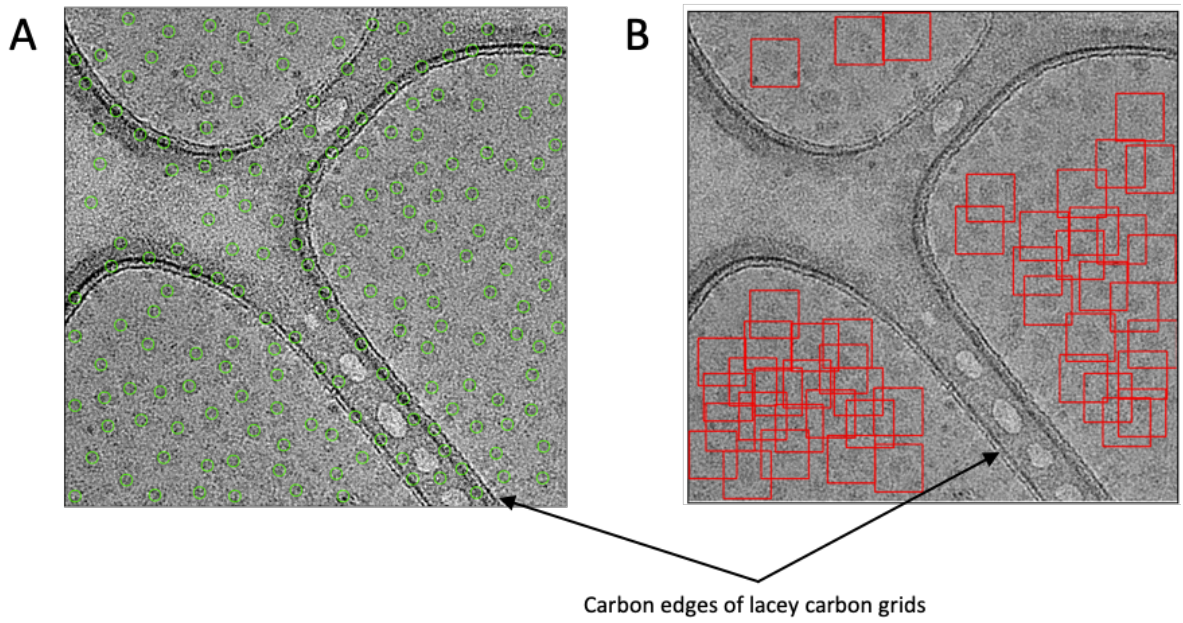

Figure 26. Comparison of RELION and crYOLO particle picking of the same micrograph. (A) RELION autopicking picked on average 183 particles/micrograph, each picked particle is represented by a green circle. RELION autopicking identifies carbon edges of the lacey carbon grids as particles for image processing. (B) crYOLO picking software picked on average 50 particles/micrograph, each picked particle is represented by a red square. crYOLO does not identify carbon edges as particles to be image processed.

Figures made with (A) RELION and (B) crYOLO.

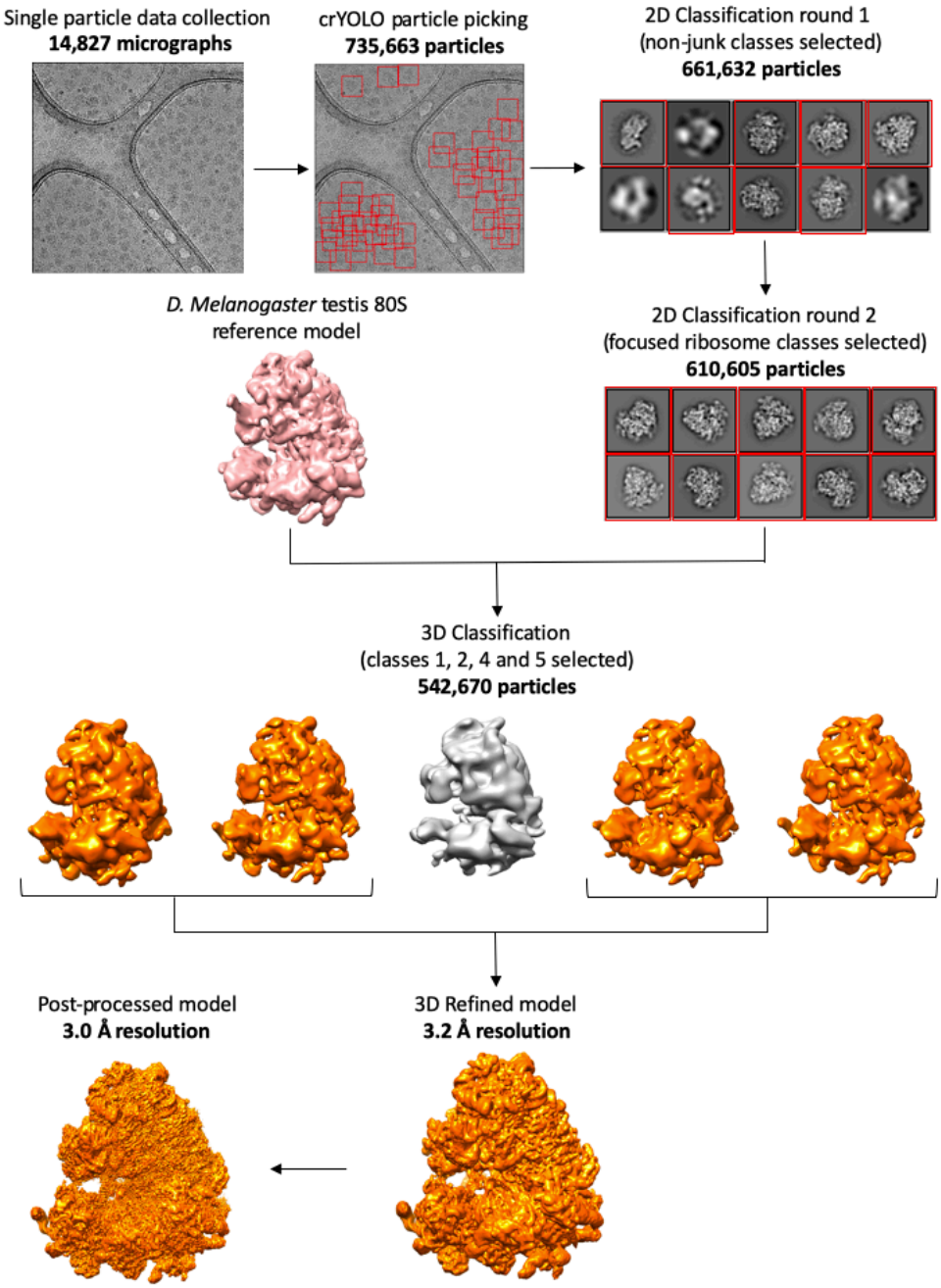

Figure 27. Schematic illustration of image processing of cryo-EM data using crYOLO picked particles. From 14,872 micrographs, 735,663 particles were picked using the RELION autopicking software. 2 rounds of 2D classification were carried out to remove junk particles, resulting in 610,605 particles submitted to 3D classification. From the 5 3D classes generated, the 4 best were selected, consisting of 542,670 particles. 3D refinement of these particles resulted in a 3.2 Å initial resolution average. Post-processing resulted in a 3.0 Å final resolution. Representative 2D classes selected and taken forward are highlighted with red boxes, 3D averages selected and taken forward are coloured in orange. Only the full ribosome 3D class averages generated, as determined by visual inspection, were selected to ensure the highest resolution post processed average was produced.

Figure made with UCSF Chimera, crYOLO and RELION outputs.

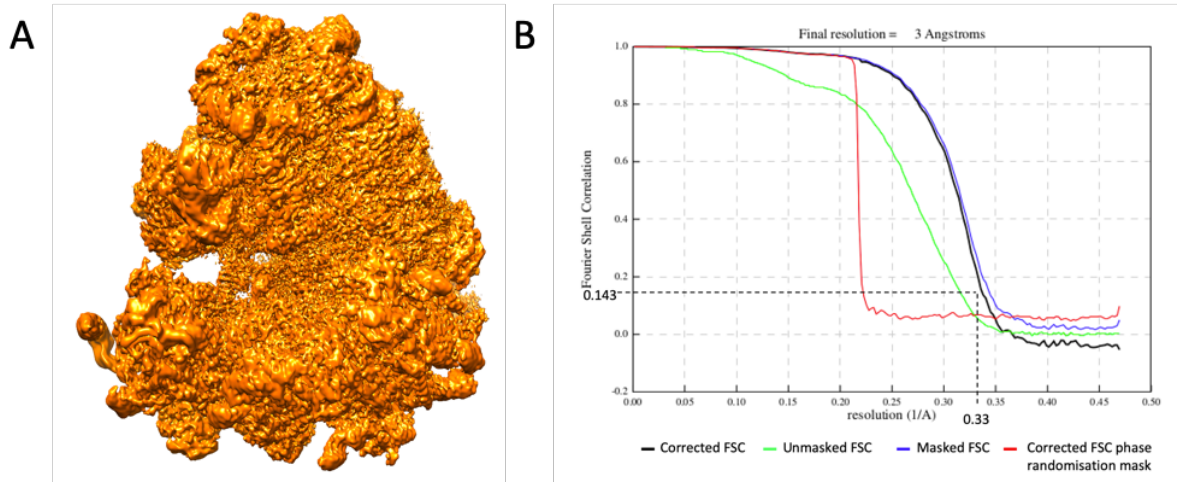

Figure 28. Head 80S post-processing average of the crYOLO picked particles and FSC curve plots. (A) The *D. melanogaster* head 80S post-processed 3D average processed from 542,670 particles at a resolution of 3.0 Å. (B) Resolution plot of the average for the whole particle population. Explanation to interpretation of the different curves is provided in the legend of Figure 25.

Figure (A) made with UCSF Chimera.

4.4 RELION and crYOLO 3D averages are identical

RELION and crYOLO achieved the same resolution. Therefore, to determine if the structures provided comparable results, the averages were overlaid. However, no obvious differences were detected in the structural densities between the two models (Figure 29). Since there were no significant differences RELION and crYOLO structures, and crYOLO generated a model in a fraction of the time, the crYOLO average was used subsequently for atomic modelling.

4.5 Global 80S ribosome atomic modelling finds no additional RpS11 densities

Due to the significant enrichment of RpS11 in *D. melanogaster* head 80S monosomes and polysomes as detected by TMT-MS (Hopes et al., 2021), I hypothesised that extra RpS11 densities would be detected by cryo-EM. Fitting of the *D. melanogaster* ovary 80S monosome and testis 80S polysome atomic models revealed an area of density in the 60S subunit that was not accounted for by these atomic model structures (Figures 30 and 31). Therefore, I suspected that this unoccupied region could potentially correspond to extra RpS11 densities. This was further investigated by fitting the *D. melanogaster* embryo 80S atomic model (Anger et al., 2013) into the head 80S monosome average, as this was the atomic model on which the testis 80S polysome and ovary 80S structures were calculated. However, fitting of this atomic model explained all ribosome densities in the average and the previously unoccupied region was now accounted for by the atomic model (Figure 32). This density was confirmed to be RpLP0, a lateral stalk subunit, which was present in the embryonic extract 80S atomic model but not included in the ovary 80S monosome and testis 80S polysome atomic models. Therefore, after this investigation, I found no additional densities were detected in the head 80S monosome average that could account for an additional copy of RpS11.

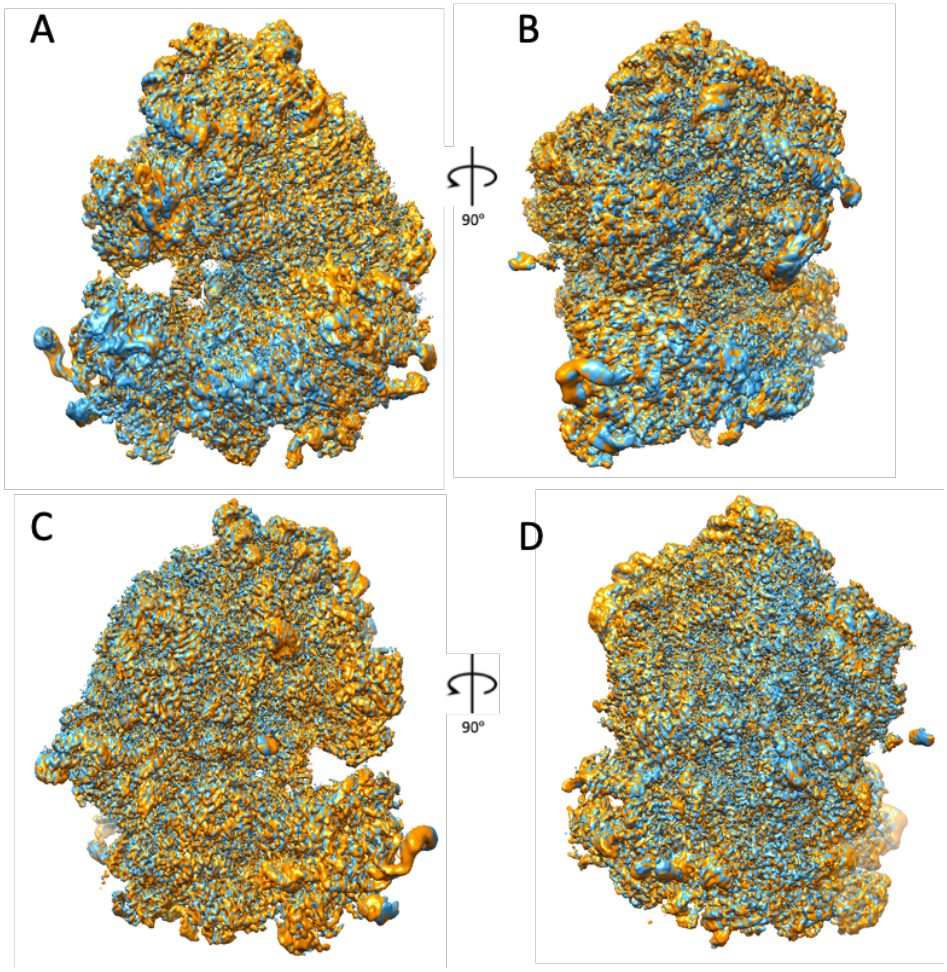

Figure 29. Superimposition of RELION and crYOLO cryo-EM *D. melanogaster* head 80S 3D averages reveals no apparent differences. Each view represents a 90° rotation about the vertical axis of the 80S ribosome. (A) Left side view (B) front view (C) right side view (D) back view. RELION average is shown in blue and crYOLO in orange.

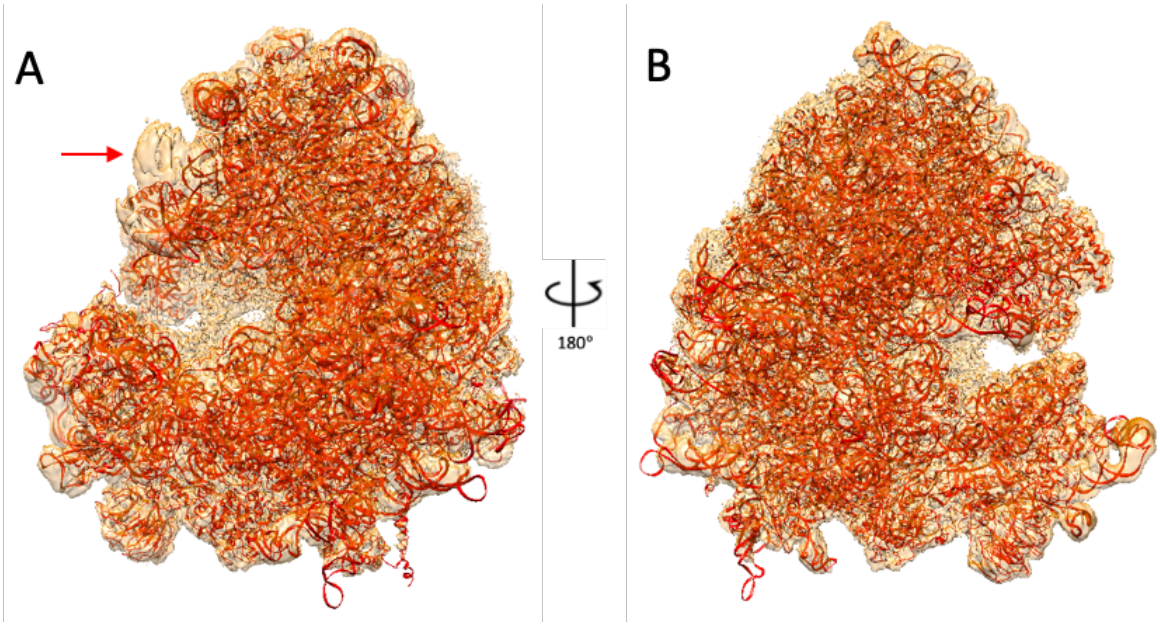

Figure 30. *D. melanogaster* ovary 80S structure (Hopes et al., 2021) fitted onto the crYOLO cryo-EM *D. melanogaster* head 80S 3D average. *D. melanogaster* ovary 80S structure (red) and crYOLO 3D average (pale orange). (A) Left side view, red arrow indicating unaccounted density, not occupied by the atomic model. Each view represents a 180° rotation about the vertical axis of the 80S ribosome. (B) Right side view.

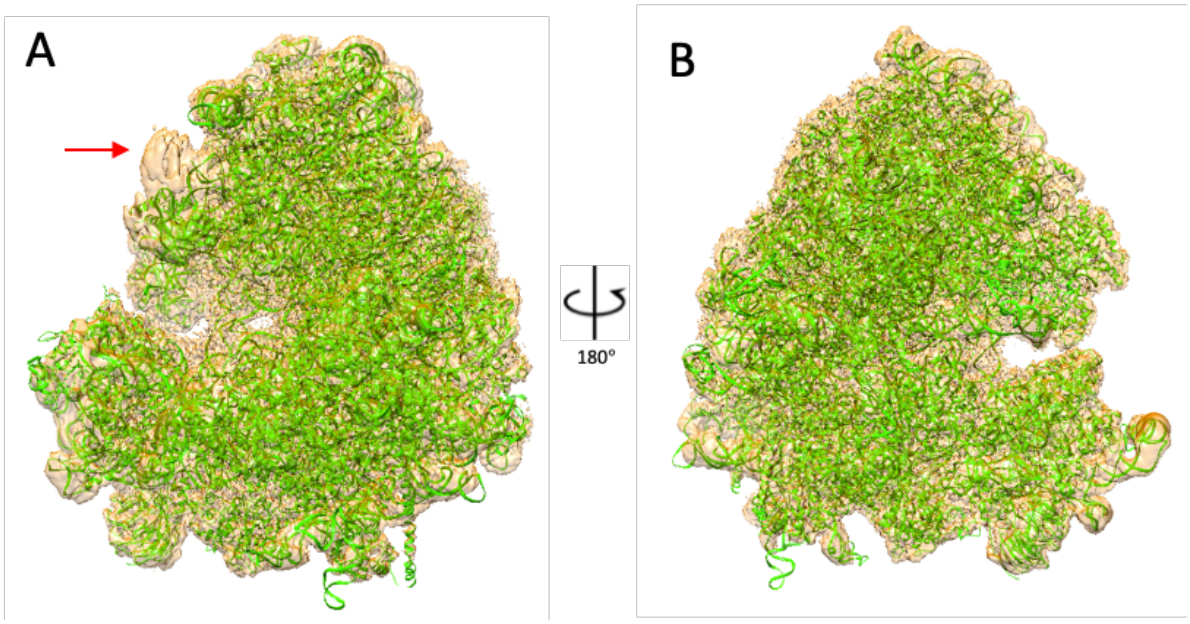

Figure 31. *D. melanogaster* testis 80S polysome structure (Hopes et al., 2021) fitted onto the crYOLO cryo-EM *D. melanogaster* head 80S monosome 3D average. *D. melanogaster* testis 80S structure (green) and crYOLO 3D average (pale orange). Each view represents a 180° rotation about the vertical axis of the 80S ribosome. (A) Left side view, red arrow indicating unaccounted density, not occupied by the atomic model. (B) Right side view. Testis 80S polysome structure is shown in green and crYOLO 3D average in pale orange.

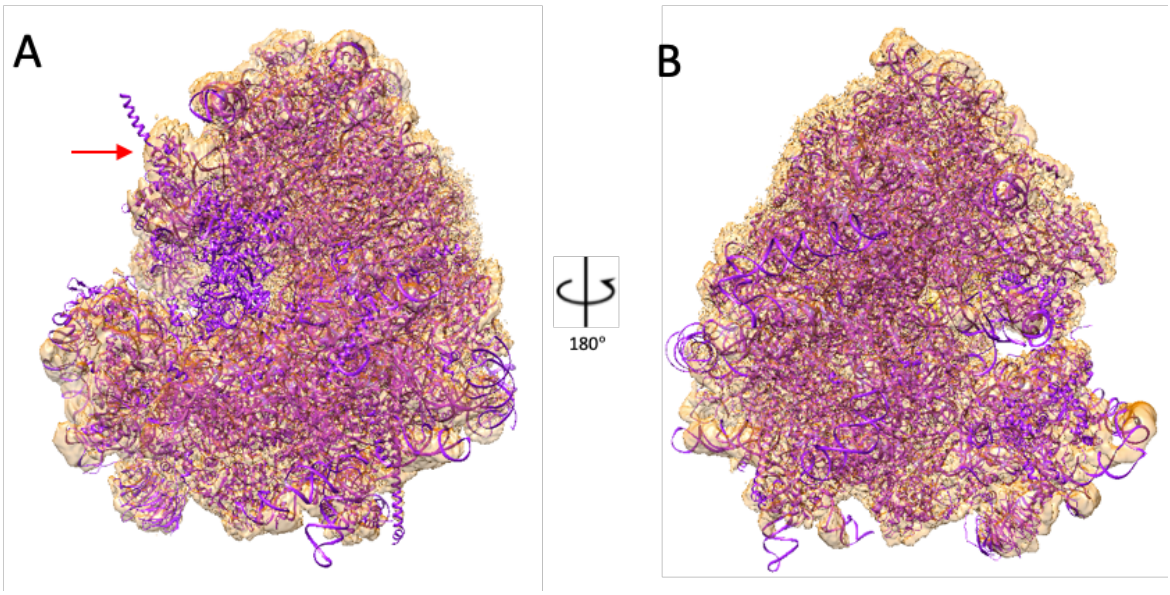

Figure 32. *D. melanogaster* embryonic extract 80S monosome (Anger et al., 2013) fitted onto the crYOLO cryo-EM *D. melanogaster* head 80S monosome 3D average. *D. melanogaster* embryonic extract 80S structure (purple) and crYOLO 3D average (pale orange). Each view represents a 180° rotation about the vertical axis of the 80S ribosome. (A) Left side view, red arrow indicating density accounted for by RpLP0. (B) Right side view.

4.6 Confirmation that the head RpS11 atomic model is identical to other tissues

Since no extra RpS11 densities were detected in the 80S average, the canonical RpS11 occupancy was investigated. I sought to determine if the head 80S monosome RpS11 was in an altered conformation or structural location in comparison to other *D. melanogaster* ribosomes. The atomic model of the ovary 80S monosome RpS11 seemed to be majorly accounted for and fitted tightly within the head 80S monosome electron density average (Figure 33).

To contextualise the fit, location and occupancy of RpS11 in the head 80S monosome average, the fit of RpS11 within averages from ribosomes from different *D. melanogaster* tissues was analysed (Figure 34). The RpS11 atomic models from the testis 80S monosome, testis 80S polysome, ovary 80S monosome, embryo 80S monosome and embryo 80S foot-printed polysome, fitted well within their respective averages. Moreover, all fits were nearly identical. This suggests that there are no structural consequences of the significant RpS11 enrichment detected by TMT-MS in head 80S ribosomes, in terms of position, structure or stoichiometry of RpS11, when analysed by cryo-EM.

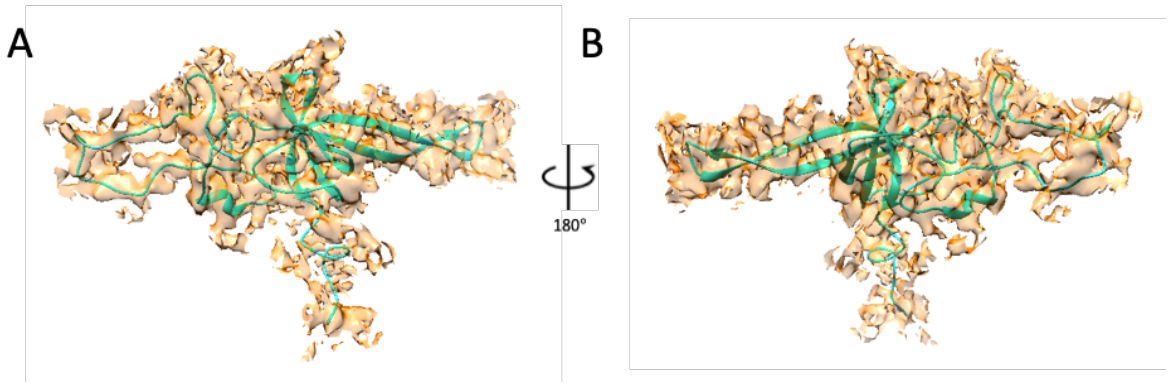

Figure 33. The atomic model fit of the *D. melanogaster* ovary 80S RpS11 onto the crYOLO *D. melanogaster* head 80S monosome 3D average. Each view represents a 180° rotation about the vertical axis of the 80S ribosome. (A) Front view (B) back view. *D. melanogaster* ovary 80S RpS11 atomic model is shown in turquoise and *D. melanogaster* head 80S monosome 3D average in pale orange.

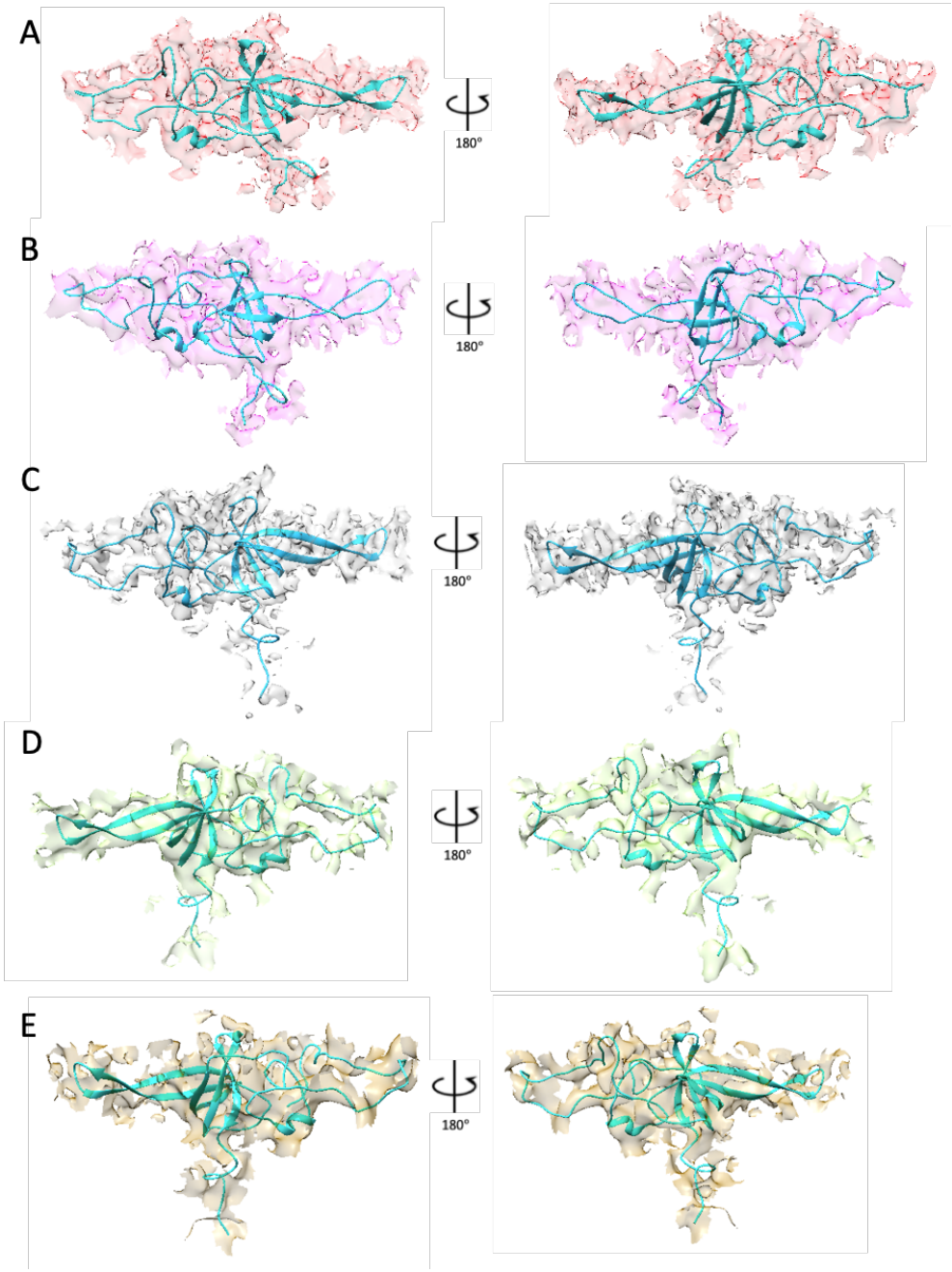

Figure 34. The atomic model fit of RpS11 in various *D. melanogaster* tissue ribosomes cryo-EM averages. (A) Testis 80S monosome average (light red), testis 80S monosome RpS11 atomic structure (turquoise). (B) Testis 80S polysome average (magenta), testis 80S polysome RpS11 atomic structure (turquoise). (C) Ovary 80S monosome (light grey), ovary 80S monosome RpS11 atomic structure (turquoise). (D) Embryo 80S monosome (light green), ovary 80S monosome RpS11 atomic structure (turquoise). (E) Embryo 80S foot-printed polysome (light brown), ovary 80S monosome RpS11 atomic structure (turquoise). Each view represents a 180° rotation about the vertical axis of the 80S ribosome. Testis 80S monosome and polysome, and ovary 80S monosome and polysome atomic models and averages from Hopes et al, (2021). Embryo 80S monosome and embryo foot-printed 80S polysome by Amy Turner.

4.7 Discussion

The second aim of this project was to dissect the structural effect of the now confirmed RpS11 enrichment in head tissue ribosomesas detected by TMT-MS. This was hoped to indicate a structural mechanism by which RpS11 head enriched ribosomes could target specific mRNAs for translational regulation.

4.7.1 Head 80S monosome structural analysis

Cryo-EM image analysis was carried on the head 80S monosome dataset particles. My analysis started with a comparison of RELION and crYOLO particle picking software, focused on image processing time and particle picking accuracy, to develop the ideal pipeline for 80S image analysis. crYOLO picked far fewer junk particles, but a similar number of ribosome particles; as a consequence, it was more accurate than RELION, resulting in much faster processing. However, both crYOLO and RELION datasets resulted in visually identical averages at the same resolution (3.0 Å). Due to faster processing, the time the crYOLO average was taken forward for structural analysis and used for further analysis.

4.7.2 Determining structural consequences of RpS11 enrichment by atomic modelling

A recent study has established structural evidence of differential RP stoichiometry resulting in additional copies of RPs residing in noncanonical positions. In *Chaetomium thermophilum*, the 60S RpL41 was detected in the periphery of the 60S as well as the canonical location of the interface between the 60S and 40 subunits. Whereas in *S. cerevisiae*, only one copy of RPL41 was located in the canonical position (Kišonaitė et al., 2022). Therefore, due to the significant enrichment of RpS11 in *D. melanogaster* head 80S monosomes and polysomes compared to other tissue ribosomes (Hopes et al., 2021), I expected to detect additional locations of RpS11 in head 80S structures or perhaps altered structural location of the canonical RpS11, compared to other available *D. melanogaster* tissue ribosome atomic models (embryonic extract 80S monosome (Anger et al., 2013), testis polysome and ovary 80S monosome (Hopes et al., 2021). However, global atomic modelling of the available *D. melanogaster* tissue ribosome structures fitted extremely well to the head 80S monosome average. No additional densities were detected, after the RpLP0 density was accounted for in the ovary 80S monosome and testis polysome atomic models (Figures 30 – 32). Due to the relatively large size of RpS11 (153 residues), I expected that if additional copies of RpS11 were present, they would be easily detected whether they were located internally or on the periphery of the ribosome. However, this was not the case, which could possibly indicate that a truncated version of RpS1 was incorporated into the ribosome, which could not be ruled out by TMT-MS peptide fragment analysis but seemed unlikely (Section 3.2). Therefore, it is possible that no additional copies of RpS11 are present in a consistent

location in the head 80S ribosomes, detectable at any contour level. This was surprising as the head ribosome sample analysed by TMT-MS was derived from sucrose purified ribosomes, implying that the significant enrichment of RpS11 must be due to additional copies of RpS11 interacting with the ribosome. Therefore, I investigated the fit of the canonical RpS11 within the head 80S monosome average to determine if there were any differences in structure or location. Atomic modelling of the ovary 80S monosome RpS11 structure fitted within the head 80S monosome electron density tightly and all densities were accounted for, implying there was no difference in canonical RpS11 occupancy (Figure 33). Furthermore, the atomic model fit of the ovary 80S monosome canonical RpS11 in the head 80S monosome average was virtually identical to all other available *D. melanogaster* tissue ribosomes (Figure 34). Together, this structural analysis of *D. melanogaster* head 80S monosomes found no consequences of the reported significant enrichment of RpS11 in head tissue in comparison to other tissues, as detected by TMT-MS analysis (Hopes et al., 2021). A possible explanation for no detection of any additional RpS11 densities could be that additional RpS11 proteins may have been incorporated into the ribosome in place of another RP that is not essential for general translation or else is bound very weakly to the ribosome and is lost in the process of cryo-EM sample preparation. If this was true, it could likely be one of the several RPs seen to be significantly enriched in the testis and ovary 80S monosomes in comparison to the head 80S monosomes (Figure 7B and C). To investigate this, the head 80S monosome atomic model coordinates could be further refined by combining automated atomic model refinement with visual inspection (Afonine et al., 2018; Emsley et al., 2010). Following this, atomic models would be generated for each ribosome sample, from which more accurate structural analysis of the atomic models could be carried out to identify any additional RpS11 structures within the head 80S monosome.

5 tRNA occupancy of *D. melanogaster* ribosomes

5.1 Introduction

The third aim of this project was to determine the translational profile of monosomes across different *D. melanogaster* tissues. Historically monosomes of have been assumed to be far less translationally active than polysomes as translation occurs more efficiently when many ribosomes simultaneously translate 1 mRNA. Monosomes, however are thought to consist of 2 types of 80S ribosome: i) monosomes are formed in the absence of mRNA and therefore not actively translating, termed 'vacant couples' (Noll et al., 1973), and ii) actively translating 80 ribosomes associated with low abundance and highly regulated mRNA transcripts (Heyer and Moore, 2016). However, the relative proportion of these two groups has not been established.

5.2 The head 80S monosome average contains all classical tRNA densities

When inspecting the head 80S monosome global average, I observed strong tRNA densities within the mRNA channel, indicative of a substantial proportion of head 80S monosomes to be engaged in active translation. A detailed analysis of the head 80S monosome average found that multiple tRNA densities were present, assessed by fitting atomic models of the classical tRNAs (A/A, P/P and E/E) (Figure 35). This showed densities corresponding to the A/A and P/P tRNAs, in addition to faint densities for the E/E tRNA. According to the literature, during peptide bond formation ribosomes usually only contain two tRNAs which move from the A/A and P/P sites into the P/P and E/E sites via the intermediate A/P and E/P states (Uemura et al., 2010; Schuller and Green, 2018). Therefore, it seems likely that head 80S monosome was an average of the elongation translational stages, likely including the intermediate tRNAs A/P and E/P and possibly elongation factors, in addition to the classical tRNAs. For this reason, I decided to ascertain if the head 80S monosomes were trapped in different translational states. Together, the presence of the intermediate tRNA and multiple translational states would confirm the head 80S monosomes are actively translating. I aimed to calculate the proportion of the head 80S monosomes engaged in active translation compared to the tRNA vacant monosomes. In addition, I sought to understand if this level of tRNA occupancy is exclusive to the head tissue and if tissue specific differences exist.

5.3 Determining and quantifying translational states of the head 80 monosome dataset

The methods by which tRNA occupation and the translational states present were determined and assessed was first validated in the head 80S monosome dataset and applied to the remaining *D. melanogaster* tissue ribosome datasets.

To resolve the individual translational states of the head 80S monosome, 'focused classification' was used to classify monosomes into classes according to their tRNA occupation or vacancy. The focused classification uses a mask to focus on a region of localised 3D variance in a further classification job on RELION (Penczek et al., 2006). In this case the region of variance focused on was the mRNA channel. The head 80S monosome dataset particles were binned 5 times to expedite the image processing steps; as the final resolution was 3.0 Å (corresponding to a maximum resolution of 10.65 Å), the image processing aimed only at determining the presence or absence of tRNAs which can be assessed at lower resolutions.

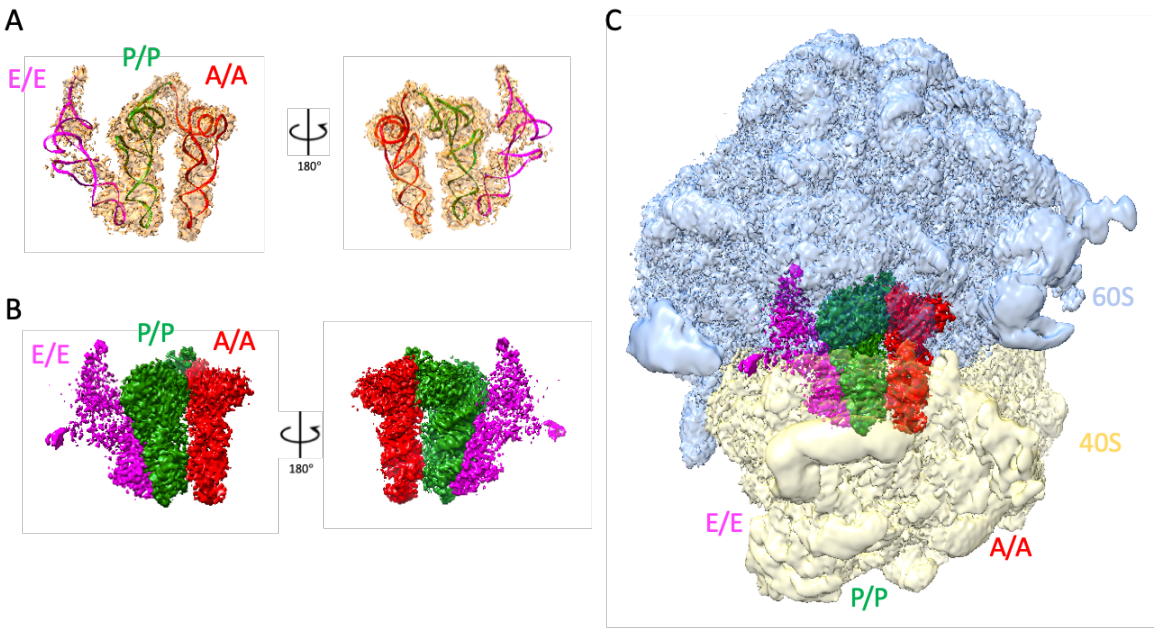

Figure 35. The atomic model fit of the classical tRNAs within the crYOLO *D. melanogaster* head 80S monosome electron density average. (A) Atomic model fit of the classical tRNAs within the average of head 80S monosomes. (B and C) Coloured EM densities based on the fits of the classical tRNAs, on their own (B) or together with the whole average (C). A/A site tRNA is shown in red, P/P tRNA site in green and E/E in pink. In C, the large (blue) and small (yellow) subunits, are shown at 70% transparency.

5.3.1 Justifying tRNA occupation assessment at the mean + 1σ contour level

To accurately interpret the tRNA occupation or vacancy of the resultant significant focused classification class averages, the contour level of each average must be carefully chosen. I sought an objective contour level that was appropriate to assess tRNA occupation and the strength of tRNA density detection (strong, partial or faint). I stipulated that this level would show the largest amount of densities around the mRNA channel without any background noise or the loss of structural information.

The atomic model of the testis 80S polysome was fitted to each significant focused classification class average and contours corresponding to multiples of the standard deviation from the mean (mean + xσ) were calculated for each class. The averages were assessed by visual inspection for background noise and the atomic model fit at the different contour levels (Figure 36). Consistently across all the significant head 80S monosome focused classification classes, the mean + 1σ level was found to be the most appropriate level. In all averages at the mean contour level, notable background noise was observed. At the mean + 2σ and mean + 3σ levels there was a loss of densities around the atomic models compared to the mean + 1σ level, as evidenced by the electron density averages no longer covering the atomic model. Therefore, the mean + 1σ level was selected to analyse tRNA occupancy of the head 80S monosomes and all other *D. melanogaster* tissue ribosome datasets.

5.3.2 Validation of the focused classification

To validate the focused classification method to resolve and assess tRNA densities within the mRNA channel an unmasked 10-class 3D classification without alignment was carried out in parallel for comparative analysis. Both classifications were assessed on the number of resultant unique significant classes. Significant classes were defined as classes containing >1% total dataset particles and >200 particles. The resolution of classes below this threshold were considered too poor to define tRNA occupation. The focused classification for the head 80S dataset produced 6 significant classes, showing 3 unique tRNA conformations and 1 tRNA vacant class, accounting for 99.88% of the head 80S monosome particles (Figure 37). In comparison, the unmasked classification produced 4 significant classes with only 2 unique tRNA conformations and no tRNA vacant classes, accounting for 98.09% of particles (Supplemental figure 5). I therefore concluded that the focused classification was more accurate in resolving individual tRNA occupancy and vacancy conformations. Accordingly, the focused classification method was used to assess tRNA occupancy of the head 80S monosome and other *D. melanogaster* tissue ribosome datasets. It should be noted that a dataset specific mRNA channel mask was generated for each dataset focused classification.

5.4 98% of head 80S monosomes contain tRNAs

Having determined the focused classification workflow to classify the different tRNA occupation/vacancy within a ribosomal dataset and validated the contour level at which to assess this, the significant head 80S monosome classes were analysed (Figure 37). The percentage of particles making up each significant class was calculated, and the tRNA densities I confirmed and detected for this, and all other datasets were qualitatively scored by level of density detection: full (+++), partial (++) and faint (+). Once the tRNA occupation was confirmed, the translational state each significant class could represent was then assigned.

Overall, 97.59% of dataset particles formed tRNA occupied classes and 2.29% of dataset particles formed the tRNA vacant classes. 3 of the 6 classes representing 60.55% of dataset particles contained densities for both A/A and P/P tRNAs, which I determined to represent the elongation stages of peptide bond formation and pre-translocation (Figure 37A, D, E). 18.55% of dataset particles contained densities for the intermediate tRNA conformations A/P and P/E, which correspond to the hybrid state elongation stage (Figure 37B). 18.50% of dataset particles contained only densities corresponding to the P/P site tRNA, which is suggestive this represents the E/E site ejection stage (Figure 37C). However, this could also be potentially representative of the post-translocation stage after CHX treatment. Although the post-translocation stage consists of occupation the P/P and E/E site tRNAs, CHX was used in the ribosome purification protocol. CHX is an elongation inhibitor which occupies the E/E site, preventing eEF2 entry but allows for an additional round of translocation (Pestova and Hellen, 2003). Therefore, this strong P/P signal could be from a post-translocation stage monosome after CHX incorporated, where the E/E site tRNA would be ejected and no additional A/A site tRNA has been incorporated. However, this cannot be confirmed as presence of CHX cannot be seen at this low resolution.

This demonstration of tRNA occupation in 5 out of 6 significant classes and the identification of multiple translational states, strongly suggests that the majority head 80S monosomes are actively translating.

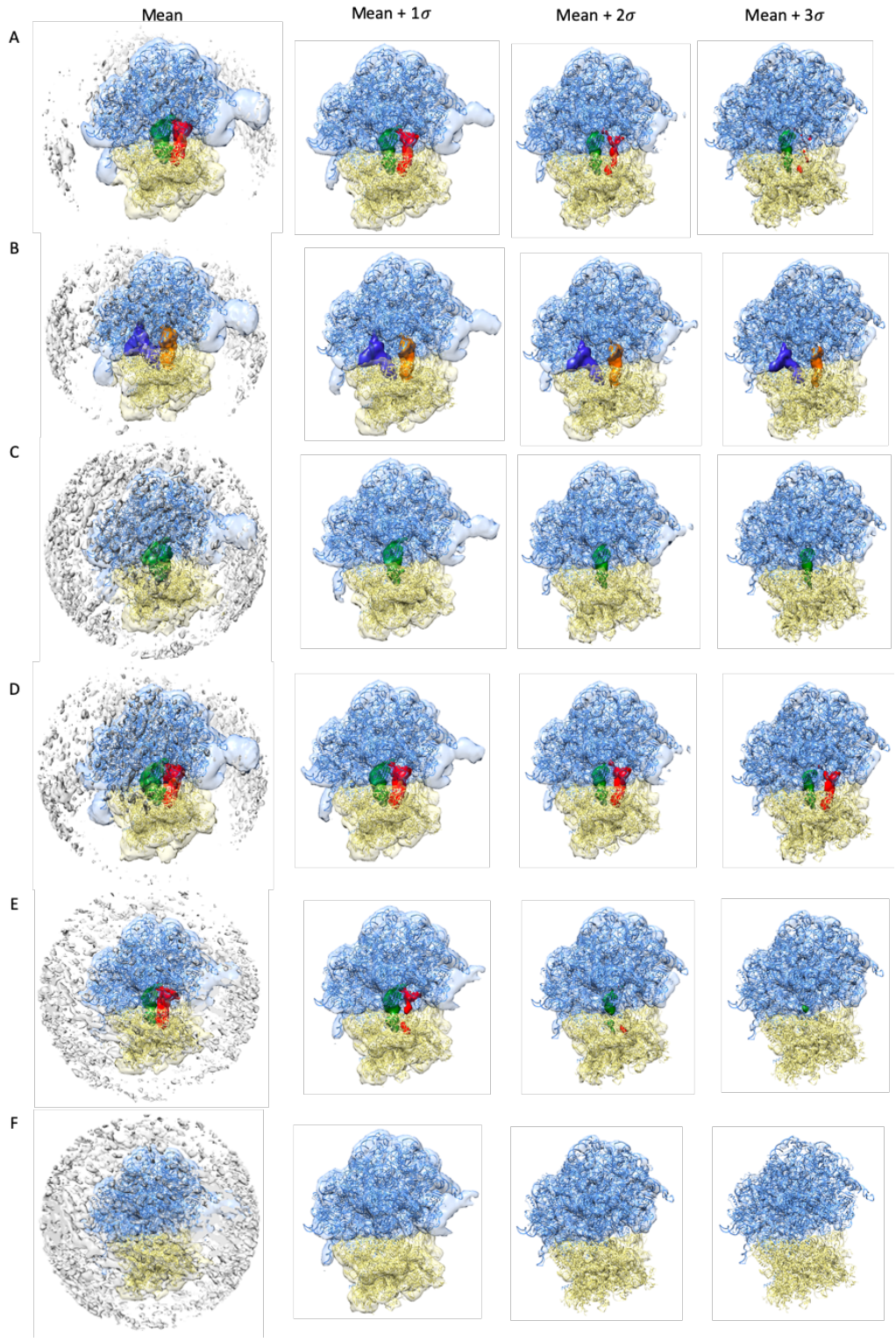

Figure 36. The 6 significant 3D classes of the head 80S dataset (610,605 particles) focused classification, presented at the mean, mean + 1σ, mean + 2σ and mean + 3σ contour levels. Significance was defined as focused classes consisting of >1% dataset particles and >300 particles. A to F, significant head 80S monosome classes, fitted with the testis 80S polysome structure and ordered by abundance (A, most abundant). 60S (light blue), 40S (yellow), A/A tRNA (red), P/P tRNA (green), A/P tRNA (orange), P/E tRNA (blue).

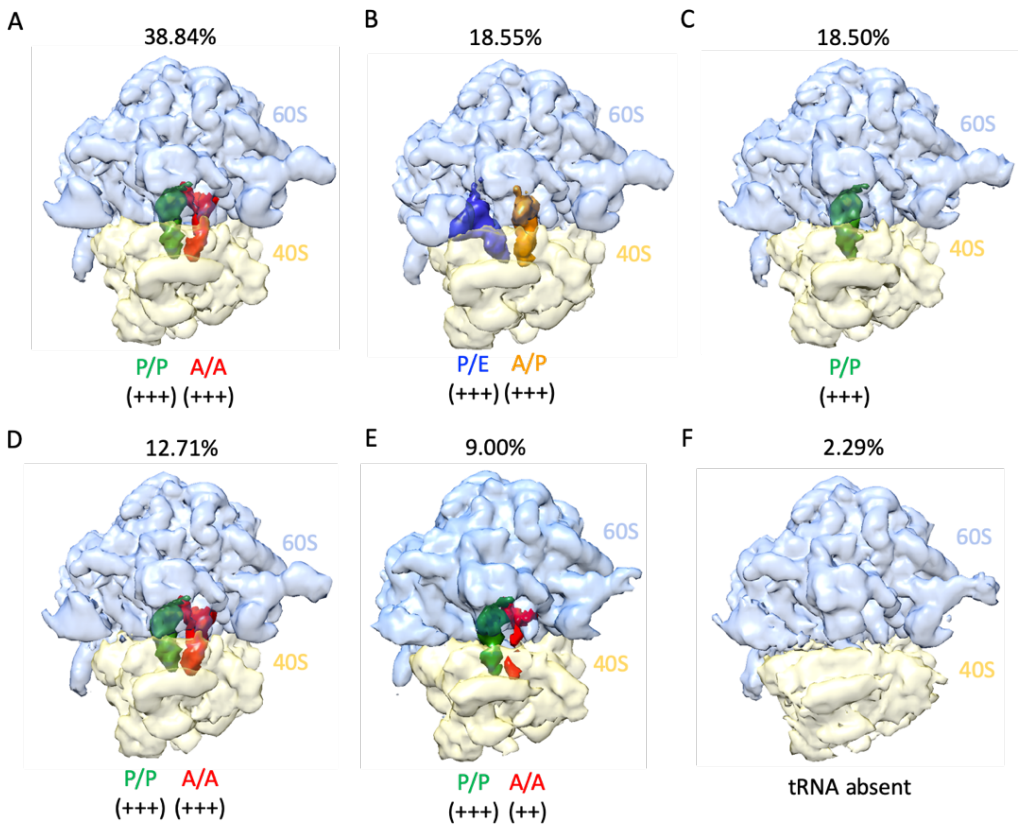

Figure 37. Significant classes resulting from focused classification of the head 80S monosome dataset (610,605 particles). (A) 38.84% (237,142) dataset particles, containing strong A/A tRNA (red) and P/P tRNA (green) densities. (B) 18.55% (113,271) dataset particles containing strong A/P tRNA (orange) and P/E tRNA (blue) densities. (C) 18.50% (112,936) dataset particles, containing strong P/P tRNA (green) densities. (D) 12.71% (77,605) dataset particles, containing strong A/A tRNA (red) and P/P tRNA (green) densities. (E) 9.00% (54,932) dataset particles, containing partial A/A tRNA (red) densities and strong P/P (green) tRNA densities. (F) 2.29% (13,962) dataset particles, tRNA vacant. 60S is light blue and 40S is yellow. mRNA channel densities were qualitatively scored on a scale of full (+++), partial (++) and faint (+).

5.5 91% of embryo 80S monosomes exhibit tRNA occupancy

The structure of 80S monosomes from *D. melanogaster* embryos has previously been resolved to 6.0 Å and was determined to contain an E/E site tRNA (Anger et al., 2013). Therefore, I hypothesised that the focused classification of the embryo 80S monosome dataset (11,446 particles) would reveal high levels of tRNA occupancy similar to the head 80S monosomes. Focused classification resulted in 97.16% of dataset particles forming significant classes. 91.22% of dataset particles formed 3 tRNA occupied classes and 5.94% formed 1 tRNA absent class. 83.06% of dataset particles contained partial P/P and E/E tRNA densities indicative of the post-translocation elongation stage (Figure 38A). Due to the small percentage of particles in the dataset, the remaining two tRNA occupied classes (representing 5.75 and 2.41% of dataset particles, respectively) were resolution limited meaning that detailed assessment of the specific sites these tRNAs occupied and the translational states they represent could not be determined (Figure 38C, D). However, they clearly contained densities at the mRNA channel, and therefore were considered tRNA-containing classes. Similarly, the remaining class (representing 5.94% of dataset particles) was resolution limited, preventing a detailed assessment, but deemed to be tRNA absent due to the mRNA channel appearing vacant by visual inspection (Figure 38B). Together this data implies, as with head 80S monosomes, that the majority of embryo 80S monosomes are actively translating.

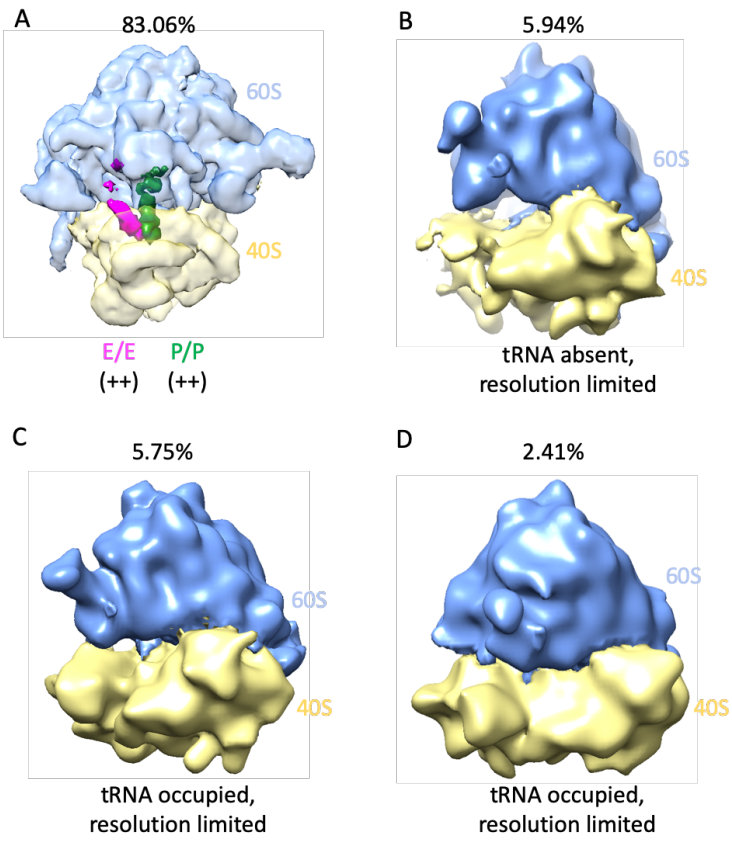

Figure 38. Significant classes resulting from focused classification of the embryo 80S monosome dataset (11,446 particles). (A) 83.06% (9,507) dataset particles, containing partial E/E tRNA (pink) and P/P tRNA (green) densities. (B) 5.94% (680) dataset particles, tRNA absent with detailed assessment limited by poor resolution. (C) 5.75% (658) dataset particles, tRNA occupied with detailed assessment limited by poor resolution. (D) 2.41% (276) dataset particles, tRNA occupied with detailed assessment limited by poor resolution. 60S is light blue and 40S is yellow. mRNA channel densities were qualitatively scored on a scale of full (+++), partial (++) and faint (+).

5.6 99% of embryo 80S foot-printed polysomes are tRNA occupied

The embryo 80S foot-printed polysome dataset (34,603 particles) was generated by Amy Turner. This dataset was derived from embryo polysome fractions isolated by sucrose gradient centrifugation and treated with RNase, which digested the mRNA between each 80S ribosome, producing 80S foot-printed polysomes. This dataset was selected to be analysed as a positive control. Since the dataset was collected from foot-printed polysomes, they must be in a state of active translation and therefore containing tRNA. Focused classification resulted in 4 tRNA occupied significant classes, representing 99.23% of dataset particles (Figure 39). 53.13% of dataset particles made up the most populated class of 80S polysomes, which contained densities for the hybrid tRNA site conformations, A/P and E/P, and therefore was considered to be in the hybrid state of the elongation stage of translation (Figure 39A). 43.18% of dataset particles contained densities for the P/P and E/E site tRNAs, indicative of the final elongation stage, post-translocation (Figure 39B). The least populated significant class (1.25% of dataset particles) contained densities for A/A and P/P site tRNA densities which was determined to be representative of the elongation stage states of peptide bond formation and pre-translocation (Figure 39D). The tRNA assignment of the tRNA occupied class consisting of 1.67% of dataset particles was limited by poor resolution, meaning no specific tRNA or translational state designation could be made (Figure 39C). Therefore, the detection of multiple translational states confirms as expected that the embryo 80S foot-printed polysomes are actively translating.

5.7 IFRD1 occupies 99% of testis 80S monosomes

It has been previously described that on average testis 80S ribosomes contain IFRD1 but it was not determined the percentage of them that did (Hopes et al., 2021). *D. melanogaster* IFRD1 is orthologous to rabbit IFRD2, a protein that was identified to be occupied spanning the P/P and E/E sites of inactive rabbit reticulocyte ribosomes, representing 7.6% of rabbit reticulocyte ribosomal particles and approximately 20% of translationally inactive ribosomal particles (Hopes et al., 2021; Brown et al., 2018). To determine the proportion of IFRD1 occupation in testis 80S monosomes, focused classification of the testis 80S monosome dataset (46,878 particles) was performed. This resulted in 2 significant classes, representing 98.72% of dataset particles. Both significant classes contained strong IFRD1 densities, positioned in the P/P and E/E tRNA sites. No tRNA densities were detected in either class indicating that at least 98.72% of testis 80S monosomes are translationally inactive (Figure 40). This data implies that IFRD1 is a potent inhibitor of translation of the testis 80S monosomes.

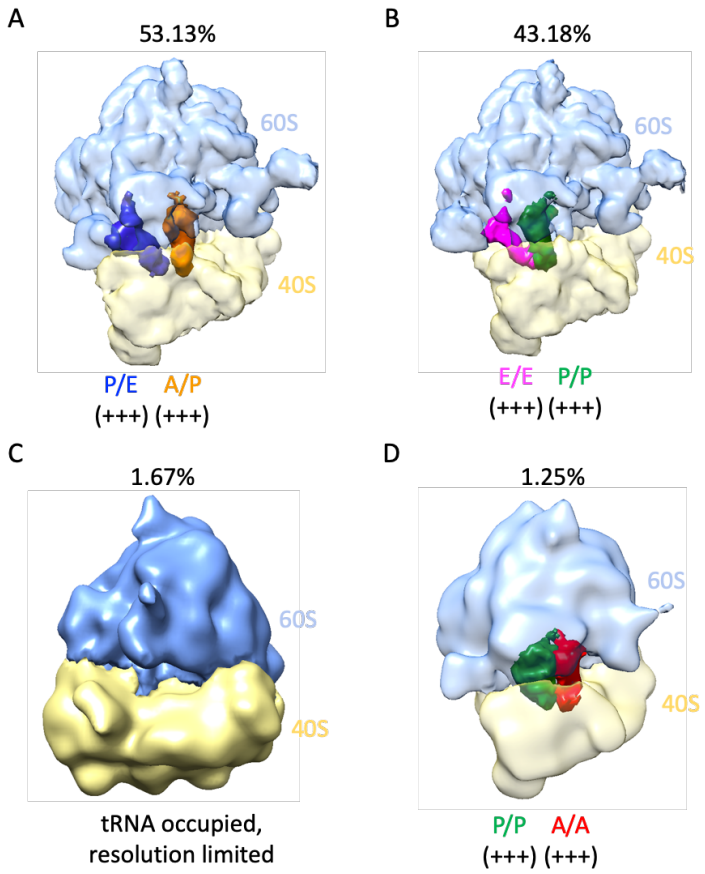

Figure 39. Significant classes resulting from focused classification of the embryo 80S foot-printed polysome dataset (34,603 particles). (A) 53.13% (18,383) dataset particles, containing strong P/E tRNA (blue) and A/P tRNA (orange) densities. (B) 43.18% (14,943) dataset particles, containing strong E/E tRNA (pink) and P/P tRNA (green) densities. (C) 1.67% (577) dataset particles occupied with detailed assessment limited by poor resolution. (D) 1.25% (434) dataset particles containing strong P/P tRNA and A/A tRNA (red) densities. 60S is light blue and 40S is yellow. mRNA channel densities were qualitatively scored on a scale of full (+++), partial (++) and faint (+).

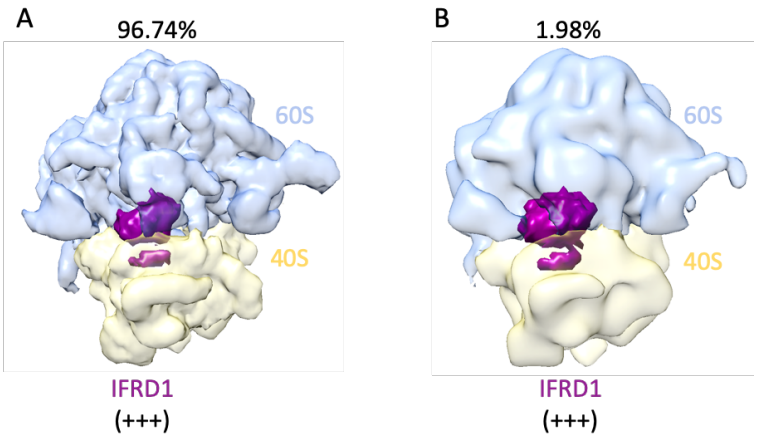

Figure 40. Significant classes resulting from focused classification of the testis 80S monosome dataset (46,878 particles). (A) 96.74% (45,351) dataset particles, containing a strong IFRD1 (purple) density in the mRNA channel. (B) 1.98% (926) dataset particles, containing a strong IFRD1 (purple) density in the mRNA. 60S is light blue and 40S is yellow. mRNA channel densities were qualitatively scored on a scale of full (+++), partial (++) and faint (+).

5.8 97% of testis polysomes are tRNA occupied

Atomic modelling of testis 80S polysomes previously determined that a tRNA occupied the P/P site, as would be expected for actively translating polysomes (Hopes et al., 2021). I was therefore interested if focused classification could detect classes with additional tRNA densities and determine the level of testis 80S polysomes engaged in translation. Focused classification of the testis 80S polysome dataset (10,392 particles) resulted in just one significant class, made up of 97.25% of the dataset particles, which was tRNA-occupied. This class consisted of a faint A/A density and full P/P density (Figure 41). Due to the presence of only one significant class, the small size of the dataset and faint density detection of the A/A tRNA, designation of the translational stage is difficult to assign. A potential explanation is that this class represents a combination of the elongation stages peptide bond formation and pre-translocation and E/E site ejection or possibly CHX incorporated post-translocation. This CHX incorporated post-translocation stage, as discussed in the head 80S monosome tRNA occupation analysis above, would explain the very strong P/P tRNA site occupation. This could also indicate that the limited number of dataset particles were being stretched too far by being forced into a 10 class focus classification, therefore I decided to carry out a 5 class focus classification to compare resultant classes. However, this resulted in virtually the same result of 1 significant focused class consisting of 97.06% of all particles (10,087 particles) with a faint A/A density and full P/P density (supplemental figure 6).

In any case, it can be confidently concluded that the testis 80S polysomes are actively translating and not trapped in one translational conformation. Despite not clearly showing multiple elongation states across several significant classes, polysomes are known to be actively translating and there are clearly tRNAs present in the mRNA channel.

5.9 97% of ovary 80S monosomes are vacant couples

Finally, I analysed the ovary 80S monosome particle set. Previous analysis of the final cryo-EM average did not detect any tRNAs or additional densities around the mRNA channel (Hopes et al., 2021). However, I was unsure if this was true all ovary 80S monosomes. Therefore, focused classification of the ovary 80S monosome dataset (185,913 particles) was performed. This produced 4 significant classes, together representing 97.16% of dataset particles. mRNA channel inspection found all four significant classes were found to be tRNA absent. The complete absence of tRNAs from any of the classes is highly suggestive that ovary 80S monosomes are not actively translating (Figure 42). These classes are likely to be ‘vacant couples’, 80S monosomes formed in the absence of mRNA.

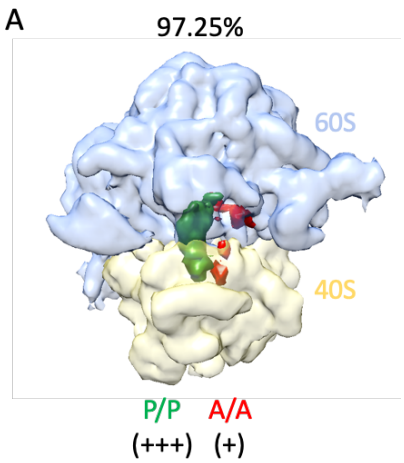

Figure 41. Significant classes resulting from focused classification of the testis 80S polysome dataset (10,392 particles). (A) 97.25% (10,106) dataset particles, containing a strong P/P tRNA (green) density and a faint A/A tRNA (red) density. 60S is light blue and 40S is yellow. mRNA channel densities were qualitatively scored on a scale of full (+++), partial (++) and faint (+).

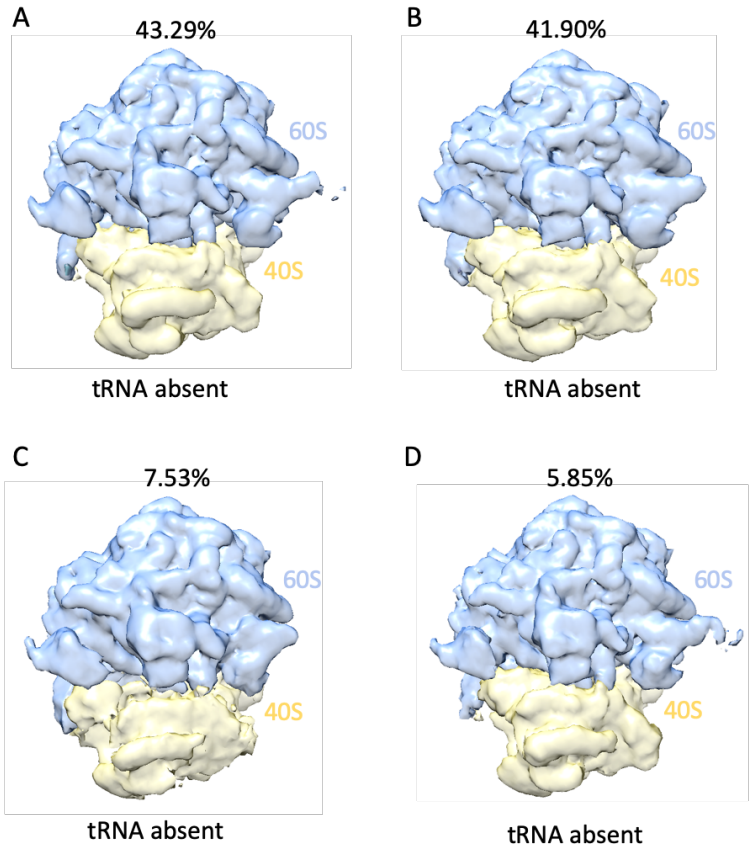

Figure 42. Significant classes resulting from focused classification of the ovary 80S monosome dataset (185,913 particles). (A) 43.29% (80,480) dataset particles, tRNA absent. (B) 41.90% (77,897) dataset particles, tRNA absent. (C) 7.53% (14,001) dataset particles, tRNA absent. (D) 5.85% (10,879) dataset particles, tRNA absent. 60S is light blue and 40S is yellow. mRNA channel densities were qualitatively scored on a scale of full (+++), partial (++) and faint (+).

5.10 Comparison of tRNA occupancy across *D. melanogaster* tissues

Comparative translational state and tRNA occupation analysis of the available *D. melanogaster* tissue ribosome datasets confirmed as expected that the ovary and testis 80S monosomes were translationally inactive, whereas the testis and embryo polysomes were determined to be translationally active. This analysis also demonstrated clearly that unexpectedly, the majority of head, and somewhat surprisingly, most embryo 80S monosomes are also translationally active. This is evident from the multiple translational states present in these datasets (Table 11). Moreover, head 80S monosomes were determined to present a similar level of tRNA occupation to the testis 80S polysomes and the embryo 80S foot-printed polysomes (97.25% and 99.23% vs. 97.59%, respectively), and therefore I can conclude that they are all similarly translationally active. Additionally, the embryo 80S monosomes tRNA occupation was only marginally lower than the polysome datasets (91.22%), suggesting that they are also highly translationally active. This is in contrast to the IFRD1 occupied testis 80S monosomes and mRNA channel vacant ovary 80S monosomes where no tRNAs were detected in any significant focussed class and are therefore translationally inactive (Table 12, Figure 43).

Table 11. tRNA occupation and determined translational stages of the significant focused classes of *D. melanogaster* tissue ribosome datasets. The *D. melanogaster* tissue ribosome datasets analysed were the head 80S monosome (610,605 particles), embryo 80S monosome (11,446 particles), embryo 80S foot-printed polysome (34,603 particles), testis 80S monosome (46,878 particles), testis 80S polysome (10,392 particles) and ovary 80S monosome (185,913 particles). Significant focused classes with the same tRNA occupancy have been combined.

Dataset	Percentage of particles (%)	mRNA channel occupation assessment	Determined translational stage
Head 80S monosome	60.55	A/A tRNA, P/P tRNA	Elongation – Peptide bond formation/pre-translocation
	18.55	A/P tRNA, P/E tRNA	Elongation – Hybrid state
	18.50	P/P tRNA	Elongation – E/E site ejection or possible CHX incorporated post-translocation
	2.29	tRNA absent	N/A
Embryo 80S monosome	83.06	P/P tRNA, E/E tRNA	Elongation – Post-translocation
	5.94	tRNA absent - resolution limited	Undetermined
	5.75	tRNA occupied - resolution limited	Undetermined
	2.41	tRNA occupied - resolution limited	Undetermined
Embryo 80S foot-printed polysome	53.13	A/P tRNA, P/E tRNA	Elongation - Hybrid state
	43.18	P/P tRNA, E/E tRNA	Elongation - Post-translocation
	1.67	tRNA occupied - resolution limited	Undetermined
	1.25	A/A tRNA, P/P tRNA	Elongation – Peptide bond formation/pre-translocation
Testis 80S monosome	98.72	IFRD1	N/A
Testis 80S polysome	97.25	A/A tRNA, P/P tRNA	Possible combination of elongation states – Peptide bond formation/pre-translocation and E/E site ejection or possible CHX incorporated post-translocation
Ovary 80S monosome	98.57	tRNA absent	N/A

Table 12. Percentage of all *D. melanogaster* tissue ribosome particles that are tRNA occupied, tRNA absent and undefined. Undefined particles were determined to be the particles that were not included in the significant focused classes.

***D. melanogaster* tissue ribosome dataset**	**tRNA occupied dataset particles (%)**	**tRNA absent dataset particles (%)**	**Undefined dataset particles (%)**
Head 80S monosome	97.59	2.29	0.12
Embryo 80S monosome	91.22	5.94	2.84
Embryo 80S foot-printed polysome	99.23	0	0.77
Testis 80S monosome	0	98.72	1.28
Testis 80S polysome	97.25	0	2.75
Ovary 80S monosome	0	98.57	1.43

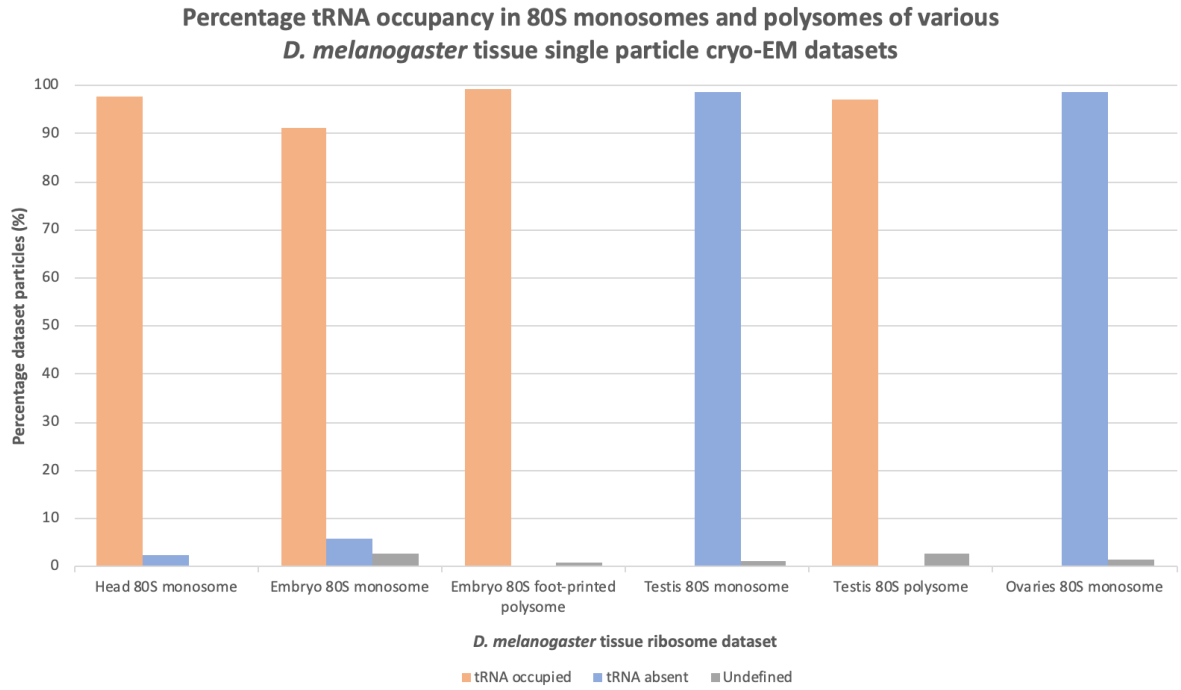

Figure 43. Percentage *D. melanogaster* tissue ribosome particles that are tRNA occupied, tRNA absent and undefined particles. Orange; tRNA occupied particles, blue; tRNA absent particles, grey; undefined particles.

5.11 Discussion

The final aim of this project was to determine the translational profile of monosomes across different *D. melanogaster* tissues. I answered this aim by performing tRNA occupation quantification and assessment of *D. melanogaster* tissue 80S monosomes and polysomes. I have verified that focus classification is a suitable method to analyse and quantify tRNA occupation in *D. melanogaster* tissue ribosome cryo-EM analysis datasets. tRNA occupation analysis found that as expected the significant focused classes of all testis and embryo polysomes were actively translating, whereas the significant focused classes of all testis and ovary 80S monosomes were not actively translating. Unexpectedly, focus classification detected that the vast majority of head and (and less unexpectedly) embryo 80S monosomes are in a state of active translation.

5.11.1 Head 80S monosomes are engaged in active translation

Structural analysis of the head 80S monosome average detected strong densities of all 3 classical tRNAs in the mRNA channel, indicating that most head 80S monosomes are in a state of active translation (Figure 35). This was a surprising finding as monosomes have long been assumed to be far less translationally active than polysomes. Although the existence of translationally active monosomes has been established and the type of transcripts they preferentially translate is now defined, the extent and proportion of monosomes in active translation compared to vacant couples is as yet undetermined (Heyer and Moore, 2016). Therefore, I was interested to determine the translational states of these ribosomes and the proportion of these monosomes that were actively translating in comparison to other *D. melanogaster* tissues. Notably, it seemed very unlikely that the increased RpS11 stoichiometry in head tissue investigated in this project was inducing monosomal translation, as TMT-MS analysis determined RpS11 to be highly incorporated into both the monosomal and polysomal fractions (Hopes et al., 2021).

5.11.2 Head 80S monosome tRNA occupation analysis

Focused classification was used to determine the extent and proportion of these monosomes in active translation by assessing and quantifying tRNA occupation. The focused classification and contour level at which to properly assess tRNA occupation was validated using the head 80S monosome cryo-EM particle dataset (Figures 36 and 37). The resultant significant focused classification classes determined that ~98% of head 80S monosomes are engaged in active translation and ~2% are vacant couples (Figures 37 and 43, Table 12). This is suggestive that monosomal translation is utilised in the head tissue, and more specifically the brain, as a form of translation regulation and is required for translation of specific mRNA transcripts. This notion is supported in the literature: monosomal

translation was found to be major source of proteins in the axons and dendrites of rodent neurons. These monosomes were found to translate distinct pools of mRNA in comparison to mRNAs that are being translated by polysomes in the soma (Biever et al., 2020). However, as these 80S monosomes used in my study were from head tissue, this implies that monosomes in the brain are actively translating no matter how close to the axons or dendrites. Since the brain only makes up 14% of the dry mass of the head tissue (Posey et al., 2001), this potentially also implies that glia cells as well as the other brain cells and tissues of the head (e.g., eyes, proboscis, antennae, pharynx etc.) also contain actively translating monosomes.

~61% of the total particles formed ribosomes I determined to be representative of the elongation stages of peptide bond formation and pre-translocation (Figure 37A, D, E, Table 11). Differentiation of these 2 stages cannot be carried out at this resolution as they both have the same tRNA conformation and only differ in tRNA acetylation. Both A/A and P/P tRNAs are acetylated prior in the peptide bond formation state, whereas the P/P tRNA is deacetylated in the pre-translocation state and A/A is acetylated (Dever et al., 2018). Therefore, analysis with higher resolution cryo-EM averages could be performed to allow the visualisation of acylated and unacetylated tRNAs to differentiate between ribosomes in the peptide bond formation state and those in the pre-translocation state.

~19% of all particles formed a focused class that was designated to be in the hybrid state of translocation in the elongation phase, due to the presence of intermediate A/P and E/P tRNAs (Figure 37B and Table 11). This shows that the hybrid state is a well occupied state of elongation in head 80S monosomes. ~19% of particles formed ribosomes with only P/P tRNA densities that were accounted to be representative of E/E site ejection and possibly the post-translocation stage after CHX binding. The CHX mechanism of action is not exactly known, however after binding to the E/E site, CHX has been found to allow for an extra round of translocation (Pestova and Hellen, 2003). Higher resolution analysis could confirm the presence of CHX to confirm this interpretation. Although P/P tRNA site occupation is suggestive of both initiation and termination phases (Figure 4), I determined that this was not likely as no eIF or eRF densities were detected in the mRNA channel. Furthermore, initiation and termination only occur once during translation whereas elongation is a cyclical process repeated for each additional ORF codon until the stop codon is reached (Schuller and Green, 2018). Therefore, it is unlikely that enough 80S ribosomes would be in the initiation and termination phases to be resolved in a significant focussed class.

5.11.3 Embryo 80S monosomes tRNA occupation analysis

The focused classification of the embryo 80S monosome dataset determined that ~91% of monosomes were actively translating and 5.94% were vacant couples (Figure 38, 43 and Table 12). This was an expected result as E/E tRNA and eEF2 densities were resolved in a previously published atomic model of *D. melanogaster* embryo 80S monosomes (Anger et al., 2013). As the embryo 80S monosome dataset was relatively small (~11,000 particles), only 1 focused class was of high enough resolution for a confident tRNA assessment to be made, consisting of ~83% of the total dataset particles. This class contained partial E/E and P/P site tRNA densities, which I designated as representing the post-translocation elongation stage (Figure 38A). Notably no detection of eEF2 in the post-translocation state focused class of this dataset, which was expected due to the inclusion of CHX in the ribosome purification protocol (Section 2.7.2), as CHX acts as an inhibitor of elongation by binding the E/E site, preventing the binding of eEF2 (Schneider-Poetsch et al., 2010). Although eEF2-GDP dissociates after post-translocation (Dever et al., 2018), there was no detection of any eEF2 densities implying that CHX is likely incorporated into most embryo 80S monosomes. The embryo 80S monosome translational state did not show the same single tRNA occupancy of the E/E site in the published embryo 80S monosome atomic model (Anger et al., 2013). This is likely due to a combination of factors. For example, the absence of CHX in this ribosome purification protocol meant that translation was not halted in these ribosomes. In addition, the embryo extract was derived from 0-12 hour embryos, whereas our embryo 80S ribosomes were derived from 0-2 hour embryos. Furthermore, this atomic model was based on the dataset particle average and individual translational states were not investigated, so other tRNA sites may be occupied but not resolved in the global average.

Assessment of the poorly resolved classes determined 2 were confidently showing tRNA occupation (representing 5.94 and 5.75%, respectively) and one class was tRNA absent. To better characterise the translational states of the embryo 80S monosomes, analysis of a much larger dataset is required. This could be achieved by reperforming embryo 80S monosome cryo-EM sample preparation with significantly more input material. This may result in a more concentrated sample being applied to cryo-EM grids to allow for the detection of more monosome particles during cryo-EM data collection.

Detection of tRNA occupancy in ~91% of monosomes implies, similar to head 80S monosomes, that monosomal translation is utilised in the embryonic tissue as a form of translation regulation and is required for translation of specific mRNA transcripts. Moreover, monosomes have been established to preferentially translate uORF containing transcripts (Heyer and Moore, 2016). Genome-wide

averages of ribosomal occupancy during the *D. melanogaster* lifecycle found that 49.3% of uORFs (17,603 out of 35,735) expressed were ribosome occupied during the embryos at 0–2-hours (Zhang et al., 2018). This is the same stage that the embryos were collected for my analysis. Therefore, embryonic monosomal translation may be the result of specific translational control mechanisms and large number of uORFs translated during early embryo development (Patraquim et al., 2020).

5.11.4 Foot-printed embryo polysome tRNA occupation analysis

The foot-printed embryo polysomes found that all significant focused classes were tRNA occupied (~99% particles), as expected (Figure 39, 43 and Table 12). As this dataset was selected as a positive control, this result is an additional validation of the focused classification method in resolving and quantifying the translational states of *D. melanogaster* tissue ribosome datasets. Notably, this dataset resolved 4 out of 5 tRNA states of elongation: peptide bond formation and pre-translocation (~1% particles) (Figure 39D), the hybrid state (~53% particles) (Figure 39A) and post-translocation (~43% particles) (Figure 39B).

As seen in the embryo 80S monosome, and in contrast to the head 80S, the foot-printed embryo polysome post-translocation state contained both P/P and E/E tRNA densities. As both embryo and head tissues were treated with the same concentration of CHX (100 μg/mL) during cellular lysis, this could suggest that concentration of ribosomes is much higher in embryo tissue than in heads. Therefore, CHX induced states may be underrepresented in focused classes. Alternatively, this observation could also imply that embryo ribosomes are less susceptible to CHX incorporation than head 80S monosomes.

5.11.5 Testis 80S monosome tRNA occupation analysis

It has been previously described that testis 80S ribosomes contain IFRD1 in the P/P and E/E sites, but it was not determined the percentage that were occupied. It was assumed that most, but not all testis 80S monosomes were occupied (Hopes et al., 2021). However, focused classification determined that ~99% of all particles contained IFRD1 densities and no tRNAs were detected. Therefore, in contrast to the head 80S and embryo 80S monosomes, no testis 80S monosomes were detected to be actively translating (Figures 40, 43 and Table 12). This strongly implies that IFRD1 is a potent inhibitor of translation in the testis. A possible mechanism of IFRD1 inhibition influencing translational regulation could be by stalling ribosomes by stably binding the 60S and 40S subunits restricting formation of actively translating monosomes and polysomes.

This extremely high level of IFRD1 occupation in testis 80 monosomes is in contrast to the rabbit reticulocyte 80S ribosomes where approximately 20% of translationally inactive ribosomes were bound by IFRD2, an orthologous protein to *D. melanogaster* IFRD1 (Brown et al., 2018). Notably all IFRD2 containing rabbit reticulocytes were also bound by a Z site tRNA, a non-canonical tRNA binding site. The Z site tRNA has only been identified in these inactive rabbit reticulocytes ribosomes, both in the presence and absence of IFRD2 (Brown et al., 2018). Focused classification of the testis 80S monosomes did not find any densities at any level occupying the Z tRNA site. This could suggest that the mechanism of IFRD1 inhibiting translation is different in *D. melanogaster* testis 80S monosomes compared to IFRD2 in the rabbit reticulocyte ribosomes. This seems likely due to the relatively high amino acid sequence conservation of these two orthologs (37% identity) (Hopes et al., 2021).

It was suggested that IFRD2 (the rabbit ortholog of IFRD1), impacted translational regulation during differentiation (Brown et al., 2018). As differentiation is a key process of spermatogenesis, this is likely the same role that IFRD1 is playing in the testis 80S monosomes (Demarco et al., 2014). The role of IFRD1 in inhibiting translation in the testis could be characterised by performing UAS-GAL4 RNAi mediated knockdown of IFRD1. It seems likely that in the absence of IFRD1 monosomal translation would be induced or that the levels of polysomal translation would increase and presence of monosomes would decrease. Gross inspection of testes dissected from knockdown progeny compared to WT would indicate if translation regulation by IFRD1 impacts the normal structure, formation and function of the testis. Moreover, ribosome foot-printing of monosomal and polysomal fractions in knockdown progeny compared wild type would confirm if any monosomal translation is occurring and what transcripts this impacts and whether they relate to differentiation during spermatogenesis.

5.11.6 Testis 80S polysome tRNA occupation analysis

As expected, focused classification demonstrated that all testis 80S polysomes in the significant focused classes were actively translating (~97%) (Figures 40, 43 and Table 12). However, due to the relatively small size of the dataset (10,392 particles) only one tRNA conformation was resolved by focus classification. This focus class contained a strong P/P site tRNA and a partial tRNA A/A, indicating that due to the unequal strength of the tRNA densities this was likely representing two elongation state tRNA conformations: peptide bond formation and pre-translocation (A/A and P/P), and E/E site ejection or possibly CHX incorporated post-translocation (P/P). The detection of only one tRNA conformation could suggest that the polysomes are frozen in one translational state, however due to the difference in strength of the tRNA densities detected (as defined by visual inspection of the tRNA densities at the mean + 1σ contour level), this is very unlikely. Moreover, polysomes are known to be

translationally active and due to the finding of ~99% of testis monosome particles being IFRD1 occupied and therefore translationally inactive, it is impossible that all 80S ribosomes in testis tissue are translationally inactive. Therefore, focused classification of testis 80S polysomes must have resolved a combination of multiple elongation stages.

5.11.7 Ovary 80S monosome tRNA occupation analysis

tRNA occupation analysis and quantification determined that 98.57% dataset particles formed 80S ribosomes formed in the absence of mRNA (vacant couples) (Figure 41, 43 and Table 12). This result also shows that IFRD1 is not inactivating monosomal translation in any of the ovary 80S monosome, as previously suggested (Hopes et al., 2021). This result was more surprising than the detection of no translational activity in testis 80S monosomes, as focus classification detected no additional densities, within the mRNA channel or the ribosome that could be inhibiting monosomal translation. This therefore implies that 80S monosomal translation is being repressed by an unknown mechanism. Further analysis of ovary 80S TMT-MS data may determine a translational repressor or else could suggest there is much less monosomal translation, and therefore translation of monosome associated transcripts, in the ovaries than the testis.

This finding is in contrast to the determination of eEF2 occupying vacant couples and stably binding the 80S ribosomes in HEK293 cell lysates (Liu and Qian, 2016), no eEF2 densities were present in the ovary 80S monosome focus classes. This is likely due to the occupation of CHX in the E/E site, preventing eEF2 binding (Pestova and Hellen, 2003). This indicates that in ovary 80S monosomes that eEF2 is not required for the stable binding of ribosomal subunits to form vacant couples. eEF2 is unlikely to occupy testis 80S monosomes vacant couples due to IFRD1 occupation across the P/P and E/E sites potentially blocking eEF2 binding sites in the mRNA channel.

5.11.8 Comparison of tRNA occupation in all D. melanogaster tissue ribosome datasets

This tRNA occupancy quantification and analysis has shown that not only are monosomes of the head and embryo tissue active translating, but almost all of the monosomes in these tissues are actively translating. Notably head 80S monosomes were found to be as tRNA occupied (and therefore as actively translating) as the embryo foot-printed and the testis 80S polysomes, whereas embryo 80S monosomes were slightly less tRNA occupied (~7-8%). This could also imply that head and embryo tissues are performing localised translation in small volume regions of cells such as axons where visualisation of polysome complexes is generally unseen due to their large size being unable to be accommodated (Biever et al., 2020; Holt and Schuman, 2013; Steward and Schuman, 2003). This is

starkly different in the testis 80S monosomes, where IFRD1 appears to be actively inhibiting translation of all monosomes detected by focused classification. In contrast, all ovary 80S monosomes in significant focused classes were found to be tRNA absent without any extra ribosomal factors detected that could be inhibiting translation. As no level of translational activity was detected in these tissues, this suggests that monosomal translation is not necessary for the translation of any transcripts vital to normal testis and ovary function. Moreover, this could imply that there are very low levels of the transcripts found to be favoured in monosomal translation such as short ORFs and NMD targets, uORF containing mRNAs and low abundance proteins (Heyer and Moore, 2016).

Across all *D. melanogaster* tissue ribosome datasets, of the tRNA occupied 80S ribosomes, the focused classification only resolved significant focused classes that were in the elongation phase (Table 11). This presence of only elongation states in *D. melanogaster* tissue ribosome datasets is similar to ribosome profiling of yeast 80S monosomes that found the majority of monosomes are engaged in elongation (Heyer and Moore, 2016). Furthermore, monosomes have been thought to be 'pioneer ribosomes', initiating 80S ribosomes, which bind to the mRNA transcript before it has moved far enough along the transcript to allow a second 80S ribosome to bind and form a polysome complex (Heyer and Moore, 2016). The detection of no initiating stages in head 80S and embryo 80S monosomes therefore could suggest that these monosomes are not representative of these pioneer ribosomes but are truly actively translating monosomes. However, as discussed, due to very few actively translating ribosomes likely to be initiating compared to elongating, initiation would be unlikely resolved by focus classification. To determine the presence of pioneer ribosomes in embryo and head 80S monosomes, ribosome profiling could be carried out to determine the mRNA codons they occupy. Any monosomes occupying AUG codons in the P/P site would be considered to be initiating.

Although multiple elongation tRNA conformations and therefore elongation states were detected, I did not however detect any eEFs. As discussed, this is in contrast to the eukaryotic extract 80S monosome which detected eEF2 and E/E site tRNA (Anger et al., 2013), due to inclusion of CHX in ribosome purification. Hence, no detection of eEF2 densities in the assigned hybrid and post-translocation states in the other actively translating tissue ribosomes suggests that CHX was well incorporated into all tissue ribosomes analysed. In addition, I determined that no significant focused classes of any of the datasets analysed resolved the A/A site tRNA selection stage, consisting of A/A site and P/P site occupation, where eEF1A-GTP is bound to the A/A site tRNA (Figure 4) (Rodnina et al., 2005). Notably CHX incorporation should not impact eEF1A binding, as eEF1A delivers tRNAs to

the A/A site, whereas CHX prevents eEF2 binding by binding to the E/E site (Rodnina et al., 2005; Schneider-Poetsch et al., 2010). A/A site selection has been resolved by cryo-EM in *E. coli* ribosomes, showing A/A site and P/P site occupation, with EF-Tu-GTP (the prokaryotic homolog of eEF1) bound to the A/A site tRNA (Loveland et al., 2020). However, this state was resolved by incubation of the *E. coli* ribosomes with Phe-tRNA-EF-Tu-GTP, which allowed visualisation of this state (Loveland et al., 2020). This could suggest that this stage is too transient to be resolved by cryo-EM *in vivo* or that by halting elongation, CHX incorporation may prevents further A/A site tRNAs being delivered to the ribosome by eEF1A.

6 Discussion

6.1 Assessment of RpS11 enrichment in head ribosomes

This project set out to establish the role of ribosomal heterogeneity by changes in RpS11 stoichiometry in *D. melanogaster* head tissue, which was employed as a proxy for the brain. This was prompted by the reported significant enrichment of RpS11 in head tissue ribosomes as detected by TMT-MS (Hopes et al., 2021). This finding was verified by RpS11 peptide fragment detection analysis, although it was unclear if this was the detection of the full-length peptide and not a truncated version. Therefore, I investigated the impact of this enrichment through RNAi knockdown and cryo-EM structural analysis of head 80S monosomes. Structural analysis however could not determine structural consequences of RpS11 enrichment. Further investigation is required to establish the role of RpS11 stoichiometry in brain and head tissue development and function, and if it impacts translation of specific mRNAs or global translation. Therefore, considering the inconclusive results of RpS11 heterogeneity as assessed by UAS-GAL4 RpS11 RNAi-mediated knockdown as well as this structural analysis, the roles of RpS11 stoichiometry in head tissue translation is as yet undetermined.

Potentially the significant RpS11 enrichment in head ribosomes could be only playing a role in the normal adult brain function, since enrichment was detected in adult head ribosomes. Therefore, the significance of RpS11 enrichment may not be apparent in knockdown of the developing *D. melanogaster* brain, as was carried out in the RpS11-RNAi knockdowns performed. This could be investigated by the employment of adult brain drivers to drive expression of RpS11-RNAi, such as heat shock inducible RpS11-RNAi drivers (Grabher and Wittbrodt, 2004). Alternatively, auxin-inducible gene expression system (AGES) could be combined with *elav*-GAL4 to only induce expression of RpS11-RNAi after development by adding auxin to the fly food of adult flies (McClure et al., 2022). Alternatively, injection of short RpS11 double stranded RNA transcripts to the abdomen of anesthetised adult WT *D. melanogaster* could induce RNAi. This method has been previously shown to knockdown *LacZ* expression in the CNS of bacterial *lacZ*-expressing flies (Dzitoyeva et al., 2001).

The *elav*-GAL4 driver was used as elav is expressed in the *D. melanogaster* neurons and most embryonic glial cells (Berger et al., 2007). Therefore, it would be beneficial to confirm the expression of the *elav*-GAL4 line used to ensure that knockdown is only being performed in the target cells. This could be achieved by carrying out a cross with a UAS-fluorescent marker line (e.g. UAS-mCherry) to confirm the elav driver expression, by confocal microscopy of the resultant UAS-GAL4 progeny brains. Following confirmation of elav expression and successful RpS11-RNAi knockdown by western blot or

qPCR, as discussed, phenotypes of knockdown progeny could be assessed by dissecting brains and gross physiological inspection. In addition, the assessment of behavioural phenotypes (e.g., social behaviour, olfactory learning and habituation). Altered behavioural phenotypes from parental controls would indicate abnormal neuronal function (Nichols et al., 2012; Busto et al., 2010). Performing puromycin incorporation assays on RpS11-RNAi head tissue to measure the rate of protein synthesis would allow assessment of the importance of RpS11 stoichiometry in general translation in the head tissue(Nakano and Hara, 1979). Furthermore, to establish whether RpS11 enriched ribosomes translate specific mRNAs that are important to neural function/development, Ribo-seq could be utilised to assess differences in the translatome of these RpS11-RNAi knockdown ribosomes in comparison to WT, isolated by polysome fractionation (Ingolia et al., 2009). This would provide a snapshot of mRNA transcripts being actively translated and whether these relate to neuronal development or function. If RpS11-RNAi knockdown is lethal in *D. melanogaster*, as suggested by the production of no knockdown phenotype progeny in the *elav*-GAL4 UAS-RpS11-RNAi #23477 cross, the experiments discussed above could not be performed. In this case, incorporation of additional copies of RpS11 could be determined by producing a transgenic *D. melanogaster* line tagging RpS11 with both HA and FLAG tags (Kanca et al., 2017). Ribosomes would be isolated from this line by polysomal fractionation and would be subjected to confocal microscopy. Detection of both tags on the same ribosome would imply that multiple copies of RpS11 are present.

To confirm if head ribosomes contain different length versions of RpS11, western blot could be used to determine if RpS11 is detected at the correct molecular mass (18.1 kDa). Cryo-EM analysis confirmed the presence of the single full-length copy (Figures 30-34). Therefore, if additional truncated versions of RpS11 were also incorporated into the head ribosomes this may explain the significant enrichment of RpS11 and why no additional copies of RpS11 could be detected by cryo-EM. To ensure there are no additional RpS11 densities associated with the exterior of the ribosome, re-post-processing the refined models with larger, softer masks may reveal additional RpS11 densities outside of the ribosome previously excluded by tight fitting masks. If no extra RpS11 densities are identified in re-post-processing, head 80S monosome particles could be repicked using larger box sizes to ensure any additional densities surrounding the ribosome are included during particle picking.

As the enrichment of RpS11 detected by TMT-MS in head ribosomes was derived from ribosomal fractions after sucrose centrifugation, RpS11 must be interacting with the ribosome. Alternative explanations to the reported RpS11 enrichment could be due to RpS11 playing an extra ribosomal RNA binding role in head tissue ribosomes; or perhaps post-translational modifications of RpS11 allows for

more efficient detection by TMT-MS possibly preventing protein turnover or degradation. It is worth noting that if additional copies of RpS11 were present in inconsistent locations, they would not be seen in the cryo-EM averages; a possible approach to test if this is the case would be to use both native (native-MS) and cross-linking mass spectrometry (XL-MS). Native-MS allows for intact ribosomes to enter the mass spectrometer and non-covalent interactions would be preserved, therefore enabling accurate measurement of the stoichiometry of RpS11, confirming the presence of additional copies (van de Waterbeemd et al., 2018). Once this was confirmed, XL-MS would be employed. The use of amine reactive cross-linkers in cross linking mass spectrometry retains structural interactions of RPs (Tüting et al., 2020). This would determine which proteins that RpS11 could be interacting with. An additional possible explanation of no structural evidence of additional RpS11 densities is that additional copies of RpS11 are associating with the head 80S monosome but are not stable enough to persist. Therefore, use of the Gradient Fixation (GraFix) method could be applied, which uses chemical cross-linking during density gradient ultracentrifugation to stabilise weak molecular interactions, reducing RpS11 dissociation during cryo-EM grid preparation (Stark, 2010).

Notably the brain makes up a very small proportion of the head tissue, the dry weight of the *D. melanogaster* brain is only 14% of the head tissue (Posey et al., 2001). Therefore, RpS11 is also likely to be significantly enriched in the ribosomes of other tissues of the head as well as the brain, including the eyes, pharynx, proboscis, maxillary palps, bristles, antennae, antennae segments etc. To further implicate the enrichment of RpS11 as impacting RpS11 stoichiometry in the brain tissue ribosomes and therefore, its relevance to translation of transcripts required for normal brain development could be investigated. TMT-MS analysis could be performed using brain tissue as well as the other *D. melanogaster* tissue ribosomes. This would determine if RpS11 is enriched in brain tissue ribosomes, in comparison to other tissues, to the same extent as head tissue monosomes.

This series of experiments and analysis will further the understanding of the role ribosomal heterogeneity plays in neuronal function, as well as potentially elucidating specialised ribosome mechanisms.

6.2 tRNA occupation of *D. melanogaster* ribosomes

Structural analysis of the head 80S monosome cryo-EM average by focused classification surprisingly showed that nearly all (98%) head 80S monosomes were actively translating. This novel observation led to the question: are 80S monosomes also translating in other *D. melanogaster* tissues and if so to what extent? Therefore, tRNA assessment and quantification was carried out and determined that,

unexpectedly, the vast majority (91%) of 0-2h embryo 80S monosomes are also actively translating. In contrast, there was no detection of translation in the testis and ovary 80S monosomes. Interestingly, all testis 80S monosomes were found to be occupied by IFRD1, inhibiting translation. In contrast, ovary 80S monosomes formed vacant couples in the absence of any detectable additional factors. As expected, I established all embryo 80S foot-printed and testis polysomes were actively translating. These findings suggest that monosomal translation is a form of translational regulation and is required in head and embryo tissues for translation of specific mRNA transcripts, not expressed in testis or ovary tissue.

To further dissect the implications of 80S monosomal translation in head tissue, cryo-EM analysis of the *D. melanogaster* brain and brain cells could be carried out to determine the extent of monosomal translation in these settings. Moreover, ribosome foot-printing of the brain and brain cells could determine the specific transcripts that are expressed by monosomal translation.

Cryo-EM of embryos from other time points and specific embryo cell monosomes could determine the extent of monosomal translation during *D. melanogaster* development. In addition, ribosome profiling of the embryo tissue could be carried out to determine the types of transcripts and specific transcripts that monosomal translation is favouring. This has been already performed in polysomes however not in monosomes (Patraquim et al., 2020). Therefore, it would be very interesting to compare the polysome associated transcripts to the monosome associated.

6.3 General conclusions and significance

The role of the reported RpS11 enrichment in head ribosomes remains elusive but is very suggestive of RpS11 holding a significant role in the development or function of the *D. melanogaster* brain. This warrants further investigation to determine the significance of this enrichment in the specific tissues of the head, as well as any translational roles it may hold in the brain. Better understanding of RpS11 in the *D. melanogaster* brain could shed light on neurodegenerative conditions and brain cancers in humans, leading to new treatments.

The analysis of tRNA occupation and quantification implies that monosomal translation in *D. melanogaster* tissues is a form of translational control that is important for the translation of specific transcripts in embryo and head tissues. These results have much significance in the field of translation. This project has shown for the first time that *D. melanogaster* head 80S monosomes are actively translating, implicating the brain tissues as also performing monosomal translation.

Moreover, by quantifying the level of active translation in both embryo and head 80S monosomes we have determined that the vast majority of these ribosomes are actively translating. It was astounding the clear-cut definition of active translation in these tissue and number of translational states that could be determined by focus classification, even in relatively small particle datasets such as the foot-printed embryo 80S polysomes. This work adds to the evidence redefining monosomes from being considered translationally unimportant, to a major source of translation as well as involved in the translation of highly regulated transcripts (Heyer and Moore, 2016; Biever et al., 2020). These results could impact many ribosome foot-printing studies which have only analysed polysomal fractions and disregarded the monosomal fractions. It would be very exciting to apply these methods to other species, in particular humans, and determine if monosomal translation is impacted in disease states. For example, translational regulation is known to be to be highly dysregulated in neurodegeneration and cancer (Kapur et al., 2017; Vaklavas et al., 2017). Therefore, characterising monosomal translation could further the understanding of these diseases and even allude to possible new treatments.

7 Supplementary Data

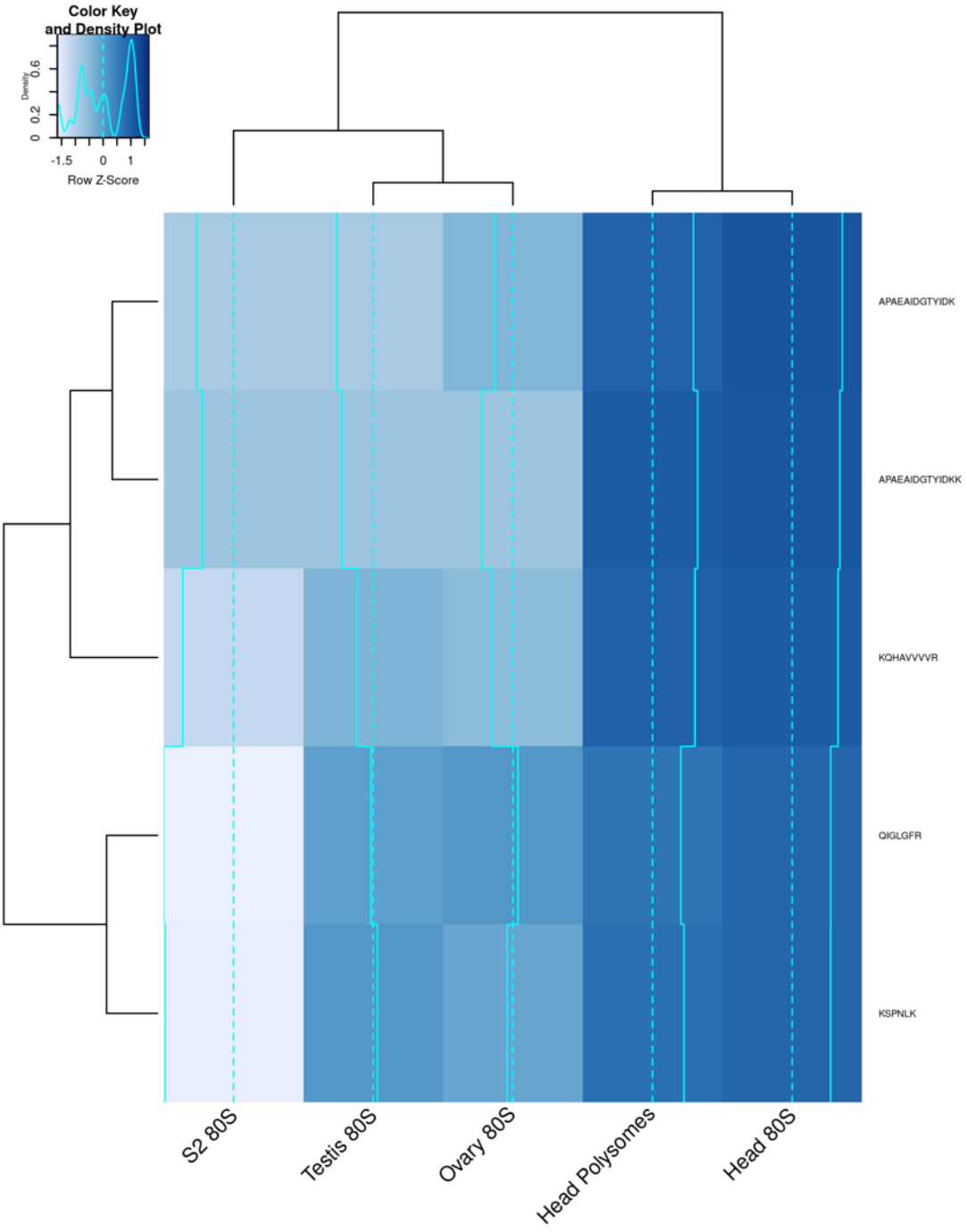

Supplemental figure 1. TMT-MS replicate 1 hierarchical clustering of log_{10} scaled normalised abundances of RpS11 peptide fragments in *D. melanogaster* tissue and cell culture ribosomes. Normalised abundances were scaled to a control pool (the average detection of all RP peptide fragments in all ribosome fractions) from which Z-scores were calculated and plotted, rows are clustered according to RpS11 peptide fragments. Peptide fragment normalised abundances were extracted from the TMT-MS data using RpS11 protein (Uniprot accession code A1Z8U9).

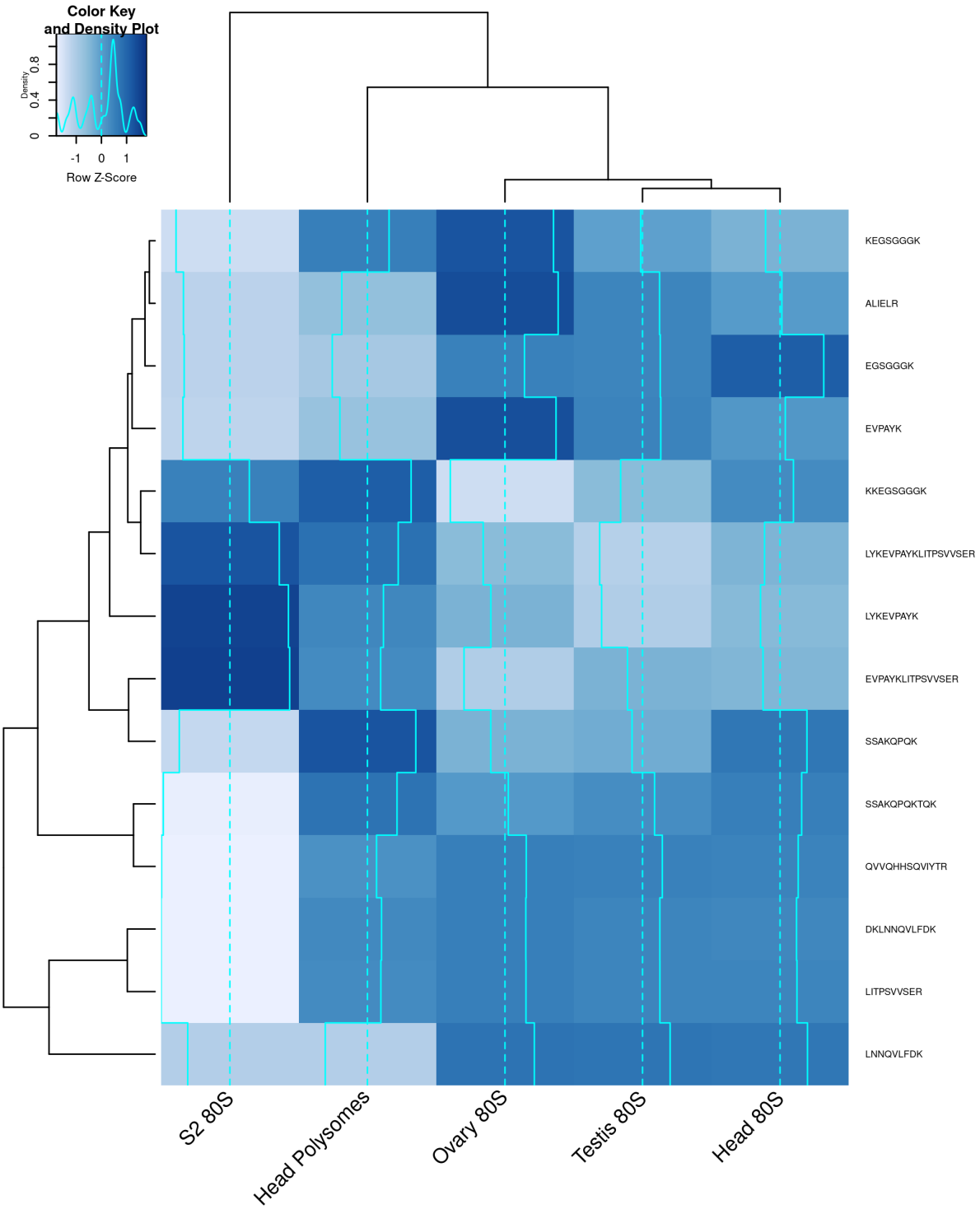

Supplemental figure 2. TMT-MS replicate 1 hierarchical clustering of log_{10} scaled normalised abundances of RpS25 peptide fragments in *D. melanogaster* tissue and cell culture ribosomes. Normalised abundances were scaled to a control pool (the average detection of all RP peptide fragments in all ribosome fractions) from which Z-scores were calculated and plotted, rows are clustered according to RpS25 peptide fragments. Peptide fragment normalised abundances were extracted from the TMT-MS data using RpS25 protein (Uniprot accession code P48588).

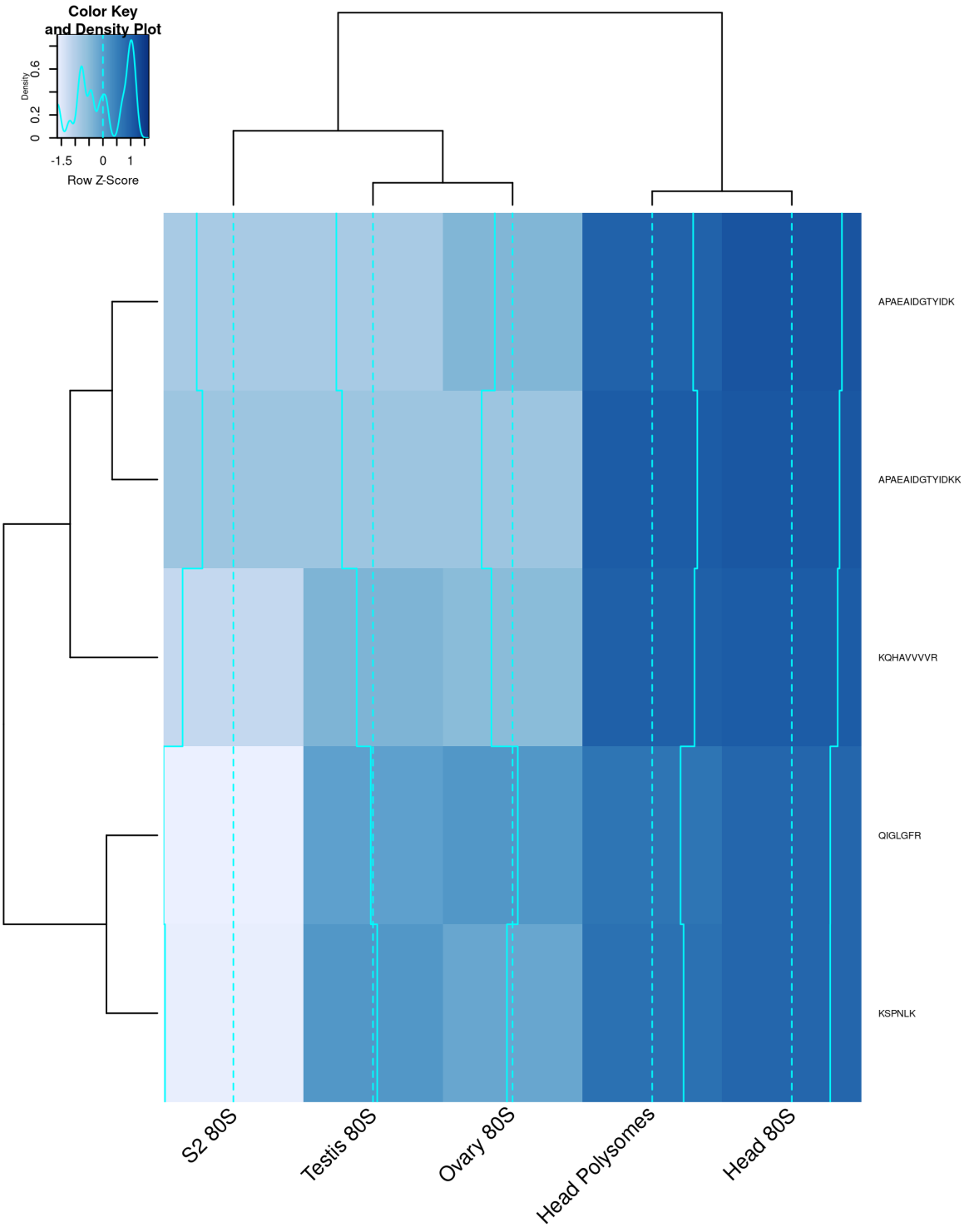

Supplemental figure 3. TMT-MS replicate 2 hierarchical clustering of log_{10} scaled normalised abundances of RpS11 peptide fragments in *D. melanogaster* tissue and cell culture ribosomes. Normalised abundances were scaled to a control pool (the average detection of all RP peptide fragments in all ribosome fractions) from which Z-scores were calculated and plotted, rows are clustered according to RpS11 peptide fragments. Peptide fragment normalised abundances were extracted from the TMT-MS data using RpS11 protein (Uniprot accession code A1Z8U9).

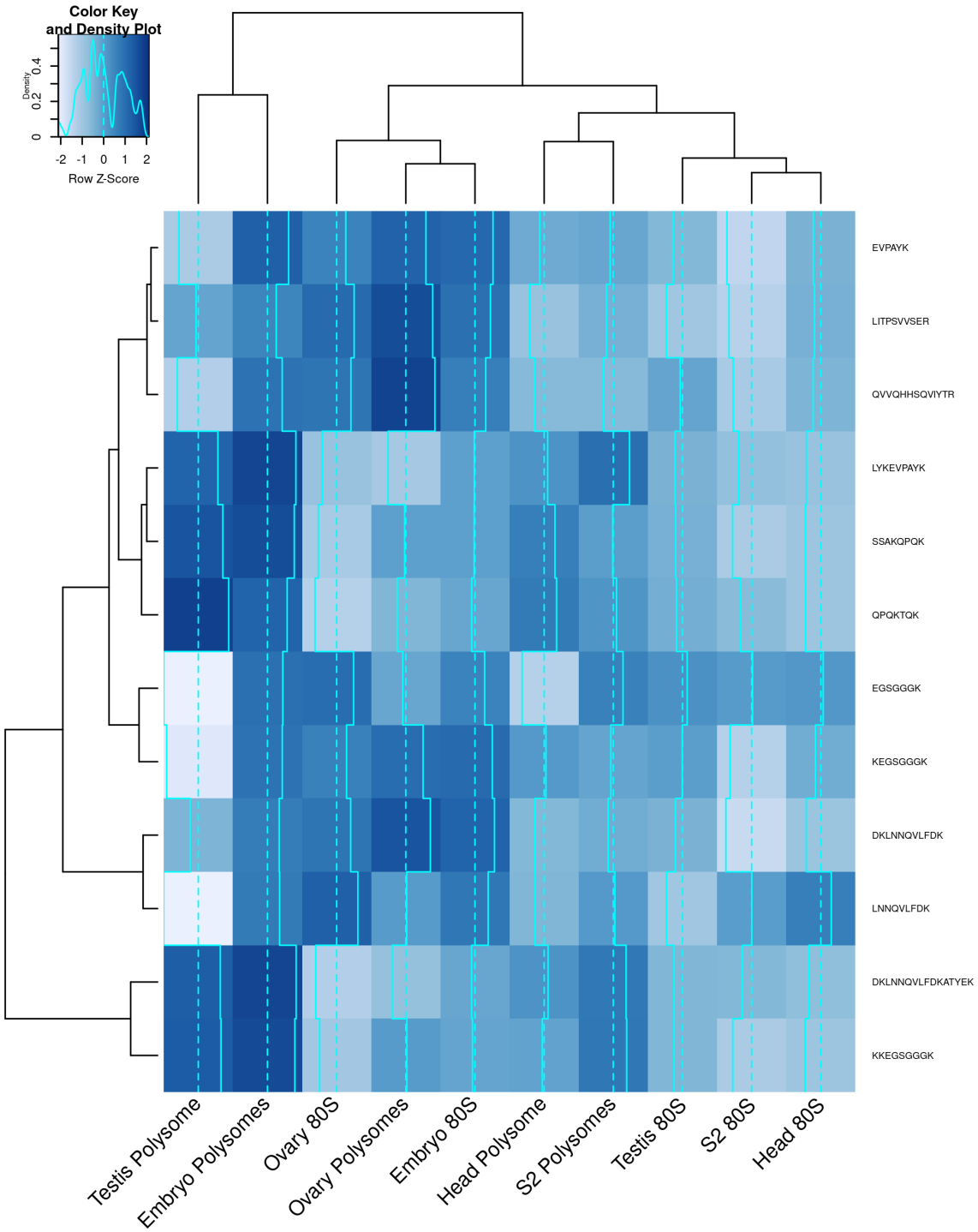

Supplemental figure 4. TMT-MS replicate 2 hierarchical clustering of log_{10} scaled normalised abundances of RpS25 peptide fragments in *D. melanogaster* tissue and cell culture ribosomes. Normalised abundances were scaled to a control pool (the average detection of all RP peptide fragments in all ribosome fractions) from which Z-scores were calculated and plotted, rows are clustered according to RpS25 peptide fragments. Peptide fragment normalised abundances were extracted from the TMT-MS data using RpS25 protein (Uniprot accession code P48588).

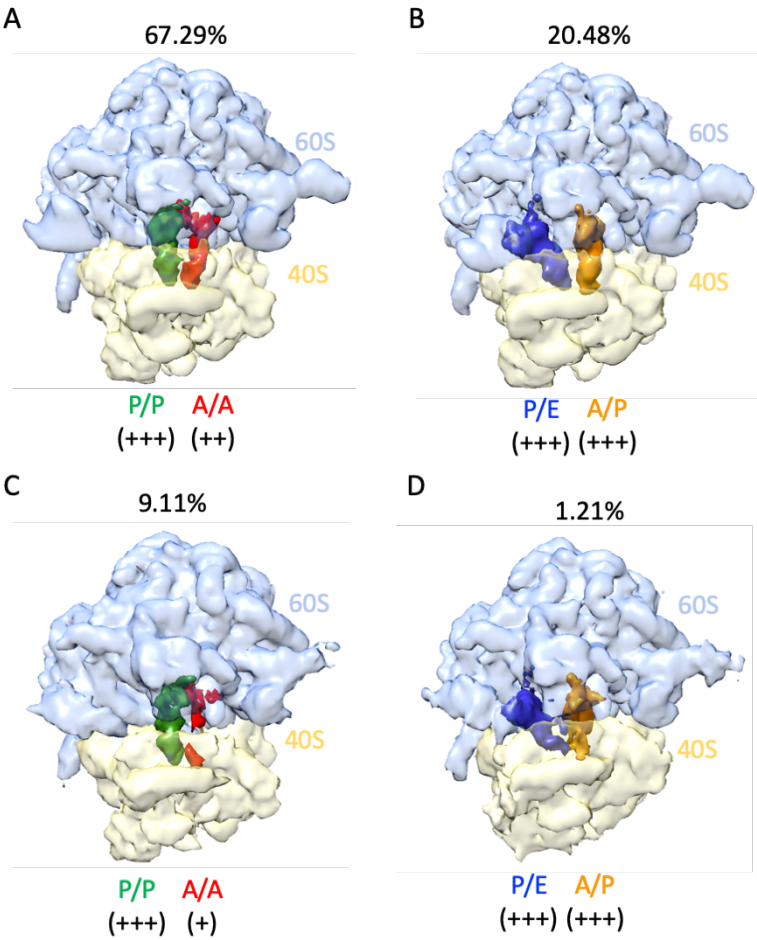

Supplemental figure 5. Significant classes resulting from the unmasked classification of the head 80S monosome dataset (610,605 particles) presented at the mean + 1σ contour level. (A) 67.29% dataset particles, containing a strong P/P tRNA (green) density and a partial A/A tRNA (red) density. (B) 20.48% dataset particles, containing strong P/E tRNA (blue) and A/P tRNA (orange) densities. (C) 9.11% dataset particles, containing a strong P/P tRNA (green) density and a faint A/A tRNA (red) density. (D) 1.21% dataset particles, containing strong P/E tRNA (blue) and A/P tRNA (orange) densities. 60S is light blue and 40S is yellow. mRNA channel densities were qualitatively scored on a scale of full (+++), partial (++) and faint (+).

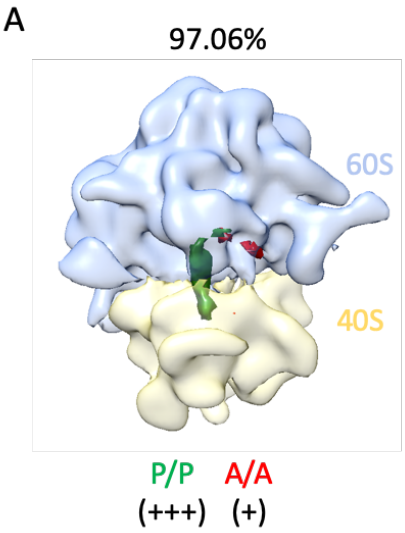

Supplemental figure 6. Significant classes resulting from focused classification of the testis 80S polysome dataset (10,392 particles). (A) 97.06% (10,087) dataset particles, containing a strong P/P tRNA (green) density and a faint A/A tRNA (red) density. 60S is light blue and 40S is yellow. mRNA channel densities were qualitatively scored on a scale of full (+++), partial (++) and faint (+).

8 Bibliography

Afonine, P.V., Klaholz, B.P., Moriarty, N.W., Poon, B.K., Sobolev, O.V., Terwilliger, T.C., Adams, P.D. and Urzhumtsev, A. 2018. New tools for the analysis and validation of cryo-EM maps and atomic models. *Acta Crystallogr D Struct Biol.* **74**(Pt 9), pp.814-840.

Aitken, C.E. and Lorsch, J.R. 2012. A mechanistic overview of translation initiation in eukaryotes. *Nature Structural & Molecular Biology.* **19**(6), pp.568-576.

Akirtava, C., May, G.E. and McManus, C.J. 2022. False-Positive IRESes from Hoxa9 and other genes resulting from errors in mammalian 5' UTR annotations. *bioRxiv.* p2022.2002.2010.479744.

Anger, A.M., Armache, J.P., Berninghausen, O., Habeck, M., Subklewe, M., Wilson, D.N. and Beckmann, R. 2013. Structures of the human and Drosophila 80S ribosome. *Nature.* **497**(7447), pp.80-85.

Barbosa, C., Peixeiro, I. and Romão, L. 2013. Gene expression regulation by upstream open reading frames and human disease. *PLoS Genet.* **9**(8), pe1003529.

Bass, T.M., Grandison, R.C., Wong, R., Martinez, P., Partridge, L. and Piper, M.D.W. 2007. Optimization of dietary restriction protocols in Drosophila. *The journals of gerontology. Series A, Biological sciences and medical sciences.* **62**(10), pp.1071-1081.

Baxter-Roshek, J.L., Petrov, A.N. and Dinman, J.D. 2007. Optimization of ribosome structure and function by rRNA base modification. *PloS one.* **2**(1), pp.e174-e174.

Behrmann, E., Loerke, J., Budkevich, T.V., Yamamoto, K., Schmidt, A., Penczek, P.A., Vos, M.R., Bürger, J., Mielke, T., Scheerer, P. and Spahn, C.M. 2015. Structural snapshots of actively translating human ribosomes. *Cell.* **161**(4), pp.845-857.

Berg, M.D. and Brandl, C.J. 2021. Transfer RNAs: diversity in form and function. *RNA Biol.* **18**(3), pp.316-339.

Berger, C., Renner, S., Lüer, K. and Technau, G.M. 2007. The commonly used marker ELAV is transiently expressed in neuroblasts and glial cells in the Drosophila embryonic CNS. *Dev Dyn.* **236**(12), pp.3562-3568.

Biever, A., Glock, C., Tushev, G., Ciirdaeva, E., Dalmay, T., Langer, J.D. and Schuman, E.M. 2020. Monosomes actively translate synaptic mRNAs in neuronal processes. *Science.* **367**(6477), peaay4991.

Brenner, S., Jacob, F. and Meselson, M. 1961. An unstable intermediate carrying information from genes to ribosomes for protein synthesis. *Nature.* **190**, pp.576-581.

Brown, A., Baird, M.R., Yip, M.C., Murray, J. and Shao, S. 2018. Structures of translationally inactive mammalian ribosomes. *Elife.* **7**.

Budkevich, T., Giesebrecht, J., Altman, R.B., Munro, J.B., Mielke, T., Nierhaus, K.H., Blanchard, S.C. and Spahn, C.M. 2011. Structure and dynamics of the mammalian ribosomal pretranslocation complex. *Mol Cell.* **44**(2), pp.214-224.

Busto, G.U., Cervantes-Sandoval, I. and Davis, R.L. 2010. Olfactory learning in Drosophila. *Physiology (Bethesda).* **25**(6), pp.338-346.

Cagney, G., Park, S., Chung, C., Tong, B., O'Dushlaine, C., Shields, D.C. and Emili, A. 2005. Human Tissue Profiling with Multidimensional Protein Identification Technology. *Journal of Proteome Research.* **4**(5), pp.1757-1767.

Carroll, A.J., Heazlewood, J.L., Ito, J. and Millar, A.H. 2008. Analysis of the Arabidopsis Cytosolic Ribosome Proteome Provides Detailed Insights into Its Components and Their Post-translational Modification *. *Molecular & Cellular Proteomics.* **7**(2), pp.347-369.

Chassé, H., Boulben, S., Costache, V., Cormier, P. and Morales, J. 2017. Analysis of translation using polysome profiling. *Nucleic Acids Research.* **45**(3), pp.e15-e15.

Chen, C., Stevens, B., Kaur, J., Smilansky, Z., Cooperman Barry, S. and Goldman Yale, E. 2011. Allosteric vs. spontaneous exit-site (E-site) tRNA dissociation early in protein synthesis. *Proceedings of the National Academy of Sciences.* **108**(41), pp.16980-16985.

Chen, F.W. and Ioannou, Y.A. 1999. Ribosomal proteins in cell proliferation and apoptosis. *International reviews of immunology.* **18**(5-6), pp.429-448.

Cosgrove, J.W., Heikkila, J.J. and Brown, I.R. 1982. Translation of mRNA associated with monosomes and residual polysomes following disaggregation of brain polysomes by LSD and hyperthermia. *Neurochemical Research.* **7**(4), pp.505-518.

Crick, F.H. 1958. On protein synthesis. *Symp Soc Exp Biol.* **12**, pp.138-163.

Curran, S.P. and Ruvkun, G. 2007. Lifespan regulation by evolutionarily conserved genes essential for viability. *PLoS Genet.* **3**(4), pe56.

D'Souza, M.N., Gowda, N.K.C., Tiwari, V., Babu, R.O., Anand, P., Dastidar, S.G., Singh, R., James, O.G., Selvaraj, B., Pal, R., Ramesh, A., Chattarji, S., Chandran, S., Gulyani, A., Palakodeti, D. and Muddashetty, R.S. 2018. FMRP Interacts with C/D Box snoRNA in the Nucleus and Regulates Ribosomal RNA Methylation. *iScience.* **9**, pp.399-411.

Dalla Venezia, N., Vincent, A., Marcel, V., Catez, F. and Diaz, J.-J. 2019. Emerging Role of Eukaryote Ribosomes in Translational Control. *International journal of molecular sciences.* **20**(5), p1226.

Demarco, R.S., Eikenes Å, H., Haglund, K. and Jones, D.L. 2014. Investigating spermatogenesis in Drosophila melanogaster. *Methods.* **68**(1), pp.218-227.

Dever, T.E., Dinman, J.D. and Green, R. 2018. Translation Elongation and Recoding in Eukaryotes. *Cold Spring Harb Perspect Biol.* **10**(8).

Dietzl, G., Chen, D., Schnorrer, F., Su, K.-C., Barinova, Y., Fellner, M., Gasser, B., Kinsey, K., Oppel, S., Scheiblauer, S., Couto, A., Marra, V., Keleman, K. and Dickson, B.J. 2007. A genome-wide transgenic RNAi library for conditional gene inactivation in Drosophila. Nature. **448**(7150), pp.151-156.

Djumagulov, M., Demeshkina, N., Jenner, L., Rozov, A., Yusupov, M. and Yusupova, G. 2021. Accuracy mechanism of eukaryotic ribosome translocation. *Nature.* **600**(7889), pp.543-546.

Doudna, J.A. and Rath, V.L. 2002. Structure and function of the eukaryotic ribosome: the next frontier. *Cell.* **109**(2), pp.153-156.

Duffy, J.B. 2002. GAL4 system in drosophila: A fly geneticist's swiss army knife. *genesis.* **34**(1-2), pp.1-15.

Dzitoyeva, S., Dimitrijevic, N. and Manev, H. 2001. Intra-abdominal injection of double-stranded RNA into anesthetized adult Drosophila triggers RNA interference in the central nervous system. *Molecular Psychiatry.* **6**(6), pp.665-670.

Emsley, P., Lohkamp, B., Scott, W.G. and Cowtan, K. 2010. Features and development of Coot. *Acta Crystallogr D Biol Crystallogr.* **66**(Pt 4), pp.486-501.

Ferretti, M., Ghalei, H., Ward, E., Potts, E. and Karbstein, K. 2017. Rps26 directs mRNA-specific translation by recognition of Kozak sequence elements. *Nature structural & molecular biology.* **24**(9), pp.700-707.

Ferretti, M. and Karbstein, K. 2019. Does Functional Specialization of Ribosomes Really Exist? *RNA.* **25**, prna.069823.069118.

Frank, J., Gao, H., Sengupta, J., Gao, N. and Taylor Derek, J. 2007. The process of mRNA–tRNA translocation. *Proceedings of the National Academy of Sciences.* **104**(50), pp.19671-19678.

Frolova, L., Le Goff, X., Zhouravleva, G., Davydova, E., Philippe, M. and Kisselev, L. 1996. Eukaryotic polypeptide chain release factor eRF3 is an eRF1- and ribosome-dependent guanosine triphosphatase. *Rna.* **2**(4), pp.334-341.

Ganoza, M.C., Kiel, M.C. and Aoki, H. 2002. Evolutionary conservation of reactions in translation. *Microbiol Mol Biol Rev.* **66**(3), pp.460-485, table of contents.

Gebauer, F., Preiss, T. and Hentze, M.W. 2012. From cis-regulatory elements to complex RNPs and back. *Cold Spring Harbor perspectives in biology.* **4**(7), pa012245.

Genuth, N.R. and Barna, M. 2018. Heterogeneity and specialized functions of translation machinery: from genes to organisms. *Nature reviews. Genetics.* **19**(7), pp.431-452.

Gerst, J.E. 2018. Pimp My Ribosome: Ribosomal Protein Paralogs Specify Translational Control. *Trends in Genetics.* **34**(11), pp.832-845.

Grabher, C. and Wittbrodt, J. 2004. Efficient activation of gene expression using a heat-shock inducible Gal4/Vp16-UAS system in medaka. *BMC Biotechnol.* **4**, p26.

Grosjean, H. 2015. RNA modification: the Golden Period 1995-2015. *RNA (New York, N.Y.).* **21**(4), pp.625-626.

Guimaraes, J.C. and Zavolan, M. 2016. Patterns of ribosomal protein expression specify normal and malignant human cells. *Genome Biology.* **17**(1), p236.

Haag, E.S. and Dinman, J.D. 2019. Still Searching for Specialized Ribosomes. *Developmental Cell.* **48**(6), pp.744-746.

Hansen, M., Taubert, S., Crawford, D., Libina, N., Lee, S.J. and Kenyon, C. 2007. Lifespan extension by conditions that inhibit translation in Caenorhabditis elegans. *Aging Cell.* **6**(1), pp.95-110.

Hershey, J.W.B., Sonenberg, N. and Mathews, M.B. 2012. Principles of Translational Control: An Overview. *Cold Spring Harbor Perspectives in Biology.* **4**(12).

Hertz, M.I., Landry, D.M., Willis, A.E., Luo, G. and Thompson, S.R. 2013. Ribosomal Protein S25 Dependency Reveals a Common Mechanism for Diverse Internal Ribosome Entry Sites and Ribosome Shunting. *Molecular and Cellular Biology.* **33**(5), pp.1016-1026.

Heyer, Erin E. and Moore, Melissa J. 2016. Redefining the Translational Status of 80S Monosomes. *Cell.* **164**(4), pp.757-769.

Hiller, D.A., Singh, V., Zhong, M. and Strobel, S.A. 2011. A two-step chemical mechanism for ribosome-catalysed peptide bond formation. *Nature.* **476**(7359), pp.236-239.

Hipkiss, A.R. 2007. On why decreasing protein synthesis can increase lifespan. *Mech Ageing Dev.* **128**(5-6), pp.412-414.

Holt, Christine E. and Schuman, Erin M. 2013. The Central Dogma Decentralized: New Perspectives on RNA Function and Local Translation in Neurons. *Neuron.* **80**(3), pp.648-657.

Hopes, T., Norris, K., Agapiou, M., McCarthy, C.G.P., Lewis, P.A., O'Connell, M.J., Fontana, J. and Aspden, J.L. 2021. Ribosome heterogeneity in Drosophila melanogaster gonads through paralog-switching. *bioRxiv.* p2020.2001.2020.913020.

Ingolia, N.T., Ghaemmaghami, S., Newman, J.R.S. and Weissman, J.S. 2009. Genome-Wide Analysis in Vivo of Translation with Nucleotide Resolution Using Ribosome Profiling. *Science.* **324**(5924), pp.218-223.

Jackson, R.J., Hellen, C.U. and Pestova, T.V. 2010. The mechanism of eukaryotic translation initiation and principles of its regulation. *Nat Rev Mol Cell Biol.* **11**(2), pp.113-127.

Jeibmann, A. and Paulus, W. 2009. Drosophila melanogaster as a model organism of brain diseases. *International journal of molecular sciences.* **10**(2), pp.407-440.

Jia, B., Wang, T. and Lehmann, J. 2021. Peptidyl transferase center decompaction and structural constraints during early protein elongation on the ribosome. *Scientific Reports.* **11**(1), p24061.

Juszkiewicz, S., Chandrasekaran, V., Lin, Z., Kraatz, S., Ramakrishnan, V. and Hegde, R.S. 2018. ZNF598 Is a Quality Control Sensor of Collided Ribosomes. *Mol Cell.* **72**(3), pp.469-481.e467.

Kanca, O., Bellen, H.J. and Schnorrer, F. 2017. Gene Tagging Strategies To Assess Protein Expression, Localization, and Function in Drosophila. *Genetics.* **207**(2), pp.389-412.

Kapur, M., Monaghan, C.E. and Ackerman, S.L. 2017. Regulation of mRNA Translation in Neurons-A Matter of Life and Death. *Neuron.* **96**(3), pp.616-637.

Kelen, K.V.D., Beyaert, R., Inzé, D. and Veylder, L.D. 2009. Translational control of eukaryotic gene expression. *Critical Reviews in Biochemistry and Molecular Biology.* **44**(4), pp.143-168.

Kelly, S.M., Elchert, A. and Kahl, M. 2017. Dissection and Immunofluorescent Staining of Mushroom Body and Photoreceptor Neurons in Adult Drosophila melanogaster Brains. *J Vis Exp.* (129).

Kišonaitė, M., Wild, K., Lapouge, K., Ruppert, T. and Sinning, I. 2022. High-resolution structures of a thermophilic eukaryotic 80S ribosome reveal atomistic details of translocation. *Nature Communications.* **13**(1), p476.

Kondrashov, N., Pusic, A., Stumpf, C.R., Shimizu, K., Hsieh, A.C., Ishijima, J., Shiroishi, T. and Barna, M. 2011. Ribosome-mediated specificity in Hox mRNA translation and vertebrate tissue patterning. *Cell.* **145**(3), pp.383-397.

Kong, J. and Lasko, P. 2012. Translational control in cellular and developmental processes. *Nature Reviews Genetics.* **13**(6), pp.383-394.

Lecampion, C., Floris, M., Fantino, J.R., Robaglia, C. and Laloi, C. 2016. An Easy Method for Plant Polysome Profiling. *J Vis Exp.* (114).

Li, X., Mooney, P., Zheng, S., Booth, C.R., Braunfeld, M.B., Gubbens, S., Agard, D.A. and Cheng, Y. 2013. Electron counting and beam-induced motion correction enable near-atomic-resolution single-particle cryo-EM. *Nature methods.* **10**(6), pp.584-590.

Liu, B., Han, Y. and Qian, S.B. 2013. Cotranslational Response to Proteotoxic Stress by Elongation Pausing of Ribosomes. *Molecular Cell.* **49**(3), pp.453-463.

Liu, B. and Qian, S.B. 2016. Characterizing inactive ribosomes in translational profiling. *Translation (Austin).* **4**(1), pe1138018.

Locati, M.D., Pagano, J.F.B., Girard, G., Ensink, W.A., van Olst, M., van Leeuwen, S., Nehrdich, U., Spaink, H.P., Rauwerda, H., Jonker, M.J., Dekker, R.J. and Breit, T.M. 2017. Expression of distinct maternal and somatic 5.8S, 18S, and 28S rRNA types during zebrafish development. *Rna.* **23**(8), pp.1188-1199.

Loveland, A.B., Demo, G. and Korostelev, A.A. 2020. Cryo-EM of elongating ribosome with EF-Tu•GTP elucidates tRNA proofreading. *Nature.* **584**(7822), pp.640-645.

Ludwig, L.S., Gazda, H.T., Eng, J.C., Eichhorn, S.W., Thiru, P., Ghazvinian, R., George, T.I., Gotlib, J.R., Beggs, A.H., Sieff, C.A., Lodish, H.F., Lander, E.S. and Sankaran, V.G. 2014. Altered translation of GATA1 in Diamond-Blackfan anemia. *Nature medicine.* **20**(7), pp.748-753.

Mageeney, C.M. and Ware, V.C. 2019. Specialized eRpL22 paralogue-specific ribosomes regulate specific mRNA translation in spermatogenesis in Drosophila melanogaster. *Mol Biol Cell.* **30**(17), pp.2240-2253.

Martin, I., Dawson, V.L. and Dawson, T.M. 2011. Recent advances in the genetics of Parkinson's disease. *Annual review of genomics and human genetics.* **12**, pp.301-325.

Marygold, S.J., Roote, J., Reuter, G., Lambertsson, A., Ashburner, M., Millburn, G.H., Harrison, P.M., Yu, Z., Kenmochi, N., Kaufman, T.C., Leevers, S.J. and Cook, K.R. 2007. The ribosomal protein genes and Minute loci of Drosophila melanogaster. *Genome Biology.* **8**(10), pR216.

McClure, C.D., Hassan, A., Aughey, G.N., Butt, K., Estacio-Gómez, A., Duggal, A., Ying Sia, C., Barber, A.F. and Southall, T.D. 2022. An auxin-inducible, GAL4-compatible, gene expression system for Drosophila. *eLife.* **11**, pe67598.

McKenzie, A.T., Wang, M., Hauberg, M.E., Fullard, J.F., Kozlenkov, A., Keenan, A., Hurd, Y.L., Dracheva, S., Casaccia, P., Roussos, P. and Zhang, B. 2018. Brain Cell Type Specific Gene Expression and Co-expression Network Architectures. *Scientific Reports.* **8**(1), p8868.

Merrick, W.C. and Pavitt, G.D. 2018. Protein Synthesis Initiation in Eukaryotic Cells. *Cold Spring Harb Perspect Biol.* **10**(12).

Moazed, D. and Noller, H.F. 1989. Intermediate states in the movement of transfer RNA in the ribosome. *Nature.* **342**(6246), pp.142-148.

Munro, J.B., Altman, R.B., Tung, C.S., Cate, J.H., Sanbonmatsu, K.Y. and Blanchard, S.C. 2010. Spontaneous formation of the unlocked state of the ribosome is a multistep process. *Proc Natl Acad Sci U S A.* **107**(2), pp.709-714.

Murphy, J.C., Schumann, S., Harrington, E., Vasconcelos, E.J.R., Mottram, T.J., Aspden, J.L. and Whitehouse, A. 2022. Kaposi's sarcoma-associated herpesvirus induces specialised ribosomes to efficiently translate viral lytic mRNAs. *bioRxiv.* p2022.2003.2011.483946.

Nakano, K. and Hara, H. 1979. Measurement of the protein-synthetic activity in vivo of various tissues in rats by using [3H]Puromycin. *Biochemical Journal.* **184**(3), pp.663-668.

Nichols, C.D., Becnel, J. and Pandey, U.B. 2012. Methods to assay Drosophila behavior. *J Vis Exp.* (61).

Nickless, A., Bailis, J.M. and You, Z. 2017. Control of gene expression through the nonsense-mediated RNA decay pathway. *Cell Biosci.* **7**, p26.

Nishimura, T., Wada, T., Yamamoto, K.T. and Okada, K. 2005. The Arabidopsis STV1 protein, responsible for translation reinitiation, is required for auxin-mediated gynoecium patterning. *The Plant cell.* **17**(11), pp.2940-2953.

Noll, H. 2008. The discovery of polyribosomes. *BioEssays.* **30**(11-12), pp.1220-1234.

Noll, M., Hapke, B., Schreier, M.H. and Noll, H. 1973. Structural dynamics of bacterial ribosomes: I. Characterization of vacant couples and their relation to complexed ribosomes. *Journal of Molecular Biology.* **75**(2), pp.281-294.

Norris, K., Hopes, T. and Aspden, J.L. 2021. Ribosome heterogeneity and specialization in development. *WIREs RNA.* **12**(4), pe1644.

Park, H.S., Himmelbach, A., Browning, K.S., Hohn, T. and Ryabova, L.A. 2001. A plant viral "reinitiation" factor interacts with the host translational machinery. *Cell.* **106**(6), pp.723-733.

Patraquim, P., Mumtaz, M.A.S., Pueyo, J.I., Aspden, J.L. and Couso, J.-P. 2020. Developmental regulation of canonical and small ORF translation from mRNAs. *Genome Biology.* **21**(1), p128.

Penczek, P.A., Frank, J. and Spahn, C.M.T. 2006. A method of focused classification, based on the bootstrap 3D variance analysis, and its application to EF-G-dependent translocation. *Journal of Structural Biology.* **154**(2), pp.184-194.

Pestova, T.V. and Hellen, C.U. 2003. Translation elongation after assembly of ribosomes on the Cricket paralysis virus internal ribosomal entry site without initiation factors or initiator tRNA. *Genes Dev.* **17**(2), pp.181-186.

Pettersen, E.F., Goddard, T.D., Huang, C.C., Couch, G.S., Greenblatt, D.M., Meng, E.C. and Ferrin, T.E. 2004. UCSF Chimera—A visualization system for exploratory research and analysis. *Journal of Computational Chemistry.* **25**(13), pp.1605-1612.

Pisarev, A.V., Skabkin, M.A., Pisareva, V.P., Skabkina, O.V., Rakotondrafara, A.M., Hentze, M.W., Hellen, C.U. and Pestova, T.V. 2010. The role of ABCE1 in eukaryotic posttermination ribosomal recycling. *Mol Cell.* **37**(2), pp.196-210.

Posey, K.L., Jones, L.B., Cerda, R., Bajaj, M., Huynh, T., Hardin, P.E. and Hardin, S.H. 2001. Survey of transcripts in the adult Drosophila brain. *Genome Biol.* **2**(3), pResearch0008.

Raina, M. and Ibba, M. 2014. tRNAs as regulators of biological processes. *Frontiers in Genetics.* **5**.

Ramagopal, S. 1991. Covalent modifications of ribosomal proteins in growing and aggregation-competent dictyostelium discoideum: phosphorylation and methylation. *Biochem Cell Biol.* **69**(4), pp.263-268.

Reis-Rodrigues, P., Czerwieniec, G., Peters, T.W., Evani, U.S., Alavez, S., Gaman, E.A., Vantipalli, M., Mooney, S.D., Gibson, B.W., Lithgow, G.J. and Hughes, R.E. 2012. Proteomic analysis of age-dependent changes in protein solubility identifies genes that modulate lifespan. *Aging Cell.* **11**(1), pp.120-127.

Rodnina, M.V., Gromadski, K.B., Kothe, U. and Wieden, H.-J. 2005. Recognition and selection of tRNA in translation. *FEBS Letters.* **579**(4), pp.938-942.

Scheres, S.H.W. and Chen, S. 2012. Prevention of overfitting in cryo-EM structure determination. *Nature methods.* **9**(9), pp.853-854.

Schmidt, C., Becker, T., Heuer, A., Braunger, K., Shanmuganathan, V., Pech, M., Berninghausen, O., Wilson, D.N. and Beckmann, R. 2016. Structure of the hypusinylated eukaryotic translation factor eIF-5A bound to the ribosome. *Nucleic Acids Research.* **44**(4), pp.1944-1951.

Schneider-Poetsch, T., Ju, J., Eyler, D.E., Dang, Y., Bhat, S., Merrick, W.C., Green, R., Shen, B. and Liu, J.O. 2010. Inhibition of eukaryotic translation elongation by cycloheximide and lactimidomycin. *Nat Chem Biol.* **6**(3), pp.209-217.

Schuller, A.P. and Green, R. 2018. Roadblocks and resolutions in eukaryotic translation. *Nature Reviews Molecular Cell Biology.* **19**(8), pp.526-541.

Segev, N. and Gerst, J.E. 2018. Specialized ribosomes and specific ribosomal protein paralogs control translation of mitochondrial proteins. *The Journal of cell biology.* **217**(1), pp.117-126.

Shi, Z., Fujii, K., Kovary, K.M., Genuth, N.R., Röst, H.L., Teruel, M.N. and Barna, M. 2017. Heterogeneous Ribosomes Preferentially Translate Distinct Subpools of mRNAs Genome-wide. *Molecular cell.* **67**(1), pp.71-83.e77.

Simpson, R.J. 2006. Fragmentation of protein using trypsin. *CSH Protoc.* **2006**(5).

Simsek, D. and Barna, M. 2017. An emerging role for the ribosome as a nexus for post-translational modifications. *Current Opinion in Cell Biology.* **45**, pp.92-101.

Simsek, D., Tiu, G.C., Flynn, R.A., Byeon, G.W., Leppek, K., Xu, A.F., Chang, H.Y. and Barna, M. 2017. The Mammalian Ribo-interactome Reveals Ribosome Functional Diversity and Heterogeneity. *Cell.* **169**(6), pp.1051-1065.e1018.

Slavov, N., Semrau, S., Airoldi, E., Budnik, B. and van Oudenaarden, A. 2015. Differential Stoichiometry among Core Ribosomal Proteins. *Cell Reports.* **13**(5), pp.865-873.

Sonenberg, N. and Hinnebusch, A.G. 2009. Regulation of translation initiation in eukaryotes: mechanisms and biological targets. *Cell.* **136**(4), pp.731-745.

Stark, H. 2010. GraFix: stabilization of fragile macromolecular complexes for single particle cryo-EM. *Methods Enzymol.* **481**, pp.109-126.

Steward, O. and Schuman, E.M. 2003. Compartmentalized Synthesis and Degradation of Proteins in Neurons. *Neuron.* **40**(2), pp.347-359.

Taylor, D.J., Nilsson, J., Merrill, A.R., Andersen, G.R., Nissen, P. and Frank, J. 2007. Structures of modified eEF2 80S ribosome complexes reveal the role of GTP hydrolysis in translocation. *Embo j.* **26**(9), pp.2421-2431.

Thompson, R.F., Iadanza, M.G., Hesketh, E.L., Rawson, S. and Ranson, N.A. 2019. Collection, pre-processing and on-the-fly analysis of data for high-resolution, single-particle cryo-electron microscopy. *Nat Protoc.* **14**(1), pp.100-118.

Thomson, E., Ferreira-Cerca, S. and Hurt, E. 2013. Eukaryotic ribosome biogenesis at a glance. *Journal of Cell Science.* **126**(21), p4815.

Turkina, M.V., Klang Årstrand, H. and Vener, A.V. 2011. Differential Phosphorylation of Ribosomal Proteins in Arabidopsis thaliana Plants during Day and Night. *PLOS ONE.* **6**(12), pe29307.

Tüting, C., Iacobucci, C., Ihling, C.H., Kastritis, P.L. and Sinz, A. 2020. Structural analysis of 70S ribosomes by cross-linking/mass spectrometry reveals conformational plasticity. *Scientific Reports.* **10**(1), p12618.

Uemura, S., Aitken, C.E., Korlach, J., Flusberg, B.A., Turner, S.W. and Puglisi, J.D. 2010. Real-time tRNA transit on single translating ribosomes at codon resolution. *Nature.* **464**(7291), pp.1012-1017.

Ugur, B., Chen, K. and Bellen, H.J. 2016. Drosophila tools and assays for the study of human diseases. *Disease Models & Mechanisms.* **9**(3), p235.

Vaklavas, C., Blume, S.W. and Grizzle, W.E. 2017. Translational Dysregulation in Cancer: Molecular Insights and Potential Clinical Applications in Biomarker Development. *Frontiers in Oncology.* **7**.

van de Waterbeemd, M., Tamara, S., Fort, K.L., Damoc, E., Franc, V., Bieri, P., Itten, M., Makarov, A., Ban, N. and Heck, A.J.R. 2018. Dissecting ribosomal particles throughout the kingdoms of life using advanced hybrid mass spectrometry methods. *Nat Commun.* **9**(1), p2493.

Wang, H., Ku, L., Osterhout, D.J., Li, W., Ahmadian, A., Liang, Z. and Feng, Y. 2004. Developmentally-programmed FMRP expression in oligodendrocytes: a potential role of FMRP in regulating translation in oligodendroglia progenitors. *Hum Mol Genet.* **13**(1), pp.79-89.

Warner, J.R. and Knopf, P.M. 2002. The discovery of polyribosomes. *Trends in Biochemical Sciences.* **27**(7), pp.376-380.

Warnes, M.G.R., Bolker, B., Bonebakker, L., Gentleman, R. and Huber, W. 2016. Package 'gplots'. *Various R programming tools for plotting data.*

Whittle, C.A. and Krochko, J.E. 2009. Transcript profiling provides evidence of functional divergence and expression networks among ribosomal protein gene paralogs in Brassica napus. *The Plant cell.* **21**(8), pp.2203-2219.

Wool, I.G. 1996. Extraribosomal functions of ribosomal proteins. *Trends in Biochemical Sciences.* **21**(5), pp.164-165.

Woolford, J.L. and Baserga, S.J. 2013. Ribosome Biogenesis in the Yeast Saccharomyces cerevisiae. *Genetics.* **195**(3), p643.

Xue, S. and Barna, M. 2012. Specialized ribosomes: a new frontier in gene regulation and organismal biology. *Nature Reviews Molecular Cell Biology.* **13**(6), pp.355-369.

Xue, S., Tian, S., Fujii, K., Kladwang, W., Das, R. and Barna, M. 2015. RNA regulons in Hox 5' UTRs confer ribosome specificity to gene regulation. *Nature.* **517**(7532), pp.33-38.

Yamada, S.B., Gendron, T.F., Niccoli, T., Genuth, N.R., Grosely, R., Shi, Y., Glaria, I., Kramer, N.J., Nakayama, L., Fang, S., Dinger, T.J.I., Thoeng, A., Rocha, G., Barna, M., Puglisi, J.D., Partridge, L., Ichida, J.K., Isaacs, A.M., Petrucelli, L. and Gitler, A.D. 2019. RPS25 is required for efficient RAN translation of C9orf72 and other neurodegenerative disease-associated nucleotide repeats. *Nature Neuroscience.* **22**(9), pp.1383-1388.

Yamamoto, T. 2007. Roles of the ribosomal protein S19 dimer and the C5a receptor in pathophysiological functions of phagocytic leukocytes. *Pathology International.* **57**(1), pp.1-11.

Yong, W.H., Shabihkhani, M., Telesca, D., Yang, S., Tso, J.L., Menjivar, J.C., Wei, B., Lucey, G.M., Mareninov, S., Chen, Z., Liau, L.M., Lai, A., Nelson, S.F., Cloughesy, T.F. and Tso, C.L. 2015. Ribosomal Proteins RPS11 and RPS20, Two Stress-Response Markers of Glioblastoma Stem Cells, Are Novel Predictors of Poor Prognosis in Glioblastoma Patients. *PLoS One.* **10**(10), pe0141334.

Yoshikawa, H., Larance, M., Harney, D.J., Sundaramoorthy, R., Ly, T., Owen-Hughes, T. and Lamond, A.I. 2018. Efficient analysis of mammalian polysomes in cells and tissues using Ribo Mega-SEC. *eLife.* **7**, pe36530.

Zecha, J., Satpathy, S., Kanashova, T., Avanessian, S.C., Kane, M.H., Clauser, K.R., Mertins, P., Carr, S.A. and Kuster, B. 2019. TMT Labeling for the Masses: A Robust and Cost-efficient, In-solution Labeling Approach. *Mol Cell Proteomics.* **18**(7), pp.1468-1478.

Zhang and Elias, J.E. 2017. Relative Protein Quantification Using Tandem Mass Tag Mass Spectrometry. In: Comai, L., et al. eds. *Proteomics: Methods and Protocols.* New York, NY: Springer New York, pp.185-198.

Zhang, H., Dou, S., He, F., Luo, J., Wei, L. and Lu, J. 2018. Genome-wide maps of ribosomal occupancy provide insights into adaptive evolution and regulatory roles of uORFs during Drosophila development. *PLoS Biol.* **16**(7), pe2003903.

Zhang, K. 2016. Gctf: Real-time CTF determination and correction. *Journal of structural biology.* **193**(1), pp.1-12.

Zhou, J., Lancaster, L., Donohue, J.P. and Noller, H.F. 2014. How the ribosome hands the A-site tRNA to the P site during EF-G-catalyzed translocation. *Science.* **345**(6201), pp.1188-1191.

Zivanov, J., Nakane, T., Forsberg, B.O., Kimanius, D., Hagen, W.J., Lindahl, E. and Scheres, S.H. 2018. New tools for automated high-resolution cryo-EM structure determination in RELION-3. *Elife.* **7**.